UNIVERSIDADE DE LISBOA
FACULDADE DE CIÊNCIAS
DEPARTAMENTO DE FÍSICA

Modelling Rett syndrome with 3D cardiac models derived from patient-specific human induced pluripotent stem cells

Ana Luísa Fraga Rayagra

Mestrado em Engenharia Biomédica e Biofísica

Dissertação orientada por:
Professora Doutora Maria Margarida Diogo
Professor Doutor Hugo Alexandre Ferreira

2023

Acknowledgments

Começo por agradecer a todos os que fizeram parte do meu percurso durante este ano e com quem pude partilhar esta experiência tão enriquecedora. Tive o prazer de conhecer pessoas que ficarão certamente para sempre na minha memória.

Em primeiro lugar, gostaria de agradecer ao Professor Joaquim Cabral por me ter aceite no Stem Cell Engineering and Regenerative Medicine Research Group (SCERG) e me fazer sentir tão bem recebida.

À minha orientadora, Professora Margarida Diogo, começo por agradecer a oportunidade de poder realizar a minha tese de mestrado consigo e por me ter proporcionado trabalhar num projeto tão interessante e inovador. Estou muito grata por toda a orientação e aprendizagens que me proporcionou, por me ter ajudado em tudo o que foi necessário e pela confiança que teve em mim desde o primeiro momento. A Professora aceitou que eu fizesse parte deste projeto num período particularmente difícil da minha vida, mostrando uma compreensão, sensibilidade e empatia que foram muito importantes para mim nesse momento e durante todo o percurso. Será algo que nunca esquecerei.

À minha orientadora, Doutora Mariana Branco. Não há nada que possa escrever ou dizer que consiga refletir o quão importante foste neste ano e que possa espelhar a gratidão que tenho por tudo o que me ensinaste, quer profissional quer pessoalmente. Obrigada pela orientação contínua, por todos os conhecimentos transmitidos, pela paciência, pela disponibilidade e por teres sempre uma palavra amiga, salientado o meu valor e fazendo-me sentir especial. Tal como a Professora Margarida, não posso deixar de evidenciar a tua compreensão, sensibilidade e empatia, que me ajudaram a chegar onde estou hoje. Dadas as circunstâncias, não foi possível atribuir-te o devido reconhecimento pelo trabalho que desempenhaste, que espero ao longo deste ano ter de alguma forma compensado. Sou uma sortuda poder ter tido alguém como tu ao meu lado. Foi um orgulho ter sido orientada por ti e sabes que tens um lugar muito especial no meu coração.

Ao meu orientador, Professor Hugo Ferreira, agradeço de igual forma toda a disponibilidade e apoio, fundamentais para conseguir ter realizado a dissertação que pretendia e, posteriormente, para que pudesse produzir este trabalho de que me orgulho.

À minha família. Obrigada pelo vosso amor. Agradeço por estarem sempre presentes, pela vossa paciência e compreensão, por me apoiarem em tudo e acreditarem em mim incondicionalmente. Sou uma sortuda por vos ter.

Aos meus amigos, agradeço por me apoiarem em tudo, por me valorizarem, pela infinita motivação e por fazerem sobressair o melhor de mim. Devo-vos muito por estarem sempre ao meu lado, partilhando e celebrando os bons momentos, mas ajudando-me sempre a ultrapassar os menos fáceis. São os melhores!

Agradeço ainda ao Miguel Tenreiro, pela preocupação e interesse no meu projeto e por todos os ensinamentos ao longo destes meses, assim como ao Tiago Nunes, Iryna Vykhlyantseva e João Henriques por toda a motivação, paciência e carinho.

Gostaria ainda de agradecer à Paula Klose, cujo apoio foi essencial para ter chegado onde cheguei.

Obrigada mais uma vez a todos!

Abstract

Rett syndrome (RTT) is a severe neurodevelopmental disorder caused by MeCP2 mutations, resulting mainly in impaired brain development and function, but also in a myriad of non-neurological problems, including cardiac abnormalities. Given the RTT multifaceted nature, it has been challenging to accurately model the associated phenotypes and to develop therapies. RTT models mostly focus on the neurological abnormalities, with few mimicking the cardiac problems. To date, only animal models have been used to study the disease in the heart, but these do not faithfully mimic the phenotypic aspects found in patients. Therefore, we developed, to the best of our knowledge, the first 3D cardiac model of RTT derived from patient-specific human induced pluripotent stem cells (hiPSCs).

RTT and healthy hiPSCs were successfully differentiated into cardiomyocytes (CMs) as 3D aggregates. However, RTT-derived alterations in these CM aggregates were verified, including differences in their size and compaction degree, being higher and lower in the RTT aggregates, respectively. Moreover, the characterization of the aggregate cavities and CM sarcomeres revealed differences between conditions. A higher percentage of the RTT aggregate area was occupied by cavities, which was unrelated to the number of cavities/aggregate, and the cavities presented a variable size. This disparity between conditions was not driven by CM proliferation differences. Furthermore, RTT CMs presented sarcomere structural impairment, with a lower density of myofibril, the presence of which was more pronounced near the CM nucleus, and a shorter sarcomere length.

Subsequently, the analysis of RTT-derived changes to the CM aggregates will be continued, namely to elucidate the mechanisms associated to the morphological alterations of the aggregates, and the structural abnormalities of RTT CMs. Moreover, it will be fundamental to study potential RTT-derived CM functional alterations. Additionally, co-culturing CMs with neurons, and recreating the heterogeneity of cardiac cells present in the human heart with a cardiac microtissue and organoid, would be crucial.

Keywords: Rett Syndrome, Induced Pluripotent Stem Cells, Cardiomyocyte Differentiation, 3D Culture, Cardiac Disease Modelling

Resumo

A Síndrome de Rett (RTT) é uma perturbação rara do neurodesenvolvimento causada maioritariamente por mutações no gene que codifica a proteína MeCP2, localizado no cromossoma X. Embora seja uma doença genética, as mutações que causam a RTT são praticamente todas esporádicas, com menos de 1% dos casos sendo hereditários. A incidência da RTT é mais elevada em indivíduos do sexo feminino, aproximadamente 91% dos casos reportados, afetando cerca de 1 em cada 10 000 a 23 000 mulheres mundialmente. Estes doentes podem apresentar uma ampla gama de sintomas, determinados pela localização, tipo e gravidade da mutação, ou, no caso dos indivíduos do sexo feminino, também pela inativação do cromossoma X. A doença progride em quatro fases e resulta principalmente em perturbações graves do desenvolvimento e função cerebrais, mas também numa miríade de problemas não neurológicos, nomeadamente anormalidades cardíacas, respiratórias, gastrointestinais, metabólicas e ósseas. Efetivamente, quase todos os aspetos da vida destes doentes são afetados, desde a sua capacidade de falar, andar, comer e até de respirar normalmente. Dada a gravidade dos sintomas, a expectativa de vida das pessoas com RTT é reduzida, havendo uma maior incidência de morte súbita, cerca de 26% das mortes. Tem-se especulado que o intervalo QT corrigido (QT_c) prolongado, um parâmetro que representa um prolongamento da repolarização cardíaca, poderá potenciar estas mortes súbitas verificadas nos doentes RTT. Apesar desta conexão, ainda é desconhecido se um intervalo QT_c prolongado nestas pessoas será um efeito direto da doença no coração ou um efeito secundário das manifestações do sistema nervoso.

Dada a raridade e a natureza multissistémica da RTT, a modelação com precisão dos fenótipos associados a esta doença, assim como o desenvolvimento de terapias para estes doentes, tem provado ser desafiante. Os modelos animais têm contribuído significativamente para a superação destas limitações. No entanto, a sua relevância clínica é afetada pelas diferenças entre espécies e a diversidade de fenótipos entre doentes dificilmente pode ser modelada usando essas estratégias. Mais recentemente, as características das células estaminais pluripotentes humanas (hPSCs), nomeadamente a sua capacidade de autorrenovação e o seu potencial para se diferenciarem em qualquer tipo de célula do corpo humano, têm despertado um entusiasmo geral para o desenvolvimento de novos modelos de doenças humanas. De facto, com o aumento do conhecimento sobre este tipo de células, as hPSCs têm surgido como uma alternativa promissora para o estudo da RTT, através de modelos alternativos que mimetizam com maior precisão a gravidade e as características da doença. Uma vez que as mutações no MeCP2 afetam especialmente diferentes estágios de desenvolvimento e função cerebrais, independentemente do tipo de modelo utilizado, as anormalidades neurológicas têm sido a componente da doença mais investigada. Por outro lado, muito poucos estudos recapitulam a RTT noutros órgãos afetados, como o coração. Neste contexto, apenas modelos animais, maioritariamente de murganho, têm sido utilizados para o estudo da componente cardíaca da RTT até à data.

Desta forma, este projeto teve como objetivo modelar, pela primeira vez, a RTT com modelos cardíacos 3D derivados de células estaminais pluripotentes induzidas (hiPSCs) específicas de doentes, assim como identificar alterações derivadas da doença que pudessem contribuir para fornecer novos alvos para estratégias terapêuticas para a RTT. Para tal, o estudo foi dividido em duas partes principais. A primeira parte teve como objetivo estudar as alterações derivadas da RTT no processo de diferenciação cardíaca, após otimização da diferenciação de hiPSCs em cardiomiócitos (CMs) como agregados 3D, usando tanto linhas celulares mutadas como saudáveis. A segunda parte centrou-se no estudo de alterações morfológicas dos agregados de CMs derivados de hiPSCs RTT, tendo-se explorado as diferenças na arquitetura estrutural e composição celular dos agregados 3D de CMs. Para além destes

aspetos de organização macroestrutural, foram também estudadas as alterações microestruturais dos sarcómeros dos CMs.

Em primeiro lugar, demonstrou-se ser possível diferenciar com sucesso hiPSCs RTT e saudáveis em CMs como agregados 3D. A otimização do processo de diferenciação cardíaca para cada linha celular foi realizada através da variação de dois parâmetros, nomeadamente do tamanho do agregado no início da diferenciação e da concentração da molécula de baixo peso molecular CHIR99021, modeladora da via de sinalização *wingless integrated* (Wnt). Os resultados obtidos sugerem que esses parâmetros variam dependentemente da linha celular e não são um parâmetro de distinção entre linhas celulares RTT e saudáveis. No entanto, foi possível observar alterações derivadas da RTT nesses agregados 3D de CMs, incluindo diferenças no tamanho e grau de compactação dos agregados, sendo estes maior e menor, respetivamente, nos agregados RTT.

Em segundo lugar, os agregados 3D de CMs derivados de hiPSCs RTT foram estudados face aos agregados derivados de hiPSCs saudáveis, tendo-se avaliado a sua morfologia, bem como a estrutura dos sarcómeros dos CMs. Além de CMs, outros tipos de células cardíacas naturalmente presentes *in vivo* no coração humano também foram encontrados em minoria nos agregados diferenciados RTT e saudáveis, incluindo células endoteliais e uma subpopulação de células progenitoras cardíacas. Tanto a caracterização das cavidades dos agregados como a dos sarcómeros dos CMs revelou alterações morfológicas dos agregados RTT comparativamente aos saudáveis. Os nossos resultados evidenciaram uma percentagem muito maior da área dos agregados RTT ocupada por cavidades, comparativamente com os controlos, não estando relacionada com o número de cavidades por agregado, parâmetro que foi semelhante entre as condições. Verificou-se ainda uma variação na proporção de cavidades de acordo com o seu tamanho entre agregados RTT e saudáveis, com os agregados RTT a apresentarem uma maior proporção de cavidades de maiores dimensões. Foi possível demonstrar que estas disparidades encontradas entre as cavidades dos agregados RTT e saudáveis não foram causadas por diferenças na proliferação dos CMs. Este trabalho sugeriu ainda a existência de um comprometimento estrutural dos sarcómeros dos CMs RTT, tendo-se verificado uma menor densidade de miofibrilhas, que se encontravam mais pronunciadas perto do núcleo dos CMs, assim como um comprimento menor dos sarcómeros, comparativamente com CMs saudáveis.

Futuramente, para além de mais replicados, será também fundamental utilizar linhas celulares adicionais nas experiências, incluindo linhas hiPSCs derivadas de doentes com mutações associadas à RTT diferentes, para a validação dos nossos resultados. Além disso, será necessário continuar a análise das alterações derivadas da RTT nos agregados de CMs, nomeadamente para melhor compreender os mecanismos associados às alterações morfológicas dos agregados, bem como às anomalias estruturais dos CMs RTT. O processo de diferenciação cardíaca a partir de hiPSCs RTT e saudáveis deverá ser caracterizado nomeadamente em termos de níveis de expressão génica dos principais genes envolvidos quer na diferenciação cardíaca a partir de hPSCs, quer na maturação dos CMs. Relativamente à análise morfológica das cavidades dos agregados, será interessante avaliar, entre outros, o nível de expressão de HAND1 em agregados RTT e saudáveis, já que foi sugerido anteriormente a sua necessidade para a auto-organização estrutural. Adicionalmente, para complementar o estudo da formação das cavidades dos agregados, deverá ser realizado um ensaio de imunomarcação para o marcador apoptótico CASPASE, de forma a compreender se a morte celular poderá ser um mecanismo associado à formação das cavidades. Por outro lado, será relevante avaliar as alterações funcionais nos agregados RTT. Através de uma análise do transiente de cálcio intracelular, deverão ser estimados parâmetros como a duração da contração e frequência cardíaca, tanto em condições padrão, como sob exposição a estimulação elétrica e química.

No entanto, a cultura de CMs por si só pode não permitir observar as anormalidades funcionais cardíacas já descritas em humanos. Assim sendo, uma vez que os CMs e os neurónios sofrem co-maturação durante a inervação do coração na embriogénese, o estudo das interações entre estes tipos

celulares é essencial, principalmente na modelação de doenças multissistémicas como esta. Por este motivo, numa outra fase, seria interessante co-cultivar CMs e neurónios do sistema nervoso autónomo, ambos derivados de hiPSCs. Esta abordagem permitiria captar potenciais alterações funcionais dos CMs RTT promovidas pelos neurónios RTT e desvendar informações sobre uma potencial interferência anormal entre essas duas populações celulares que, até à data, permanecem desconhecidas. Adicionalmente, seria também relevante recriar a heterogeneidade de células cardíacas presentes no coração humano, através da geração quer de um microtecido cardíaco, quer de um organoide. Para além de possivelmente possibilitarem o estudo da maturação celular e da função geral dos CMs em comparação com o modelo saudável mais simples, permitiriam compreender se as principais etapas que ocorrem durante o processo de desenvolvimento cardíaco na embriogénese, a forma como as diferentes populações celulares são especificadas e a função dos CMs são ou não afetadas pela RTT. Posteriormente, estes modelos poderiam ser ainda co-cultivados com neurónios, estabelecendo um modelo neuro-cardíaco 3D complexo para o estudo desta doença.

Keywords: Síndrome de Rett, Células Estaminais Pluripotentes Induzidas, Diferenciação de Cardiomiócitos, Cultura 3D, Modelação de Doenças Cardíacas

Table of contents

List of Figures

List of Tables

List of Acronyms

ActA Activin A

ANS autonomic nervous system

AP action potential

APD_{75} action potential duration at 75% of complete repolarization

BF bright-field

BMPs bone morphogenetic proteins

BSA bovine serum albumin

CDK cyclin-dependent kinase

CDKL5 cyclin-dependent kinase-like 5

CFs cardiac fibroblasts

CHIR glycogen synthase kinase 3 inhibitor CHIR99021

CMs cardiomyocytes

CNS central nervous system

CTD C-terminal domain

cTnT cardiac Troponin T

D day

DAPI 4',6-diamidino-2-phenylindole

DMEM/F12 Dulbecco's Modified Eagle Medium: Nutrient Mixture F-12

DMSO dimethylsulfoxide

EB embryoid body

ECM extracellular matrix

ECs endothelial cells

EHM engineered heart muscle

EHT engineered heart tissue

ESC embryonic stem cell

E/I excitatory/inhibitory

FBS fetal bovine serum

FB1 flow cytometry buffer 1

FB2 flow cytometry buffer 2

FGF fibroblast growth factor

FHF first heart field

FOXG1 forkhead box G1

FSS forward-scattered light

GCDR Gentle Cell Dissociation Reagent

GDNF glial cell line-derived neurotrophic factor

GSK3 glycogen synthase kinase 3

HDAC6 Histone Deacetylase 6

hESCs human embryonic stem cells

hiPSCs human induced pluripotent stem cells

hPSCs human pluripotent stem cells

IBI inter-beat interval

ID intervening domain

IGF-1 insulin-like growth factor-1

$I_{Na,Late}$ "late" sodium current

INs interneurons

iPSC induced pluripotent stem cell

IWP-4 inhibitor of wingless integrated production 4

KCC2 K^+-Cl^- cotransporter 2

KO-SR KnockOut™ serum replacement

LA left atria

LV left ventricle

MBD methyl-CpG-binding domain

MEAs microelectrode arrays

MeCP2 methyl-CpG-binding protein-2

microRNA miRNA

MT mutated

NCC neural crest cell

NCOR nuclear co-repressor

NGF nerve growth factor

NID nuclear co-repressor-silencing mediator of retinoic acid and thyroid hormone receptor interacting domain

NPC neural progenitor cell

NTD N-terminal domain

NT-3 neurotrophin-3

OCT4 Octamer Binding Transcription Factor 4

OFT outflow tract

PBS phosphate-buffered saline

PDMS polydimethylsiloxane

PenStrep penicillin/streptomycin

PFA paraformaldehyde

PNS peripheral nervous system

PS primitive streak

QTc corrected QT interval

RA right atria

REST RE1-silencing transcriptional factor

RNA-seq RNA sequencing

ROCKi Rho kinase inhibitor

RPMI Roswell Park Memorial Institute

RT room temperature

RTT Rett syndrome

RT-PCR real-time polymerase chain reaction

RV right ventricle

SD standard deviation

SEM standard error of mean

SHF second heart field

SMRT silencing mediator of retinoic acid and thyroid hormone receptor

SotaTool Sarcomere Organization and Texture Analysis Tool

SSEA4 Stage-Specific Embryonic Antigen-4

TGF-β transforming growth factor-beta

TRA-1-60 T Cell Receptor Alpha Locus

TRD transcriptional repression domain

TRIDs translational read-through-inducing drugs

TS Timothy syndrome

Wnt wingless integrated

WT wild-type

Chapter 1

Introduction

1.1. Rett Syndrome

1.1.1. Rett Syndrome Overview

Rett syndrome (RTT; OMIM #312750) is a neurodevelopmental disorder [1]–[3] first reported by Andreas Rett in 1966 [1], [3]. This rare genetic neurological condition mainly impacts the development and function of the brain [1]–[3]. Its incidence is higher in females, affecting about 1 in 10 000 to 23 000 women worldwide [1], [2], with solely about 9% of RTT cases being estimated to be found in men [3]. RTT patients have a life expectancy until middle age, or even longer, if they do not suffer from any other type of disease or complications and have an adequate clinical follow-up. Due to the severity of the symptoms, the life expectancy of patients is shortened, with sudden deaths being reported [1]–[3].

In 1999, Huda Zoghbi's laboratory identified that RTT is caused by mutations in the gene encoding methyl-CpG-binding protein-2 (MeCP2) on chromosome Xq28 [1]–[4]. This occurs in about 90% of RTT cases. The remaining 10%, corresponding to the RTT-like phenotype, are associated with mutations in the cyclin-dependent kinase-like 5 (CDKL5) and forkhead box G1 (FOXG1) genes [3], [4]. The MeCP2 gene has four exons, which experience alternative splicing and produce two transcripts, MeCP2-E1 e MeCP2-E2 [3]. Mutations in the MeCP2 gene cause a loss of function of this protein and a dysregulated expression of genes that it normally affects, some of which appear to be essential in the nervous system development beyond the early stages. Even though the nervous system seems to be the primary site, the specific target genes remain unknown [1].

The MeCP2 protein can act as a transcriptional activator or repressor, depending on the target gene with which it associates [1], [3], [4]. MeCP2 is composed of several domains (Figure 1.1), namely 1) the N-terminal domain (NTD), 2) the methyl-CpG-binding domain (MBD), 3) the intervening domain (ID), 4) the transcriptional repression domain (TRD), 5) the nuclear co-repressor (NCOR)-silencing mediator of retinoic acid and thyroid hormone receptor (SMRT) interacting domain (NID), located within the TRD, and 6) the C-terminal domain (CTD) [3]. The most frequent RTT mutations are located in the MBD and TRD. On the one hand, the MBD of the MeCP2 protein allows it to specifically bind to methylated DNA, while the TRD recruits repressor proteins that inhibit gene transcription [1], [3], [4].

Despite being a genetic disease, the mutations that cause RTT are almost all sporadic. Particularly, families with a girl with RTT have an increased risk of having a second child with RTT of less than 0.4%. Nonetheless, recurrence in families can occur due to mechanisms such as germline mosaicism [1]. The exact mechanism underlying how MeCP2 mutations cause RTT is still unknown. One

hypothesis is that a MeCP2 deficiency leads to a synaptic maturation inability in the cortex. On the other hand, another hypothesis involves brain cholesterol metabolism, stating that a lack of MeCP2 disrupts this mechanism, leading to abnormal neuronal development. Furthermore, recent evidence suggests that MeCP2 is also expressed in glial cells, whose dysfunction caused by a change in DNA methylation also appears to be involved in the RTT pathogenesis [4]. To date, at least 200 distinct mutations are associated with this disorder [1]. About 90% of RTT patients are diagnosed with a point mutation or small deletions in the MeCP2 gene, causing the symptomatic heterogeneity reported in these individuals [3]. Particularly, about 70% of RTT cases are due to four missense mutations, where a change in a base pair results in a different amino acid production at that position, (R106W, R133C, T158M, R306C) and four nonsense protein-truncating mutations, where a codon for an amino acid is changed to a STOP codon, resulting in a truncated protein, (early-truncating mutations R168X, R255X and R270X, and late-truncating mutation R294X) (Figure 1.1) [1]. Most of missense and late-truncating mutations in the CTD cases may be less severe, as the MeCP2 function is not completely abolished [3], [4]. The early-truncating mutation cases result in greater severity, since large deletions occur, and may eventually be responsible for the complete loss of MeCP2 function, which is associated with a more severe phenotype [1], [3], [4].

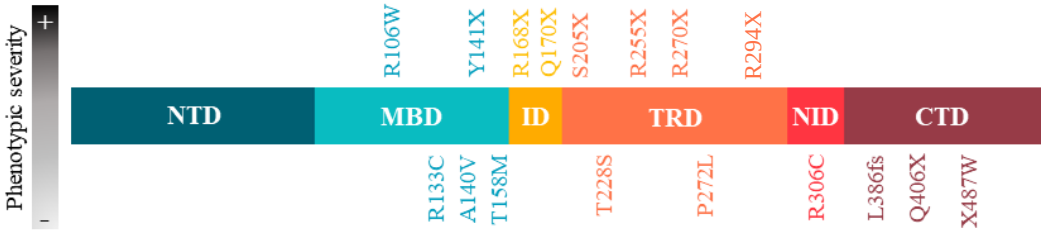

Figure 1.1: Schematic illustration of MeCP2 protein domains and corresponding most common mutations (data from 2021). (NTD) N-terminal domain; (MBD) methyl-CpG-binding domain; (ID) intervening domain; (TRD) transcriptional repression domain; (NID) NCOR/SMRT co-repressor interaction domain; (CTD) C-terminal domain. Adapted from [3].

Despite the phenotypic variability caused by MeCP2 mutations, the principal reason for distinct phenotypic severities in RTT is random X-chromosome inactivation. In addition, other factors, such as mechanisms related to epigenetics and associated with MeCP2 target genes, may also contribute to the phenotypic heterogeneity observed in RTT patients [3]. Women with RTT have a MeCP2 mutation on one of their two X-chromosomes, with only one copy of the MeCP2 gene being active in any cell, due to a random process called X-chromosome inactivation. Thus, in some cells the MeCP2 gene with the mutation is active, while in others it is the MeCP2 gene without the mutation that is active. This means that approximately half of the cells of these women have a normally functioning MeCP2 gene and the other half have a mutated (MT) one. On the other hand, as men only have one X-chromosome, a male patient with a MeCP2 mutation has that mutation present in his single copy of this gene [2]. Therefore, women with a single MT MeCP2 gene are more likely to survive, with an X-chromosome being randomly activated in each cell [1], [2], while men who have a similar mutation present an earlier onset and more severe clinical problems compared to RTT female patients [2].

RTT patients can suffer from a wide range of symptoms, determined either by the location, type and severity of the mutation, or, in the female case, also by X-chromosome inactivation [1], [2]. Although RTT is not a degenerative disorder [2], its progression typically appears to be [1]. Indeed, autopsy data from RTT patients reveal that the brain shows no signs of inflammation or degeneration. However, there is an overall decrease in the size of the brain and individual neurons. Additionally, there is an increase in the neuronal cell packaging in the hippocampus and a delayed neuronal maturation and synaptogenesis in the cerebral cortex [4].

RTT typically progresses through four stages (Table 1.1). After a period of normal development, there is a period of developmental arrest (stage I), around 6 to 18 months of age, followed by a period of rapid deterioration or regression (stage II). In this second stage, which generally occurs between 1 and 4 years old, children regress or lose acquired skills [1], losing, for example, the ability to walk and communicate [2]. RTT usually does not become clinically evident until around 2 to 4 years of age and the developmental potential of these patients is difficult to predict. Stage III, called the pseudostationary stage, takes place approximately between 2 to 10 years old. Above 10 years of age, the late motor deterioration stage (stage IV) occurs. This disorder leads to severe disabilities [1], where almost every aspect of the child's life is affected, from his ability to speak, walk, eat and even breathe easily [1], [2]. In addition, RTT patients experience learning difficulties, motor impairments, stereotyped repetitive hand movements, seizures, and autistic behaviour [3]. Among others, cardiac, gastrointestinal, metabolic and bone abnormalities are also reported. In RTT male individuals, symptoms usually begin earlier, with significant problems appearing at, or shortly after, birth [1].

Table 1.1: Most common RTT symptoms at each of the four stages of disease progression [1].

Stage	Stage name	Age	Common symptoms
I	Developmental arrest	6-18 months	• Gross motor development delay; • Disinterest in activities, for example play; • Loss of eye contact; • Decreased muscle tone; • Unusual placidity and calmness; • Breath-holding spells.
II	Rapid deterioration or regression	1-4 years	• Period of deterioration/regression; • Autistic-like behaviour; • Stereotypic repetitive hand movements during wakefulness; • Breathing irregularities; • Seizures and vacant spells that resemble seizures; • Sleep disorders; • Intermittent strabismus; • Irritability.
III	Pseudostationary	2-10 years	• Some improvement in behaviour, hand use, and communication skills (for example, attempts to communicate intent); • Good eye contact; • Continued mental impairment and hand stereotypies; • Increasing rigidity, bruxism, and involuntary tongue movements; • Motor dysfunction and seizures; • Continued breathing irregularities; • Poor weight gain despite good appetite; • Some degree of oral motor dysfunction.
IV	Late motor deterioration	>10 years	• No additional deterioration of cognitive, communication or hand skills; • Increased motor problems; • Cessation of walking; • Possible reduction of seizure frequency.

The RTT diagnosis is often confused with autism, cerebral palsy, or non-specific developmental delay. Interestingly, despite the rarity of the disorder, it is a relatively frequent cause of developmental delay in girls [2], [4]. The diagnosis requires that the patient meets the defined clinical criteria, being classified as typical/classic RTT or atypical RTT. On the one hand, a patient is diagnosed with typical RTT if he has experienced a period of regression followed by recovery or stabilization and meets all main criteria and exclusion criteria. It is not strictly necessary for him to meet the supportive criteria, but these help the diagnosis, as they are often found in typical RTT patients. On the other hand, a patient is diagnosed with atypical RTT if he has experienced a period of regression followed by recovery or stabilization and meets at least 2 of 4 main criteria and 5 of 11 supportive criteria. The main criteria, supportive criteria and exclusion criteria for typical RTT are summarized in Table 1.2 [2]. Since the MeCP2 mutation is also present in other disorders, the existence of the mutation itself is not sufficient for the RTT diagnosis [2], [4]. Despite MeCP2 mutations being frequently identified in patients who meet clinical criteria for RTT, up to 20% of women who meet all RTT clinical criteria may not have any identified mutation. In addition, and as mentioned before, some individuals have MeCP2 mutations but do not have RTT [1]. For these reasons, diagnosis is not performed using molecular genetic testing [1], [2].

Table 1.2: Main criteria, supportive criteria, and exclusion criteria for typical RTT used for RTT diagnosis [2].

Main criteria	• Partial or complete loss of acquired purposeful hand skills; • Partial or complete loss of acquired spoken language; • Gait abnormalities: impaired or absence of ability to walk; • Stereotypic hand movements such as hand wringing/squeezing, clapping/tapping, mouthing, and/or washing/rubbing automatism.
Supportive criteria	• Breathing disturbances when awake; • Bruxism when awake; • Impaired sleep pattern; • Abnormal muscle tone; • Peripheral vasomotor disturbances; • Scoliosis/kyphosis; • Growth retardation; • Small cold hands and feet; • Inappropriate laughing/screaming spells; • Diminished response to pain; • Intense eye communication – use of eye pointing.
Exclusion criteria for typical RTT	• Brain injury secondary to trauma, neurometabolic disease, or severe infection that causes neurological problems; • Grossly abnormal psychomotor development in first 6 months of life.

There is currently no cure for RTT, so the available treatment is palliative or supportive through multidisciplinary approaches [1], [4] and these patients tend to be highly dependent on their caregivers. They should receive support for communication and motor skills. Medication is usually indicated in response to the symptoms presented by patients, as there is no specific medication for RTT treatment. Non-pharmacological therapy is also often considered, as is the case of vagal nerve stimulation, Snoezelen multisensory approach, with or without hydrotherapy, placement of a gastrostomy tube, fundoplication, and surgical treatment of scoliosis [1].

1.1.2. Rett Syndrome Disease Modelling

It is particularly challenging to investigate and develop therapies for rare diseases, as there is a scarcity of patients. Animal models have made significant contributions to overcome this limitation, but more recently, with increasing knowledge regarding human pluripotent stem cells (hPSCs), they have emerged as a promising alternative for the study of RTT. Although RTT is a multi-systemic disorder, as mentioned, the loss of MeCP2 especially affects different stages of brain development and function, and, therefore, this is the most studied aspect of RTT.

1.1.2.1. Animal Models

Studies using animal models performed in the last decades, since the identification of MeCP2 as the main causative gene of RTT, have provided a considerable progress in understanding the mechanisms of RTT. Mecp2 is present in all vertebrates, but absent in non-vertebrate model organisms as fruit flies or worms [5], which makes Mecp2-mutant mice the animal model of choice. This section will focus on the progress made in RTT modelling with mice, as reviewed in [6].

Female Mecp2-mutant mice are the most clinically significant model, since, as previously mentioned, RTT incidence is higher in women. However, most studies rely on hemizygous Mecp2-mutant male mice, due to the advantages they present for mechanistic research, as they have a consistent phenotype and complete lack of Mecp2 protein.

Mouse models used in the RTT study include null alleles, point mutations, whole exon deletions, and conditional alleles. The two primary models [7], [8] are Mecp2-null models developed shortly after the identification of MeCP2 as the causative gene of the disease. Its significance comes from the fact that both mouse lines used exhibit a similar phenotype that mimics the human RTT symptoms, which allows the study of the mechanistic basis for disease.

Despite their relevance, null mouse models are not always representative, as numerous RTT patients carry, for example, missense mutations that do not result in a complete loss of the MeCP2 protein, but in a less-efficient or unstable one. To overcome this limitation and allow the study of clinically relevant mutations verified in RTT patients, mouse lines with point mutations and deletions in Mecp2 were engineered. Six of the eight point mutations that are most frequently found in RTT patients, including R106W, R133C, T158M, R168X, R255X and R306C, have an established mouse model capable of mimicking RTT symptoms [9]–[14]. Understanding the functional effects of RTT-causing mutations and how they report symptom severity has been mainly possible because of these models.

The expression level of the two Mecp2 isoforms varies between tissues, with Mecp2_e1 being more prevalent than Mecp2_e2 in the brain. Only the deletion of Mecp2_e1 was associated with RTT-like phenotypes and a reduced lifespan, according to studies that deleted either Mecp2_e1 or Mecp2_e2 across the body [15], [16].

Mouse models with conditional alleles crossed with transgenic mice carrying a tissue- or cell type-specific Cre to obtain temporal or spatial deletion of Mecp2 were also investigated. Neuronal dysfunction was once considered the only cause of RTT, so these studies were very relevant as they allowed to understand the role of Mecp2 in diverse tissues and cell types [7], [17], [18]. Additionally, temporal deletion of Mecp2 was used to study whether RTT phenotypic reversibility was possible, meaning whether Mecp2-deficient cells could be repaired. Guy et al. [18] showed that by first silencing Mecp2 and later activating it, the Mecp2-induced pathology was not permanent and symptom reversal was possible, namely neurological symptoms and normalized lifespan.

A broad spectrum of phenotypes observed in RTT patients that were mimicked using Mecp2-mutant mouse models, as well as distinctive aspects between humans and mice, are summarised in Table 1.3.

Table 1.3: Range of phenotypes observed in RTT patients that were mimicked using Mecp2-mutant mice and phenotypes observed only in RTT patients or in Mecp2-mutant mice. Adapted from [6].

Abnormality type	Shared features	Human	Mouse	References
Motor	• Reduced mobility; • Impaired motor coordination; • Ataxic gait; • Tremors.	• Stereotypic hand movements.	• Limb clasping.	[7], [8], [19]
Morpho-logical	• Reduced brain volume; • Neuronal hypotrophy.	• Kyphosis; • Scoliosis; • Osteoporosis.	• Hypotonia; • Malocclusion.	[20]
Behavioural	• Learning delays.	• Neurological regression; • Loss of speech; • Increased anxiety; • Social avoidance.	• Decrease anxiety; • Increased social behaviour; • Changes in startle response.	[21]–[26]
Metabolic	• Abnormal neurometabolites; • Increased serum cholesterol and triglycerides; • Abnormal mitochondrial structure; • Increased oxidative stress.	• Altered cerebrospinal fluid substrates; • Gallbladder inflammation.	• Fatty liver disease; • Insulin resistance.	[27]–[34]
Other	• Breathing irregularities; • Cardiac abnormalities (prolonged QT intervals); • Seizures; • Shortened lifespan.	• Gastrointestinal abnormalities; • Bruxism; • Sleep disturbances.	• Poor grooming.	[7], [35]–[38]

Currently, preclinical research is mainly divided into two approaches, namely targeting pathways downstream of Mecp2 or directly targeting Mecp2 and its protein product.

The identification of components that are found in pathways downstream of Mecp2 allowed the recognition of several targets with potential for treatment, enabling to improve neurotransmitter signalling [39]–[43], growth factor signalling [44]–[47], and metabolism [28]–[30], [48]–[50]. Although a number of treatments have ameliorated symptoms in Mecp2-mutant mice, it is still difficult to 1) identify the pathways that Mecp2 regulates, as its precise functions are still unknown; 2) understand the specificity of the treatment since Mecp2-regulated genes vary based on methylation status in distinct cell types; 3) distinguish between which pathways are affected as the primary result of Mecp2 loss and which are secondary effects.

The second approach, directly targeting Mecp2 and its protein product, is interesting as it allows all pathways downstream of Mecp2 to subsequently recover as well. Strategies include 1) directly targeting the Mecp2 mutation with small molecules called translational read-through-inducing drugs (TRIDs), which can favour the recovery of Mecp2 product; 2) reactivating the silent X-chromosome, which can restore endogenous Mecp2 to cells; and 3) introducing a normal copy of Mecp2 into cells by gene therapy. However, the line between having a therapeutic effect and causing other disorder types is tenuous. While a lack of MeCP2 can cause RTT, on the other hand, MeCP2 overexpression can induce

MeCP2 duplication syndrome, a condition that presents some RTT-like features as well as neurological dysfunction and intellectual incapacity [51].

Despite the advantages that animal models present, their clinical relevance is affected by the differences between species. In particular, the relevance of the male mouse model may be limited since it does not represent the features of female patients, the mainly affected ones. Additionally, the diversity among patients can hardly be modelled using mice. Therefore, there has been an increasing need for the employment of alternative models that more accurately resemble the severity and the features of RTT. Accordingly, *in vitro* cell models play a crucial role.

1.1.2.2. Human Pluripotent Stem Cell-derived Models

Cell culture is the method of studying the cells' behaviour outside the multicellular organism, free from systemic influences and under controlled conditions [52]. Accordingly, stem cells are a cell type widely used in cell culture, defined as the ones that have the ability to self-renew, maintaining the population pool, or to differentiate into a daughter cell [53]. Among stem cells, pluripotent stem cells are characterized by their ability to give rise to virtually every cell type derived from the three embryonic leaflets and (eventually) also to germ cells. Therefore, a pluripotent stem cell can give rise to virtually every cell in the organism, but it cannot develop into an entire organism on its own [54].

This section will address hPSC-derived models, as reviewed in [3]. Both human embryonic stem cells (hESCs), cells of the pre-implantation human embryo, as well as human induced pluripotent stem cells (hiPSCs), somatic cells that are induced to a primitive pluripotent state by transduction of specific transcription factors (Oct3/4, Sox2, Klf4 and c-Myc), are hPSCs [55], [56].

The use of hESCs raises many ethical issues regarding the usage of human embryos and concerns regarding immune rejection after transplantation of its derivatives [57]. Takahashi et al. [55] proved that hiPSCs were similar to hESCs in morphology, proliferation, surface antigens, gene expression, epigenetic status of pluripotent cell-specific genes, and telomerase activity. Thus, although hiPSCs are not identical to hESCs, the use of hiPSCs makes it possible to circumvent the aforementioned problems associated with hESCs.

As in animal models, the neurological features associated with RTT are the best documented in cell models. This was only possible due to the rapid progress in the field of hPSC culture, allowing, firstly, the development of 2D neuronal differentiation models and, subsequently, the generation of 3D brain models, constituting a more complex approach, while also better mimicking human neurodevelopment *in vitro* [3].

hPSC-derived RTT 2D Models

Although considered simplistic, hPSC-derived 2D models (Table 1.4) mimic various aspects of the morphological, functional and molecular RTT phenotypes, and have been particularly used to study the role of MeCP2 in neurons, either by directly altering neural function or by indirectly controlling other related-gene targets.

Marchetto et al. [58] were the first to develop a RTT hiPSC-based model. They found that RTT neurons displayed impaired maturation, including the presence of fewer synapses, smaller soma size, altered calcium signalling, and excitatory/inhibitory (E/I) imbalance. This disruption of the E/I activity balance between synapses resulted in an imbalance in microenvironmental homeostasis, which may trigger abnormal brain firing, causing epilepsy or other symptoms. In a similar approach, but using neurons derived from hiPSCs with a distinct mutation, Ananiev et al. [59] verified a smaller nuclear size in RTT neurons. Additionally, Kim et al. [60] found lower levels of both early-stage neurons and sodium channels when compared to control neuronal cultures. On the other hand, Djuric et al. [61] carried out the first study assessing the correlation between MeCP2 mutations and the two protein isoforms. Similar

to previous studies, RTT neurons presented a smaller soma size, decreased dendritic complexity and reduced cell capacitance. This impaired maturation was suggested as a consequence of defects in action potential (AP) generation that the authors hypothesized to be related with a decrease in voltage-gated sodium currents. Interestingly, the alteration in the form and function of the neurons, which only could be rescued by transgene-induced expression of MeCP2_E1, but not of MeCP2_E2, indicated that MeCP2_E1 is sufficient to cause these changes. Subsequently, more standardized and chemically defined methodologies were developed for neural differentiation of hPSCs, in particular, dual-SMAD inhibition [62] was applied for neuroectodermal specification of hiPSCs and hiPSC-based RTT modelling. For example, Fernandes et al. [63] revealed alterations in the number of neuronal projections obtained in RTT neurons, by employing a methodology based on the dual-SMAD inhibition protocol.

hPSC-derived 2D models have also been used in order to identify potential MeCP2 molecular targets. For instance, Choline, a precursor of membrane components, by increasing the frequency of spontaneous excitatory postsynaptic currents, was able to change the lipid profile of the membrane of RTT neurons, which in turn restored neuronal soma size and synaptic input [64]. Upon differentiation into RTT forebrain neurons, Bu et al. [65] demonstrated that these neurons exhibited phenotypic alterations, namely a smaller neuronal growth, a reduced dendritic complexity, and increased fragmentation and reduced mitochondrial membrane potential. Reduced levels of CREB, a transcription factor that indirectly regulates MeCP2 levels, were correlated with these observations. They also verified that the neuronal phenotype was rescued by improving CREB phosphorylation using Rolipram. Additionally, a reduced expression of the cell adhesion molecule L1 was found in RTT hiPSC-derived neural precursor cells, and correlated with decreased neuritogenesis in a study carried out by Yoo et al. [66], highlighting another role of MeCP2 as a molecular regulator. On the other hand, it is known that the neuron-specific K^+-Cl^- cotransporter 2 (KCC2), which inhibits the RE1-silencing transcriptional factor (REST), is an important downstream gene target of MeCP2 [67]. The downregulated expression of KCC2 in RTT hiPSC-derived neurons was associated with a defective GABA functional switch from excitation to inhibition. Tang et al. work presents a potential therapeutic approach for RTT based on KCC2 overexpression or insulin-like growth factor-1 (IGF-1) treatment, which plays a role in GABA functional switch. Several small molecules successfully restored the GABA functional switch, excitatory synapses and E/I balance by increasing the proper levels of KCC2 [68].

New insights regarding neurodevelopment and the molecular pathways involved in RTT have been uncovered through transcriptomic and proteomic analysis. Ohashi et al. [69] performed a study which revealed that the decrease in dendritic complexity of RTT neurons may be a consequence of p53 pathway activation, or be associated with ageing. In another study, Landucci et al. [70] suggested that the defects in the circuit of GABAergic neurons already mentioned may result from a Histone Deacetylase 6 (HDAC6) overexpression, which in turn induces an atypical reduction in acetylated α-tubulin. Importantly, a study developed by Varderidou-Minasian et al. [71] suggested that RTT alterations in proteins involved in a number of signalling pathways occur early during neurodevelopment, long before RTT symptoms become apparent. Sharma et al. [72] demonstrated in another pioneering study that exosomes extracted from healthy cells, which carry the signalling information required to regulate the development of neural circuits, can attenuate RTT neural impairments. Lastly, on the other hand, Xiang et al. [73] intended to evaluate the effect of MeCP2 mutations specifically in hiPSC-derived interneurons (INs), verifying a decrease in neurite growth and a decreased soma size in RTT INs, as well as defects in electrophysiological properties, including an absence of discharging APs and a low degree of synchronization. INs displayed an extensive dysregulation in gene expression, mainly related with biological processes associated with axon/dendrite growth, synapse development and ion channel activities.

hiPSC-derived RTT 3D Models

In addition to the use of 2D strategies, RTT modelling through 3D models of the human brain, whether using scaffold-based 3D models or brain organoids has also been carried out more recently (Table 1.4).

Scaffold-based 3D models. Zhang et al. [74] suggested intrinsic impairments in RTT neural progenitor cell (NPC) migration, as well as impaired neurite outgrowth and lower synapse punts in RTT neurons after maturation. Their model consisted in a layered hydrogel, the cross-linkable methacrylate-modified hyaluronic acid, which, by mimicking the extracellular matrix (ECM) composition, increased cell-to-cell interactions and promoted neuronal maturation. In order to explore the impact of electrical stimulation in neuronal maturation of RTT hiPSC-derived NPCs, Nguyen et al. [75], using a conductive 3D graphene scaffold, suggested a potential improvement in the RTT phenotype at the initial stage of neuronal maturation, as RTT neurons demonstrated increased levels in neurogenesis markers and enriched soma size.

Brain organoids. Mellios et al. [76] conducted the first study concerning a 3D *in vitro* RTT organoid model derived from hiPSCs, with the aim of assessing whether MeCP2 has a regulatory impact during neurogenesis and further neuronal differentiation. In fact, impairments in neurogenesis, for example verified by an increased number of neural progenitors and reduced cell migration distances, as well as reduced dendritic complexity were observed in RTT organoids. Additionally, this study also suggested that MeCP2 mutations may have major implications on microRNA (miRNA)-mediated pathways, which in turn affect neurogenesis and neural differentiation. The pathological phenotype of RTT neurons could be relieved by restoring miRNA expression in patients with RTT and MeCP2-deficient neural cells [76], [77]. In another study, Xiang et al. [73] generated cortical organoids to assess the impact of the JQ1 compound to rescue RTT-like pathological phenotypes. A significant reduction in the number of dysregulated genes in both neuron and glia populations was shown after treatment with JQ1. Overall, this RTT brain organoid model allowed studying in detail the role of MeCP2 as a transcriptional regulator in various neural populations, throughout a range of developmental time periods and across different regions of the organoids. Lastly, in order to mimic RTT throughout neuronal development and maturation, Gomes et al. [78] generated brain organoids from hiPSCs that mimic sub-regions of the forebrain, including the ventral and dorsal ones. This model allowed to identify a premature development of the deep-cortical layer of RTT forebrain organoids and functional impairments in RTT neurons, including deficits in calcium signalling and electrophysiology analysis, with abortive-like APs, reduced AP amplitude, decreased AP velocity and absence of spontaneous synaptic transmission. Additionally, the assembly of RTT dorsal and ventral organoids showed deficits of IN's migration. Importantly, this brain organoid model was able to reveal mutation-dependent changes in the RTT phenotype. Overall, the advantages these organoids present have triggered an interest in generating other region-specific brain organoids to assess how MeCP2 mutations impact further brain regions.

Summing up, modelling RTT using 2D and 3D culture platforms has undoubtedly improved the understanding about this disease. Regarding neuronal morphology-related alterations, both RTT model types evidence mostly changes in synapses, dendrites and neuronal projections. Similar neuronal functionality-related alterations have been seen in RTT models, including calcium signalling impairments and deficits related with AP generation. Regarding RTT-associated molecular alterations, changes in molecules linked to cell stress and apoptosis, and involved in synaptic function in both 2D and 3D RTT models stand out.

Table 1.4: Main research progress using RTT hPSC-derived 2D and 3D models. (Ref) References.

	Time	Researchers	Mutation type	Main research	Ref
2D Models	2010	Marchetto et al.	T158M, R306C, Q244X, 1155del32	Establishment of the first RTT hiPSC-based model, verifying fewer synapses, smaller soma size, altered calcium signalling and E/I imbalance.	[58]
	2011	Ananiev et al.	T158M, V247X, R306C, R294X	Identification of a smaller nuclear size in RTT neurons.	[59]
	2011	Kim et al.	T158M, Q244X, E235fs, R306C, X487W	Identification of lower levels of both RTT early-stage neurons and sodium channels when compared to controls.	[60]
	2015	Djuric et al.	MeCP2_E1	Establishment of the first study correlating MeCP2 mutations and the two protein isoforms. MeCP2_E1 mutations caused an alteration in the form and function of neurons.	[61]
	2015	Fernandes et al.	R306X	Identification of alterations in the number of neuronal projections.	[63]
	2016	Chin et al.	R306C, 1155del32	Some RTT neuron impairments could be restored by Choline supplementation.	[64]
	2016	Tang et al.	Q83X	MeCP2 mutation affected KCC2 expression, leading to a GABAergic neuron dysfunction.	[67]
	2017	Bu et al.	T158M, V247fs	Rescue of neuronal phenotype was possible by increasing CREB phosphorylation using Rolipram.	[65]
	2017	Yoo et al.	Q83X	Increased MeCP2 and L1 expression in RTT neural precursor cells might regularize impaired neuritogenesis.	[66]
	2018	Ohashi et al.	705delG, X487W	Activation of the p53 pathway, or ageing, might lead to a reduction in the dendritic complexity of RTT neurons.	[69]
	2018	Landucci et al.	T158M, R306C	HDAC6 overexpression might impair the circuit of GABAergic neurons.	[70]
	2019	Sharma et al.	Q83X	Exosomes extracted from healthy cells could attenuate RTT neural impairments.	[72]
	2020	Varderidou-Minasian et al.	MeCP2 exons 3–4 mutation	RTT alterations in proteins involved in several signalling pathways occurred early during neurodevelopment.	[71]
	2020	Xiang et al.	R133C, R270X, R306C	Identification of adverse effects in the morphology and electrophysiological properties of MeCP2 mutant cortical INs.	[73]
3D Models	2016	Zhang et al.	Q83X, N126I	Scaffold-based 3D model suggesting RTT NPC migration impairment and deficits in neurite outgrowth and lower synapse punts in RTT neurons.	[74]
	2018	Nguyen et al.	1155del32	Electrical stimulation had an impact on neuronal maturation of RTT hiPSC-derived NPCs using a scaffold-based 3D model.	[75]
	2018	Mellios et al.	R106W, V247X	Establishment of the first 3D *in vitro* RTT organoid model derived from hiPSCs. MeCP2 mutations seemed to have a strong impact on miRNA-mediated pathways, which in turn affected neurogenesis and neural differentiation.	[76]

2020	Xiang et al.	R133C, R270X, R306C	Evaluation of the impact of the JQ1 compound to rescue RTT-like pathological phenotypes using cortical organoids.	[73]
2020	Gomes et al.	R255X, Q83X	A premature development of the deep-cortical layer of RTT forebrain organoids and functional impairments in RTT neurons were shown. Deficits of IN's migration were found by the assembly of RTT dorsal and ventral organoids.	[78]

1.2. Rett Syndrome and Cardiac Defects

Besides presenting neurological complications, RTT patients suffer from a wide array of non-neurological problems, including cardiac abnormalities. They include severe sinus bradycardia or sinus pauses [79], prolonged corrected QT interval (QT_c, an adjusted QT interval based on heart rate) and T-wave abnormalities [36], [80]–[86], ventricular tachycardia [84], and subclinical biventricular myocardial dysfunction [87].

RTT patients have a higher incidence of sudden and unexpected death, about 26% of all deaths [88], compared to individuals of the same age without pathology. Published data about biochemical, electrophysiological, or pathological changes in RTT patients who have suffered from sudden death are scarce [89]. Although not consensual, a speculated factor that potentiates this sudden death in RTT is prolonged QT_c, which represents a prolongation of repolarization, a condition that affects between 7% and 55% of RTT patients [36], [80], [83], [85], [89], [90]. According to some studies, certain MeCP2 mutations, namely R255X, T158M, or significant deletions, may be more likely to predispose to QT_c prolongation [89], [90]. In the literature, data is mixed regarding the association of prolonged QT_c with other parameters, such as age and clinical severity in RTT, showing the need for further studies to elucidate these associations [89]. It remains unknown whether a prolonged QT_c in RTT patients is a direct effect of RTT on the heart or a secondary effect of the RTT nervous system manifestations [85]. On one hand, some researchers suggest that sudden deaths may be due to prolonged QT_c-related ventricular arrhythmias [85], [89], specifically, repolarisation-related ventricular tachyarrhythmias, such as torsade de pointes and ventricular fibrillation [85]. On the other hand, dysautonomia, a condition in which the autonomic nervous system (ANS) does not function properly and can affect organs such as the heart [91], is associated with reduced heart rate variability, which in turn may be also a potential cause of prolonged QT intervals and, therefore, a sudden death enhancer [92].

1.2.1. Modelling Rett Syndrome using Cardiac Models

Until now, there are no publications in the literature reporting the modelling of RTT with cardiac models derived from patient-specific hiPSCs. However, *in vitro* and *in vivo* mouse models of RTT have been applied to study the cardiac component of the pathology, as these animals present a prolonged QT_c and are susceptible to ventricular tachycardia and sudden cardiac death [36], [93], [94].

Although Mecp2 is not essential for induction of cardiac differentiation, it contributes to the development and further differentiation of cardiovascular progenitors during mouse embryonic stem cell (ESC) differentiation. Several genes with the potential to affect cardiac development and differentiation were found to be highly dysregulated during Mecp2-null ESC differentiation, including, for example, the ones essential for the early mesoderm development. Additionally, the expression of various genes that are crucial for the maintenance of heart homeostasis and its adaptation to pathologic states is directly or indirectly regulated by Mecp2. Indeed, alterations of endogenous gene expression

were also verified in the Mecp2-null mouse heart. Especially, the abnormal expression of voltage-gated channel genes was found to cause arrhythmias in Mecp2-null mice [37]. These alterations may result from Mecp2 deficiency per se or may also be a consequence of this lack of Mecp2 together with multiple factors, including autonomic dysfunction, mild hypoxia, mitochondrial abnormality, and oxidative stress [95]–[98].

Regarding the effects on cardiac ultrastructures, Mecp2 deficiency causes intercellular communication impairment in cardiomyocytes (CMs), with lower levels of Cx43 and N-cadherin proteins being found in Mecp2-null ventricle and less developed intercalated discs in Mecp2-null mice. Additionally, Mecp2 deficiency has been shown to cause cardiac pathological stress, which might have promoted autophagic activity. In turn, the accumulation of autophagic vacuoles might be related to an alteration in the conductive properties of Mecp2-null hearts [37]. As mentioned for the alterations in gene expression, these changes might be a consequence of Mecp2 deficiency per se or might also be related to the lack of Mecp2 together with multiple factors [95]–[98].

Mecp2 deficiency has been also reported to cause changes in the conductive properties of the heart, with shorter RR [37], [99] and PQ [37] intervals, as well as QT_c [36], [94], [99], [100] and QRS [36], [37], [100] prolongation in Mecp2-null mice. Particularly, comparing the QT_c and QRS parameters between male- and female-null mouse models, the QT_c and QRS prolongation in females become apparent at older ages [36], similar to what occurs in RTT patients. RTT mice also showed increased susceptibility to induced ventricular tachycardia. Especially, this susceptibility is age-dependent in female mice, being considerably higher in the older animals. According to that, McCauley et al. suggested that male- and older female- null mice with QT_c prolongation were at risk for arrhythmia-induced death [36]. Posteriorly, a lower survival rate in Mecp2-null compared to wild-type (WT) mice [37], as well as death associated with spontaneous cardiac arrhythmias and complete conduction block in another Mecp2-null mouse model [94], were also reported.

Possible treatments of QT_c prolongation and their effectiveness in preventing arrhythmias in RTT patients were studied. Treatment with β-adrenergic receptor blockers, the standard therapy for prolonged QT_c in RTT, did not prevent ventricular tachycardia in Mecp2-null mice [36], [94]. On the other hand, it has been demonstrated that prolonged QT patients with sodium channelopathies have a poor response to β-adrenergic receptor inhibition, whereas those with potassium channelopathies respond well, making it an effective antiarrhythmic prophylactic therapy [101]. This suggests that two distinct mechanisms are involved in the processes by which sodium and potassium channelopathies cause prolonged QT. Taking that into consideration, it was performed a characterization of Mecp2-null mice CMs, where a persistent increase in "late" sodium current ($I_{Na,Late}$) was found [36], [100], which was normalized when cells were treated with phenytoin, a sodium channel blocking anti-seizure drug [36]. Phenytoin treatment reduced QT_c and sustained ventricular tachycardia in Mecp2-null mice, suggesting that an alteration in $I_{Na,Late}$ underlies prolonged QT_c and the susceptibility to ventricular arrhythmia in RTT mice [36], [94]. In addition, RTT patients treated with anticonvulsants which block sodium channels demonstrated improvements in QT interval [94]. More recently, the poorly understood effects that loss of Mecp2 function has on ventricular APs have begun to be addressed. APs from ventricular myocytes were found to be prolonged in a male [100] and a female [99] Mecp2-null mouse models, obtaining AP duration at 75% of complete repolarization (APD_{75}) increased in males [100] and APD_{90} increased in both males [100] and females [99] compared to controls; as well as showing augmented triangulation, meaning a greater difference between APD_{25} and APD_{90} [99], [100]. Interestingly, APD_{90} instability was found to be greater in Mecp2-null male myocytes than that for control ones [100], with increased AP instability being described in the literature as a pro-arrhythmic marker [102], [103]. In the same studies, the $I_{Na,Late}$ inhibitor GS-6615 shortened the APs in RTT ventricular myocytes, reversing, at least partially, delayed repolarization, indicating that may potentially be used against QT_c prolongation in RTT [99], [100].

The persistent increase in $I_{Na,Late}$, prolonged QT_c, ventricular tachycardia, and sudden cardiac death appear to be a consequence of the loss of Mecp2 function in the nervous system of RTT mice and not in the CMs themselves. This was unexpected, as prolonged QT_c reflects the change in the repolarization properties of the CMs themselves. In particular, the genetic causes of idiopathic QT prolongation result from mutations in genes encoding proteins within CMs that control the electrical properties of these cells [36]. In addition, the conditional removal of Mecp2 in cholinergic neurons was sufficient to mimic cardiac rhythm defects in RTT mice. Indeed, Mecp2 restoration in cholinergic neurons was able to rescue spontaneous and induced cardiac arrhythmias, prolonged QT_c, and significantly impacted survival. These results suggest that cardiac autonomic control was altered as a consequence of Mecp2 deficiency mainly via the cholinergic nervous system. In that regard, it was also shown that treatment with the parasympathetic antagonist atropine reduced cardiac arrhythmias in RTT-mutant mice [104].

Overall, this proved to be of great relevance, as there is evidence that Mecp2 is an important regulator of cardiac gene expression and the persistent increase in $I_{Na,Late}$, prolonged QT_c, ventricular tachycardia, and sudden cardiac death appear to be a consequence of the loss of Mecp2 function.

Interestingly, patients who suffer from another neurodevelopmental disorder also present cardiac abnormalities and, contrary to RTT, there are already induced pluripotent stem cell (iPSC)-derived cardiac models for the study of this disease. Timothy syndrome (TS) is a rare multi-organ autosomal dominant disorder that results from L-type calcium channel $Ca_V1.2$ missense gain-of-function mutations in the CACNA1C gene. TS patients suffer from several problems such as cardiac arrhythmias, namely long QT syndrome and ventricular tachycardia, congenital heart disease, syndactyly, developmental delays and neurological abnormalities. The life expectancy of those diagnosed is 2.5 years, usually dying as a consequence of lethal ventricular tachyarrhythmias. In most cases, developmental delays in language, motor skills, and cognitive function are characteristic of children who survive past 2.5 years [105]. Yazawa et al. explored the TS mutation effect on the electrical activity and contraction of CMs using TS iPSC-derived CMs. These cells showed irregular contraction, prolonged APs and irregular electrical activity, with excess calcium influx and abnormal calcium transients [106], consistent with the heart defects of TS patients. It was suggested that mutations identified in TS alter multiple channel properties, such as a near complete loss of voltage-dependent channel inactivation, resulting in calcium overload. Additionally, roscovitine, a cyclin-dependent kinase (CDK) inhibitor and L-type $Ca_V1.2$ channel blocker [107], restored the electrophysiological and calcium signalling properties in TS iPSC-derived CMs [106]. Although it remained unclear how exactly roscovitine rescued the phenotypes in these cells, posteriorly it was shown that roscovitine exhibited its therapeutic effects in part by inhibiting CDK5, suggesting a potential therapeutic mechanism to alleviate cardiac phenotypes [108].

1.3. Embryonic Heart Development and Adult Heart

A new organism begins to form as a result of fertilisation. The division of blastomeres from the zygote enables a single fertile cell to continue to cleave and differentiate until a blastocyst forms. Blastomere differentiation allows the development of two distinct cell populations: the outer cell mass (or trophectoderm) and the inner cell mass. The outer cell mass originates the trophoblast, giving rise exclusively to the placenta, and the inner cell mass originates the embryoblast, meaning all the cells of the organism and some extra-embryonic cells [54].

The embryoblast evolves from a continuous epithelial sheet of cells into a multi-layered structure known as the gastrula. This is a trilaminar structure comprising the three germ layers, the ectoderm, mesoderm, and endoderm. The 1) ectoderm will give rise to all outer surface cells and the central and peripheral nervous system (CNS and PNS, respectively); the 2) mesoderm will give rise to

connective tissue, supporting tissues (skeletal and cartilaginous), muscles, heart walls, blood cells, the serous membranes lining the body cavities, among others; and the 3) endoderm will give rise to the inner linings, the epithelium of the digestive tube, respiratory tube, and pharynx [109].

Cardiac development (Figure 1.2) starts at the end of the second week of human development, in which gastrulation occurs. The heart is one of the first organs to form and function during embryogenesis. It is, almost entirely, an organ derived from the mesoderm, a layer that, along with endoderm, emerges from a transient structure known as primitive streak (PS) [110]–[112]. Mesoderm differentiates into three different subtypes, namely the 1) paraxial mesoderm; the 2) intermediate mesoderm; and the 3) lateral mesoderm, which, in turn, consists of two layers, the somatic and the splanchnic layer. Cardiac precursors of the heart arise from the splanchnic layer, localized in the mid PS and facing the endoderm [113].

The heart begins to develop from the first mesodermal cells, which migrate from the PS towards the anterior part of lateral plate mesoderm [110], [113]. The cardiac precursor pool, originating from the first mesoderm cells, can be divided into two groups of cells, 1) cells that will form the primitive heart tube and 2) cells that will be added to this linear heart tube at a later developmental stage. These two populations are known as the first and second heart fields (FHF and SHF), respectively [110], [111].

The cardiac crescent, or heart-forming region, is the first cardiac compartment that is morphologically identifiable during development. The ventral part of the cardiac crescent is constituted by migrating FHF progenitors, whereas the SHF progenitors are located posteriorly and medially to the FHF pool, in the cardiac crescent [111], [114]. Different signals are presented to the FHF and SHF progenitors, which will influence the fate of those cells.

By embryo folding, the two symmetric lateral mesoderm parts of the cardiac mesoderm are brought together. Thus, the horseshoe-shaped cardiac crescent forms a tube with one cranio-medial outlet, or arterial pole, and two caudo-lateral inlets, or venous pole. At this phase, the developing heart acquires the shape of an inverted Y [110], [111]. The FHF progenitors, which form the primitive heart tube, originate only cells with a cardiogenic fate. This primitive heart tube is organized in an outer layer of CMs and an inner layer of endocardial cells, separated by an ECM (cardiac jelly), which eventually starts to contract, pumping blood and nutrients throughout the embryo [110], [115]. The SHF progenitors are a proliferative cell population, which migrate either towards the primitive heart tube or, later on, into the looping heart tube. These give rise to the elongation at the inflow and outflow poles of the heart structure. Additionally, contrarily to FHF progenitors, SHF progenitor cells are multipotent, originating from an extra-cardiac precursor pool, which differentiate into both CMs and cardiovascular cells [111], [116], [117].

The heart tube changes into the shape of the heart through a process called cardiac looping, where each heart field contributes differently to the various regions and chambers of the heart. On the one hand, the FHF-derived heart tube seems to give rise to most of the left ventricle (LV) CMs and portions of the right and left atria (RA and LA, respectively). On the other hand, the SHF appears to result in the outflow tract (OFT), right ventricle (RV) CMs and the majority (two-third) of atrial myocardium [110], [114], [118]. Subsequently, the septa, which separate atria and ventricles from one another, are formed, as well as the atrioventricular valves, which provide one-way flow and prevent back flow through chambers. The heart continues to progress in development and acquire the appearance we know, of an organ composed of four chambers. Inflow tracks, consisting of superior vena cava, inferior vena cava and coronary sinus, as well as outflow tracks, consisting of aortic arch and pulmonary trunk, are then formed [110], [111], [113].

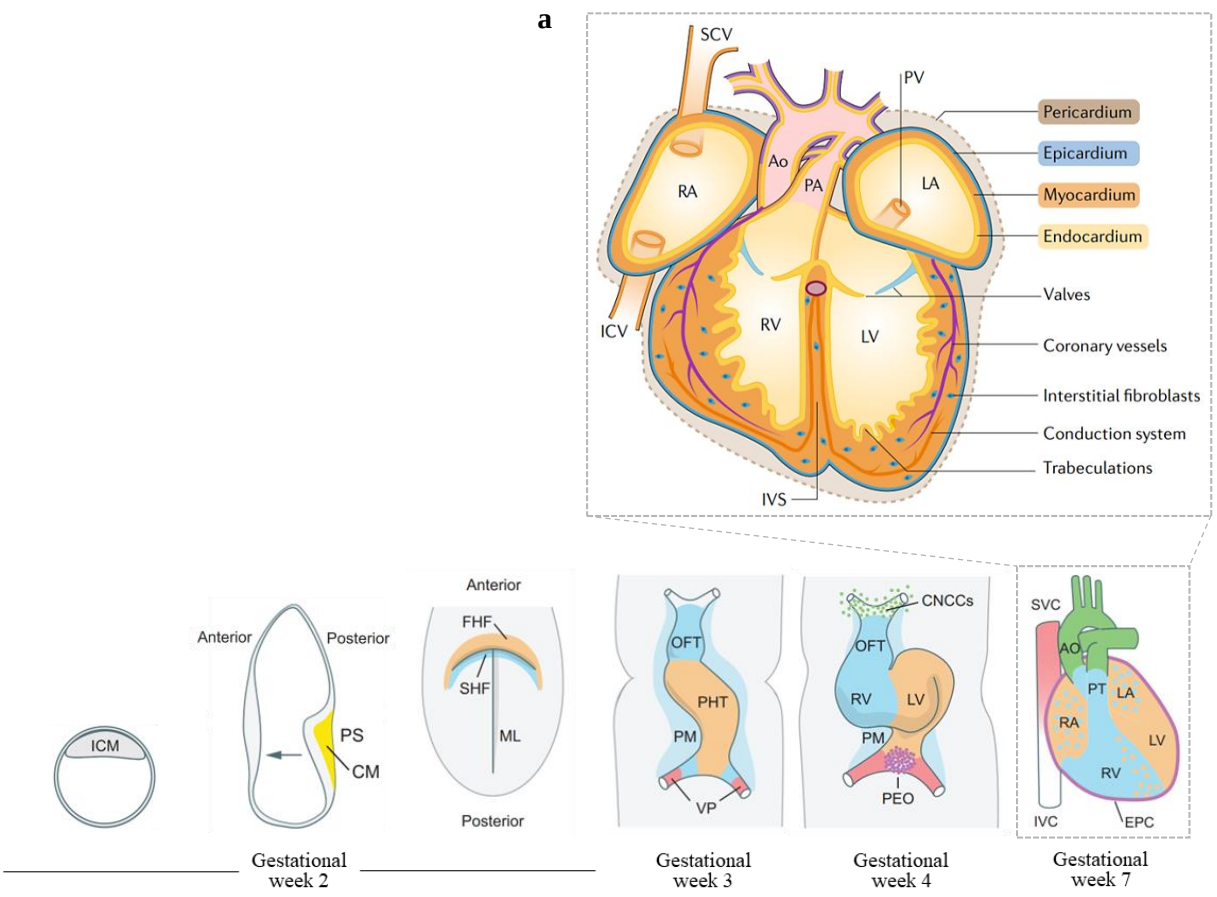
a
SCV
PV
Pericardium
Epicardium
Myocardium
Endocardium
Ao
PA
RA
LA
Valves
ICV
RV
LV
Coronary vessels
Interstitial fibroblasts
Conduction system
Trabeculations
IVS
Anterior
Posterior
ICM
PS
CM
FHF
SHF
ML
OFT
PHT
PM
VP
CNCCs
RV
LV
PEO
SVC
AO
PT
LA
RA
LV
RV
IVC
EPC
Gestational week 2
Gestational week 3
Gestational week 4
Gestational week 7
I
II
III
IV
V
VI
Gastrulation
Migration of the first mesodermal cells towards the anterior part of lateral plate mesoderm
Formation of the cardiac crescent
Fusion of the two lateral mesoderm parts, giving rise to the primitive heart tube with two poles
Heart looping
Chamber formation

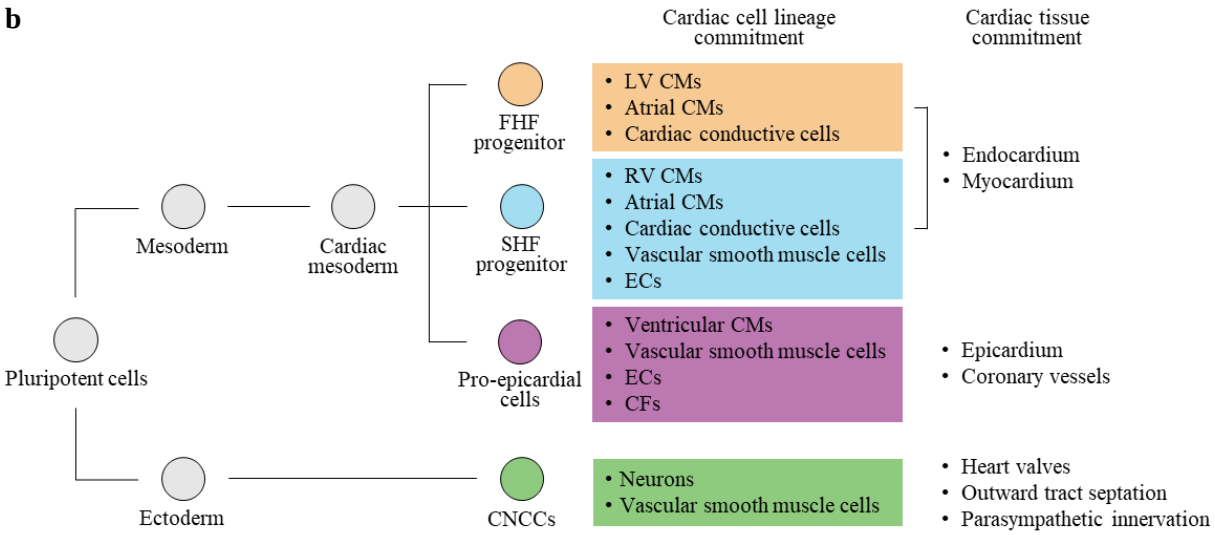
b
Cardiac cell lineage commitment
Cardiac tissue commitment
Pluripotent cells
Mesoderm
Cardiac mesoderm
Ectoderm
FHF progenitor
SHF progenitor
Pro-epicardial cells
CNCCs
• LV CMs
• Atrial CMs
• Cardiac conductive cells
• RV CMs
• Atrial CMs
• Cardiac conductive cells
• Vascular smooth muscle cells
• ECs
• Ventricular CMs
• Vascular smooth muscle cells
• ECs
• CFs
• Neurons
• Vascular smooth muscle cells
• Endocardium
• Myocardium
• Epicardium
• Coronary vessels
• Heart valves
• Outward tract septation
• Parasympathetic innervation

Figure 1.2: Heart development. Schematic representation of **(a)** cardiogenesis stages in humans and **(b)** cardiac cell lineage and specification during development. (AO) aorta; (CFs) cardiac fibroblasts; (CM) cardiogenic mesoderm; (CMs) cardiomyocytes; (CNCCs) cardiac neural crest cells; (ECs) endothelial cells; (EPC) epicardium; (FHF) first heart field; (ICM) inner cell mass; (LA) left atrium; (LV) left ventricle; (ML) midline; (PA) pulmonary artery; (PEO) proepicardial organ; (PHT) primitive heart tube; (PM) pharyngeal mesoderm; (PS) primitive streak; (PT) pulmonary trunk; (PV) pulmonary vein; (OFT) outflow tract; (RA) right atrium; (RV) right ventricle; (SHF) second heart field; (SVC) and (IVC) superior and inferior vena cava, respectively; (VP) venous poles. Adapted from [112],[119],[120].

The adult heart is located in the thoracic cavity [121], and comprises four chambers, the LA, RA, LV and RV. It is delimited by a cardiac wall composed of the 1) endocardium, the inner endothelial layer; the 2) myocardium, the intermediate layer; and the 3) epicardium, the outer epithelial layer that covers the myocardium [120]–[123]. The endocardium keeps blood in the heart antithrombotic, acts as a barrier between blood and tissue, continues as endothelium in blood vessels, and lines the outer layer of the valves in the heart. The myocardium generates and conducts APs, and contracts as a unit to pump blood through and out of the heart. The epicardium secretes pericardial serous fluid into the pericardial cavity to lubricate tissue layers [121].

The adult human heart is made up of different cell types, including four major ones, namely 1) CMs; 2) cardiac fibroblasts (CFs); 3) vascular cells, which comprise endothelial cells (ECs) and mural cells (pericytes and smooth muscle cells); and 4) immune cells (Table 1.5). Other minor populations include 5) adipocytes; 6) mesothelial cells; and 7) neuronal cells [124]–[126]. Although the most significant populations that constitute the adult human heart are CMs, FBs, vascular cells and immune cells, the distributions of these major cell types differ between atrial and ventricular tissues. However, in both cases, CMs are the most prevalent cardiac cells, comprising a higher percentage in the ventricles than in the atria. Even during embryonic development, CMs are always the most relevant cardiac cell population, despite their proportion drastically decreases (about 36%) during the developmental period, counterbalancing with the increase of the non-CM cell population [124], [125]. CMs are mainly divided into three subtypes, including atrial-like, ventricular-like, and nodal-like CMs. Each of these CM subtypes acquires distinct features during cardiac development, reflecting differences in electrophysiological, contractile and secretory processes. While nodal-like CMs are autonomic and conductive and mainly control the cardiac rhythmic activity, atrial-like and ventricular-like CMs mainly perform contractile functions as working cells [124], [125], [127], [128]. Regarding non-CMs, CFs, ECs and immune cells represent a higher percentage of cardiac cells in the arterial tissue compared to the same population in the ventricular tissue. Additionally, CFs are more abundant compared to mural cells in the atrial tissue and the opposite occurs in the ventricular tissue [124], [125].

Table 1.5: Main cardiac cell types in the adult human heart and their functions.

Cell type	Function
CMs	CMs are the contractile myocytes of the cardiac muscle.
CFs	CFs provide structural support for cardiac cells, through ECM production.
ECs	ECs line the interior surfaces of the heart chambers and blood vessels and regulate exchanges between the bloodstream and the surrounding tissues.
Mural cells	Mural cells are important to stabilize vessels and to regulate blood flow.
Immune cells	Macrophages are the major population of immune cells, but their specific function in normal conditions is still not fully understood. However, it is hypothesized that they may contribute for the normal conduction system of the heart.

The heart is innervated by the sympathetic and parasympathetic branches of the ANS, modulating heart rate and conduction velocity primarily via cardiac pacemaker tissue. Additionally, atrial and ventricular CMs are innervated by sympathetic nerves, which impact the force of contraction and relaxation. The human development of cardiac autonomic innervation begins around the fifth week post-conception [109], [129], [130]. However, knowledge regarding the development of cardiac autonomic innervation in humans is very limited, particularly concerning the cardiac parasympathetic system. Therefore, the information presented below refers exclusively to studies using animal models, as reviewed in [131].

Although cardiac autonomic neurons share a neural crest origin, they undergo distinct developmental differentiation as they mature toward their adult phenotype. The development of cardiac autonomic innervation can be divided into four distinct phases: 1) neural crest cell (NCC) migration and ganglia formation; 2) differentiation of NCCs into neurons; 3) aggregation/migration of neurons to form either the paravertebral sympathetic chains or the parasympathetic cardiac ganglia; and 4) extension of axonal projections into cardiac tissue and terminal differentiation. Parasympathetic innervation is functional before sympathetic system [130].

Cardiac sympathetic system. Thoracic NCCs migrate from the neural tube to near the developing dorsal aorta. It appears that this migration involves repulsive cues through signalling from the transmembrane protein neuropilin and Eph-ephrin. NCCs aggregate and differentiate close to the developing dorsal aorta before their final migration to paravertebral sympathetic ganglion sites. NCC differentiation occurs as a consequence of a series of transcriptional events initiated by bone morphogenetic proteins (BMPs) released from the dorsal aorta [109], [130], [132]. Particularly, some transcription factors of relevance include Phox2b, Ascl1/Mash1/Cash1, Phox2a, Gata2/3 and Hand2 [130], [133]. The final migration to paravertebral sympathetic ganglion sites is possibly driven by artemin, a member of the glial cell line-derived neurotrophic factor (GDNF) family, which is followed by a period of rapid mitosis [132]. Sympathetic nerves reach the heart through the vasculature, in a process during which neurotrophin-3 (NT-3) is secreted by the smooth muscle cells of the blood vessel. NT-3 dependence for local axonal growth of post-mitotic sympathetic neurons switches to nerve growth factor (NGF) dependence once the axons reach the heart. On the other hand, artemin and endothelin-3 seem to be important in sympathetic axonal guidance to their targets [132], [134], [135]. Once sympathetic nerves reach their targets in the heart, NGF is also important for neuronal survival and patterning, in addition to its significance for local axonal growth. By promoting the development of terminal varicosities, NGF enhances synaptic strength between sympathetic neurons and CMs. Indeed, the level of NGF in the adult mouse heart has been proved to be an indicator that helps to understand the extent of sympathetic innervation [132], [136], [137]. Interestingly, NGF expression in CMs may be promoted by endothelin-1, with significant reductions in cardiac innervation having been shown in endothelin-1-deficient mice [138].

Cardiac parasympathetic system. NCCs to be specified into parasympathetic cardiac ganglia migrate from the neural folds at the level of the hindbrain. The available data suggest that these NCCs may rely on semaphorins for attractive cues during their migration. Contrary to the sympathetic system case, these NCCs do not aggregate near the developing dorsal aorta but enter the heart along tracts laid down by the vagus nerve [132], [139]. Interestingly, it seems that these NCCs also contribute to the development of the OFT and aortic arches, composing the cardiac neural crest, briefly mentioned above [140]. Similar to what occurs in the developmental process of sympathetic neurons, NCC differentiation happen as a consequence of a series of transcriptional events initiated by BMPs. However, there are fundamental differences, namely the fact that neither Gata3 nor Hand2 are, in this case, relevant transcription factors [141]. Additionally, GDF and neurturin, a member of the GDNF family, are suggested to be involved in the trophic support and patterning of cardiac parasympathetic innervation [132].

1.4. *In Vitro* Platforms for Cardiomyocyte Differentiation and Neuro-Cardiac Co-culture

Through indirect or direct manipulation of different signalling pathways, it is possible to differentiate and maintain cardiac cells from hPSCs, with CMs being the most studied [122], [127], [128], [142].

CM differentiation protocols are based on the manipulation of the main regulatory signalling processes involved in cardiogenesis *in vivo*, including wingless integrated (Wnt), fibroblast growth factor (FGF) and transforming growth factor-beta (TGF-β), such as BMPs, Nodal and Activin signalling pathways. To achieve that, exogenous growth factors and/or small molecules at a specific concentration are used and added in a stepwise manner [142]. The combination of Activin/Nodal, BMP, FGF and Wnt signalling activation allows mesoderm induction from hPSCs, whereas the inhibition of Wnt signalling allows to successfully generate cardiac mesoderm and hPSC-derived CMs from mesoderm progenitors. BMP and Wnt signalling are particularly important in activating cardiac mesoderm specification, with FGF and Activin signalling expected to be active, either by direct exogenous stimulation or by indirectly stimulating through BMP and Wnt signal modulation [122]. On the other hand, temporal modulation of solely Wnt signalling by small molecules in a very specific and controlled manner, first activating this pathway for mesendoderm induction, followed by a step of Wnt inhibition for cardiac lineage specification, has been also extensively explored to specify hPSC-derived CMs [143]. Among these molecules, the examples of the glycogen synthase kinase 3 (GSK3) inhibitor CHIR99021 for mesoderm induction and the inhibitor of Wnt production 4 (IWP-4) for cardiac lineage specification can be mentioned. In addition to the manipulation of the referred signalling pathways, the success of the cardiac commitment process relies on other culture parameters, including the cell confluence at the beginning of differentiation and the cell density. CM-specific markers, such as cardiac troponin T (cTnT) and/or α-actinin, which are encoded by the TNNT2 and ACTN1 genes, respectively, are generally used to assess the CM differentiation efficiency.

Since there are different subtypes of CMs, the knowledge regarding how to manipulate the differentiation process, in terms of specific markers and signalling pathways, to obtain each of these CMs is essential (Figure 1.3). Indeed, the combination of higher levels of Activin A (ActA) and BMP with lower levels of Wnt during lateral mesoderm commitment favour FHF generation and, posteriorly, the LV CM specification. On the other hand, lower levels of ActA, as well as BMP, in the presence of Wnt activation favour, firstly, the SHF progeny and, then, the RV CM specification, through Wnt inhibition. Particularly, if there is the activation of the retinoic acid pathway during or after the Wnt inhibition, the specification of the atrial CMs is favoured. Additionally, the conjugation of this retinoic acid activation with BMP activation allows the sinoatrial node CM generation [122].

There are two culture formats used in the strategies for CM generation from hPSCs, namely 2D adherent monolayer or/and 3D culture. *In vitro* differentiation protocols of both culture formats rely on the same signalling and gene expression pathways required *in vivo* [144], [145].

The embryoid body (EB) differentiation method was used in the first attempts to differentiate CMs from hPSCs in a 3D environment. However, the fact that this method relies on the spontaneous and uncontrolled hPSC differentiation, culminates in the generation of a highly variable structure with differentiated cells of all three germ layers, where CMs may or may not be present. Therefore, although it has provided information unknown until then, the EB differentiation method is neither robust nor efficient [146]. Subsequently, CM differentiation from hPSCs in 3D culture was studied using directed differentiation protocols [147]–[150], which rely on the manipulation of signalling pathways as discussed above.

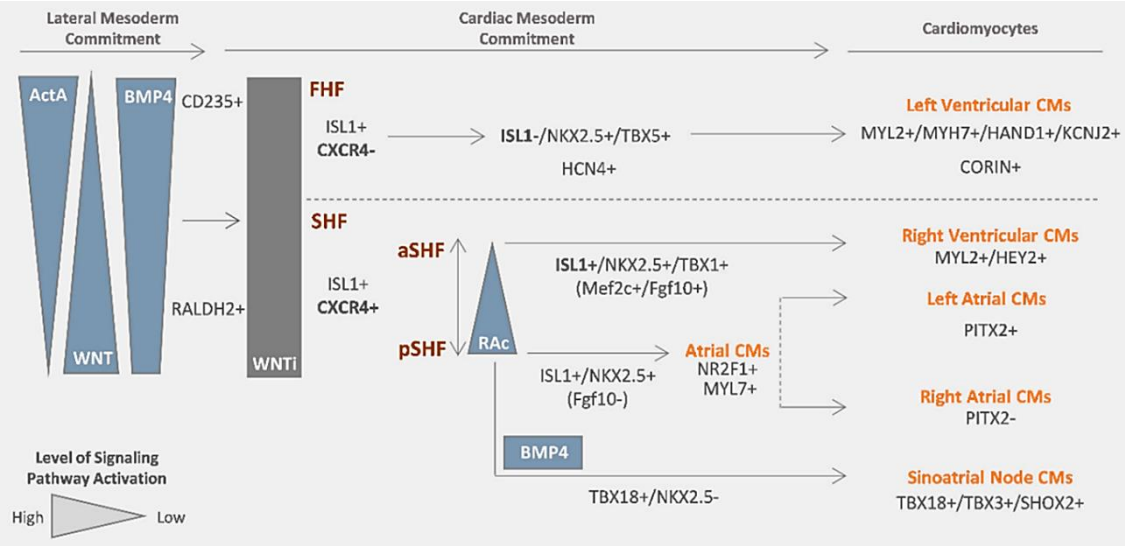

Figure 1.3: Generation of the various CM subtypes through modulation of hPSC differentiation. (ActA) Activin A signalling; (aSHF) anterior second heart field; (FHF) first heart field; (pSHF) posterior second heart field; (RAc) retinoic acid signalling; (SHF) second heart field; (WNT) Wnt signalling; (WNTi) Wnt signalling inhibition [122].

Depending on the purpose, 3D culture can nowadays be performed through two main approaches. 1) In the scaffold-free method, hPSC-derived CMs are cultured by aggregation. These 3D aggregates can be generated using either dynamic systems, such as bioreactors [150]–[152]; or static conditions, such as forced aggregation platforms [149], [153]. 2) In the scaffold-based method, hPSC-derived CMs are cultured encapsulated into ECM, natural hydrogels (such as fibrin and collagen), or synthetic hydrogels (such as polycaprolactone and polyethylene glycol) [154], [155].

Adult CMs exhibit an elongated and cylindrical shape, are multinucleated, have organized sarcomeres, and present a well-developed calcium handling system, T-tubule organization and AP [156]. Despite the progress that has been achieved in the field of CM differentiation from hPSCs, these cells still lack the structural, functional and metabolic maturation found in adult CMs [122]. Furthermore, the obtained hPSC-derived CMs are usually a mixed population of different subtypes of CMs, although they most often show a ventricular-like signature after prolonged time in culture [122], [143]. Over the years, strategies have been implemented to try to overcome these problems, namely long-term culture, electrical and mechanical stimulation, culture with biomaterials, metabolic maturation and co-culture with other cells [122]. Indeed, as a result of implementing these strategies, hPSC-derived CMs with an adult-like phenotype have been reported, characterized by an increased size and rod-shape, a higher sarcomere length, organized sarcomeres, the presence of T-tubules and AP, an increased calcium handling, a bigger number of mitochondria, and the expression of mature markers, such as MYL2 [157]–[161].

The transition from models based on homogeneous cultures of CMs to more complex multicellular cardiac microtissues has revolutionized this area of study, largely due to the elucidation of the main steps that occur during the cardiac development process in embryogenesis and how the different cell populations are specified. Microtissues, by recreating cardiac cell heterogeneity and 3D environment present in the human heart, result in a remarkable improvement in cell maturation as well as in the general function of cardiac tissue [122], [142]. Several types of cardiac microtissues have been reported in the literature, which can be mainly grouped into 1) scaffold-based engineered heart tissues (EHT), and 2) cardiac spheroids obtained through assembly of cells in a scaffold-free environment. Particularly, the model developed by Abilez et al. [162] is an example of an EHT. The authors created an engineered heart muscle (EHM) by combining hiPSC-derived CMs with human IMR-90 FBs in collagen hydrogel,

under different stretching conditions. EHMs displayed increased expression of mature CM genes, including TNNT2, calcium and potassium ion channels, β-adrenergic receptors, and T-tubule protein caveolin-3, with a decrease in beating rate and a higher degree of calcium amplitude. On the other hand, Ravenscroft et al. [163] cultured hPSC-derived CMs in multicellular spheroid microtissues, which they named CMEF microtissues, comprising human cardiac microvascular ECs and human CFs, to evaluate the contribution of non-myocyte cells on CM contractile function. Compared to hPSC-derived CM spheroids, CMEF microtissues promoted a significant increase in the expression of important genes related to cardiovascular function, nitric oxide production and microtubule and sarcomere assembly, including the calcium binding protein S100A1, considered essential in the contractile maturity of the multicellular cardiac spheroids.

Cardiac organoids, 3D self-organized structures comprising various hPSC-derived cardiac cell types that mimic the architecture and function of the *in vivo* heart, have recently been emerging as promising strategies to help better understand the mechanism of heart disease. These cardioids represent a tremendous breakthrough in biological research. Therefore, although still poorly explored, there is a great interest in developing advancements in this model system to produce 3D tissues that can better mimic the physiology of the heart [164]. Two main approaches are used to generate cardiac organoids. On the one hand, in the directed assembly method, CMs, ECs, vascular smooth muscle cells, and CFs are aggregated using hydrogels, Matrigel or ECM. Directly-assembled organoids have been utilised to study, among others, cardiac tissue maturation. In this context, Ronaldson-Bouchard et al. [165] generated a model consisting of hiPSC-derived CMs and human dermal FBs, which were encapsulated in a fibrin ECM. These mixtures were dispensed into a polycarbonate-based tissue bioreactor platform, containing tissue culture wells with flexible elastomeric pillars. After cardiac tissue formation around these pillars, the tissue was subjected to a gradually increasing electrical stimulation, with the aim of forming structures as mature as possible. The organoids displayed adult-like gene expression profiles, enhanced cardiac ultrastructure, oxidative metabolism, T-tubule formation, and calcium handling dynamics. On the other hand, in self-organized (or self-assembled) cardiac organoids, hPSCs are triggered towards cardiac lineage after spheroid formation. In a very recent study, Branco et al. [166] described the development of a self-organized heart organoid, characterized by an epicardium-like layer which surrounds a myocardium-like tissue, after CM aggregates co-culturing with self-organized human multilineage organoids. The latter recreate an early embryonic structure including both pro-epicardium/septum transversum populations and posterior foregut/hepatic primordium. This model enabled studying the impact of epicardial cells on promoting CM proliferation and structural and functional maturation.

CMs and neurons undergo co-maturation during the embryonic heart innervation. Therefore, the study of interactions between these cell types is essential, especially for modelling multi-systemic diseases such as RTT. Alongside the emergence of methods for differentiating and maintaining hPSC-derived cardiac cells, protocols for differentiating neurons from hPSCs have also been developed, with further progress being reported in the study of sympathetic neurons compared to parasympathetic ones [167]–[171]. In this context, it has been already reported in the literature hPSC-derived neuro-cardiac co-culture models (Table 1.6), which explore two main strategies distinguished by the type of cell-to-cell interaction allowed.

Through compartmentalized polydimethylsiloxane (PDMS)-based chips, it has been possible to isolate neuronal somas from CMs and restrict cell-to-cell interactions to axons extending through microtunnels between the compartments [129], [172]–[174]. In particular, chips used by Oiwa et al. [129] and Häkli et al. [174] allowed the culture of up to three different cell or tissue types on a single chip, which enables adding complexity to the model and better mimicking *in vivo* interactions.

Chips were integrated with microelectrode arrays (MEAs), in order to electrically stimulate neurons and functionally evaluate neurons and CMs [129], [172], [173]. Electrical stimulation of the neurons caused a change in the CM beat rate, which was affected by both the frequency and the pulse number applied [129], [172], [173]. These results indicated functional connections between neurons and CMs and the dependency of chronotropic effects on the activity pattern of the neurons [172], [173]. In some studies, the stimulation experiment was performed in the presence and absence of propranolol [129], [173], a β-adrenergic receptor blocker, as well as in the presence and absence of atropine [129], an acetylcholine receptor blocker, to confirm that inter-beat interval (IBI) modulation was blocked by the addition of pharmacological blockers to the culture medium. It was shown that the functional connections between neurons and CMs were dependent on the activation of these receptors.

Häkli et al. [174] used a different approach, functionally assessing CMs by chemical stimulation of neurons. The exposure of neurons to a high-K^+ solution led to significant changes in the CM beating characteristics, an increase in the beating frequency and a decrease in the contraction duration, evidencing the formation of electrophysiologically functional axon-mediated interactions between neurons and CMs.

CMs and neurons have also been co-cultured without restrictions on cell-to-cell contacts, demonstrating the formation of functional interactions between both cell types [168], [171], [175], [176].

In cardiac innervation models where CMs have been seeded on top of neurons, MEAs have also been applied. Neuronal stimulation evoked a response in the CMs. This response depended on whether the neurons used were sympathetic or parasympathetic, with an increase or decrease in cardiac beating frequency being observed, respectively [168], [171]. Winbo et al. [175] and Kowalski et al. [176] assessed CMs only by chemical stimulation of neurons, verifying that neurons were also able to modulate the beating rate of co-cultured CMs. Together, these studies enable to verify that neurons form physical and functional connections with CMs, and the β-adrenergic connections allow pharmacological (by nicotine [168], [171], [175] and propranolol [168], [171] treatment) and optogenetic (by optical control of channelrhodopsin) [168], [171] control of the neurons to influence cardiac contractile behaviours. In particular, regarding physical connections, Takayama et al. [171] identified that neurons formed varicosity-like structures along their neurites, which are essential for ANS innervation, since varicosities contain neurotransmitters released at target cells.

Furthermore, the neuro-cardiac coupling promotes the maturation of both neurons and CMs [168], [171], [176]. In this context, Kowalski et al. [176] recently performed a more detailed analysis of CM maturation aspects that were modified by co-culture, including gene expression, sarcomeres, gap junctions, and calcium handling. The neurons up-regulated genes important to the contractile apparatus, electrophysiology, and calcium machinery, as well as improved sarcomere organization, enhanced gap junction formation, and increased calcium transient amplitudes. However, sarcomere spacing, calcium relaxation time, and level of sarcoplasmic reticulum calcium did not show matured phenotypes. On the other hand, the same study reported that administration of isoproterenol alone was insufficient to induce alteration in gene expression. Thus, Kowalski et al. suggested that a different mechanism must be responsible for the expression changes observed and that β-adrenergic signalling has no, or possibly a non-detrimental, effect on CM maturation.

Table 1.6: Neuro-cardiac co-culture features and evaluated parameters. (ICG) intracardiac ganglia neurons; (NMVM) neonatal mouse ventricular myocytes; (PSNs) parasympathetic neurons; (Ref) references; (SCG) superior cervical ganglia neurons; (SNs) sympathetic neurons; (----) data unavailable.

Time	Researchers	Co-cultured cells	Co-culture time (days)	Restriction of cell-to-cell contacts	Assessment of neuron-CM interaction	Ref
2011	Takeuchi et al.	• Rat SCG neurons as SNs • Rat ventricular CMs	----	Yes	Evaluation of the effect of electrical stimulation applied to neurons on CM beating rate.	[172]
2016	Oh et al.	• hPSC-SNs • NMVM • hiPSC-CMs	----	No	Evaluation of the effect of electrical stimulation applied to neurons on CM beating rate. Evaluation of the co-culture effect on neuron and CM maturation.	[168]
2016	Oiwa et al.	• Rat SCG neurons as SNs • Rat ICG neurons as PSNs • Rat atrial CMs	20–25	Yes	Evaluation of the effect of electrical stimulation applied to neurons on CM beating rate.	[129]
2017	Sakai et al.	• Rat primary SNs • hiPSC-CMs	12–16	Yes	Evaluation of the effect of electrical stimulation applied to neurons on CM beating rate.	[173]
2020	Winbo et al.	• hiPSC-SNs • hiPSC-CMs	15	No	Evaluation of the effect of chemical stimulation applied to neurons on CM beating rate.	[175]
2020	Takayama et al.	• hiPSC-SNs • hiPSC-PSNs • hiPSC-CMs	21	No	Evaluation of the effect of electrical stimulation applied to neurons on CM beating rate. Evaluation of the co-culture effect on neuron and CM maturation.	[171]
2022	Kowalski et al.	• Embryonic mouse SNs • hiPSC-CMs	30	No	Evaluation of the effect of chemical stimulation applied to neurons on CM beating rate. Evaluation of the co-culture effect on neuron and CM maturation.	[176]
2022	Häkli et al.	• hiPSC-cortical neurons • hiPSC-CMs	15 and 30	Yes	Evaluation of the effect of chemical stimulation applied to neurons in the CM beating, using contraction duration, time to peak, relaxation time and peak-to-peak time parameters.	[174]

Chapter 2

Motivation and Aim of Studies

The self-renewal capacity of hiPSCs and their potential to differentiate into any cell type of the human body has aroused general enthusiasm for the development of new models of human disease, improved platforms for drug discovery, and wider employment of autologous cell-based therapies. In this context, disease modelling is extremely relevant, as it enables the study of a series of human diseases *in vitro*, allowing to identify pathological mechanisms, as a key to develop new therapeutic strategies for their prevention and treatment, while overcoming many of the challenges of obtaining tissue from patient donors. Additionally, by using patient-specific cells, these technologies enable the emergence of a more personalized medicine, a new paradigm designated as precision medicine.

Currently, several models have been used for studying RTT, which mainly focus on analysing alterations in brain development and function. However, models that mimic this disease in other affected organs besides the brain, such as the heart, are lacking. Additionally, the majority of the information regarding RTT is based on animal models, which do not faithfully mimic the phenotypic aspects of human RTT. To overcome these limitations, this work aimed to develop novel *in vitro* 3D cardiac models of RTT and further identification of RTT-derived alterations that may contribute to provide new targets for the development of RTT therapeutic strategies directed towards the cardiac phenotype. Therefore, this project was divided into two main parts. The first one aimed to study RTT-derived alterations to the process of cardiac differentiation from hiPSCs, after optimizing the process of hiPSC differentiation into CMs as 3D aggregates using either MT or WT cell lines. The second part focused on studying the obtained RTT versus healthy aggregates, both in terms of their structural architecture and cellular composition, as well as concerning the CM sarcomere microstructure.

Chapter 3

Materials and Methods

3.1. Expansion of Human Induced Pluripotent Stem Cells

3.1.1. Cell Lines

In this work, experiments were performed using four cell lines, two hiPSC lines derived from patients with a RTT-associated mutation and two healthy-control hiPSC lines. One of these healthy control hiPSC lines was the isogenic pair of one of the RTT cell lines, whereas the other was genetically uncorrelated. The RTT cell lines used were 1) EMC24i/R2 (C6) (46, XX cell line of a RTT patient with a mutation at MeCP2 (R255X), a nonsense mutation on C to T transition at hypermutable CpG sites within the gene, reprogrammed from skin fibroblasts using engineered colour-coded lentiviral vectors at iPSC Facility of Erasmus Medical Center), henceforth referred as R2C6; and 2) RS2042-0035E-MU (46, XX cell line of a RTT patient with a mutation at MeCP2 (R255X), reprogrammed from erythroblasts using Sendai virus at Harvard Stem Cell Institute), henceforth referred as R255X M. The healthy-control hiPSC lines were the 1) RS2042-0047B-WT line (RS2042-0035E-MU isogenic cell line), henceforth referred as R255X WT; and the 2) iPS-DF6-9-9T.B line (46, XY cell line, reprogrammed from foreskin fibroblasts, collected from healthy donors, using defined factors at University of Wisconsin, and provided by WiCell Bank), henceforth referred as DF6.

3.1.2. Adhesion Substrate

hiPSC lines were maintained as a monolayer on Matrigel® (Corning®, #354277) coated culture plates. Each Matrigel® aliquot stored at -20ºC was thawed and diluted 1:100 (v/v) in cold Dulbecco's Modified Eagle Medium: Nutrient Mixture F-12 (DMEM/F12) (Gibco™/Thermo Fisher Scientific, #32500-035) as needed.

3.1.3. Culture Medium

For hiPSC culture, mTeSR™1 medium (STEMCELL Technologies™, #85850), composed of basal medium and 5x supplement, was used. mTeSR™1 5x supplement was thawed and mixed with basal medium. The mixture was aliquoted and stored at -20°C. After thawing, individual aliquots were supplemented with 1:200 (v/v) penicillin/streptomycin (PenStrep) (Gibco™/Thermo Fisher Scientific, #15140122). Before each use, mTeSR™1 was pre-warmed at room temperature (RT).

3.1.4. Cell Thawing and Preservation

Cells cryopreserved in liquid nitrogen at -196°C were thawed at 37°C for each experiment. The cell content of a cryovial was then resuspended in culture medium [or culture medium supplemented with 1:1000 (v/v) Rho kinase inhibitor (ROCKi, Y-27632) (STEMCELL Technologies™, #72304), depending on the cell line being used] in a centrifugation tube and centrifuged at 210 × g for 3 min. Cell pellet was resuspended in culture medium (or culture medium supplemented with ROCKi) before being seeded onto a Matrigel® coated culture plate with a final volume of 1.5 mL. hiPSCs were maintained in a CO_2 incubator at 37°C, 5% CO_2, and 20% O_2, with the culture medium being changed daily.

3.1.5. Cell Passaging

Cells were passaged at a 1:3 split ratio onto new Matrigel®-coated 6-well tissue culture plates (Corning®, #10578911) when they reached 70-80% confluence. Two protocols were followed, depending on the cell line being used. 1) After removing the culture medium, cells were washed and then incubated for 5 min with EDTA solution (Invitrogen™/Thermo Fisher Scientific, #15575-038) diluted in phosphate-buffered saline (PBS) (Sigma-Aldrich®/Merck, #D8662) at a concentration of 0.5 mM. After removing the EDTA, cells were flushed with culture medium and collected to a centrifuge tube followed by seeding on the new Matrigel® coated culture plates. 2) After removing the culture medium, cells were washed with PBS and then incubated for 7 min with Gentle Cell Dissociation Reagent (GCDR) (STEMCELL Technologies™, #100-0485). After removing the GCDR, colonies were gently detached with culture medium by scraping with a serological glass pipette and collected to a centrifuge tube followed by seeding in the new Matrigel® coated culture plates.

3.1.6. Cell Cryopreservation

In order to store hiPSCs, the culture medium was first removed, then cells were washed and incubated for 5 min with EDTA. After removing the EDTA, cells were flushed with culture medium, collected to a centrifuge tube and centrifuged at 210 × g for 3 min. Cell pellet was resuspended in KnockOut™ serum replacement (KO-SR) (Gibco™/Thermo Fisher Scientific, #10828028) with 1:10 (v/v) of dimethylsulfoxide (DMSO) (Sigma-Aldrich®/Merck, #276855) for a final volume of 250 µL/vial. The cell suspension was placed in a cryovial and frozen for 24 h at -80°C before being kept in liquid nitrogen at -196°C.

3.2. 3D Differentiation of Human Induced Pluripotent Stem Cells into Cardiomyocytes

3.2.1. Cell Seeding and Pre-differentiation Culture

Cell seeding was performed when hiPSCs reached 70% confluence. After removing the culture medium, cells were washed with PBS and then incubated with Accutase® solution (Sigma-Aldrich®/Merck, #A6964) at 37°C for 7 min for single cell dissociation. Cells were flushed with the existing Accutase® solution in each well and collected to a centrifuge tube with culture medium, for inactivation of enzymatic digestion, and centrifuged at 210 × g for 3 min. Cell pellet was resuspended in culture medium supplemented with 1:1000 (v/v) ROCKi, followed by seeding onto a

AggreWell™800 24-well plate (STEMCELL Technologies™, #34815) with a cell density of 1) 3000 cells/microwell (9×10^5 cells/well); 2) 3800 cells/microwell (1.14×10^6 cells/well); 3) 4000 cells/microwell (1.2×10^6 cells/well); or 4) 5000 cells/microwell (1.5×10^6 cells/well); depending on the tested condition, for a final volume of 1.5 mL/well. Cell suspension sample was diluted 1:6 in Trypan Blue solution (Gibco™/Thermo Fisher Scientific, #15250-061). The AggreWell™800 24-well plate was then centrifuged at 2700 × *g* for 5 min, before seeding, and 300 × *g* for 3 min, after seeding. Gravitational forces promoted cell settling and self-aggregation to form 3D aggregates. Cells were incubated in a CO_2 incubator at 37°C, 5% CO_2 and 20% O_2, and the exhausted culture medium was replaced by fresh mTeSR™1 after 24 h and 48 h (Figure 3.1).

3.2.2. Cardiac Differentiation

For hiPSC differentiation into CMs as 3D aggregates (Figure 3.1), it was adapted a protocol developed by Branco et al. [142]. During the differentiation process, two basal media were used. Cells were cultured in the first basal medium, consisting of Roswell Park Memorial Institute (RPMI) 1640 medium (Gibco™/Thermo Fisher Scientific, #11875-093) supplemented with 1:50 (v/v) B-27™ minus insulin (Gibco™/Thermo Fisher Scientific, #A1895601), from day (D) 0 to D6. The second basal medium, consisting of RPMI supplemented with 1:50 (v/v) B-27™ (Gibco™/Thermo Fisher Scientific, #17504001), was used from D7 until the end of differentiation (D15-19). Basal medium was always supplemented with 1:200 (v/v) PenStrep. At D0 of differentiation, after mTeSR™1 culture medium removal, cells were cultured in the first basal medium supplemented with the GSK3 inhibitor CHIR99021 (CHIR) (Stemgent™, #04-0004) at a final concentration of 7 µM, 9 µM or 11 µM, depending on the tested condition. At D1, cells were cultured in the first basal medium. At D3, medium was changed to the first basal medium supplemented with IWP-4 (Stemgent™, #04-0036) at a final concentration of 5 µM. At D5, cells were cultured in the first basal medium. At D7, medium was changed to the second basal medium and the aggregates were flushed from the AggreWell™800 24-well plate and transferred to a 6-Well Ultra-Low Attachment plate (Corning®, #3471). Thereafter, medium was changed every 2-3 days until the cells were harvested.

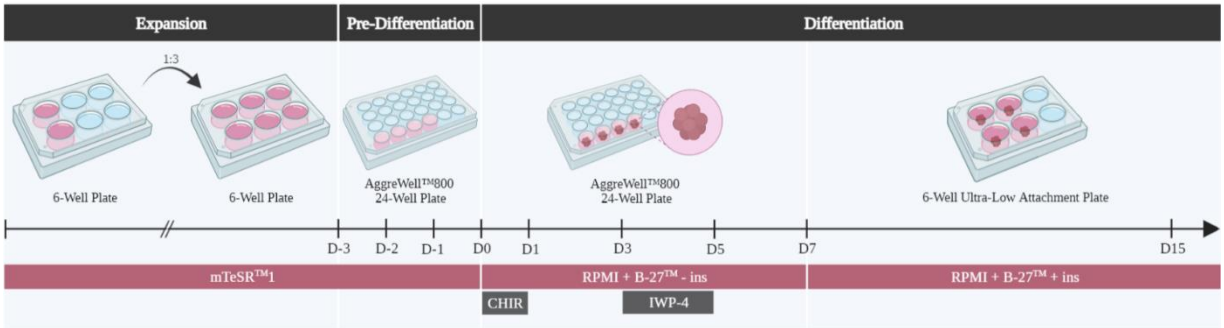

Figure 3.1: Schematic illustration of the methodology used for hiPSC differentiation into CMs as 3D aggregates. (ins) insulin.

3.2.3. Aggregate Size Analysis

The CM aggregate size was monitored throughout the entire differentiation stage, using an optical microscope, and representative images of D0, D11-13 and D15-19 aggregates were taken using Leica DMI 3000B microscope with a Nikon DXM 1200F digital camera. The size of the D0 and D11-13

aggregates was measured using ImageJ software, specifically through the determination of the Feret diameter, which represents the longest distance between any two points along the selection boundary, being applied to projections of a 3D body onto a 2D plane (Figure 3.2).

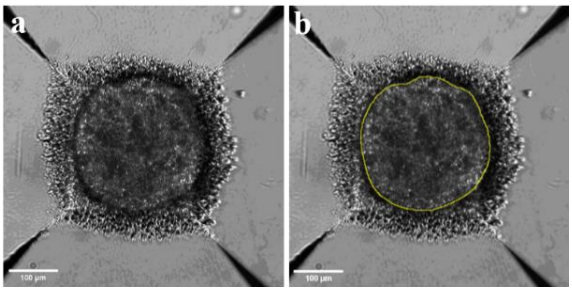

Figure 3.2: Aggregate size measurement during the process of 3D cardiac differentiation. **(a)** Representative bright-field (BF) image of an aggregate at D0 of differentiation. **(b)** Aggregate diameter measurement (in yellow) using ImageJ software to Feret diameter determination. Scale bars represent 100 µm.

3.3. Flow Cytometry Analysis

At the end of culture, hiPSC-derived CM aggregates were washed with PBS and then incubated with 0.25% (v/v) trypsin-EDTA (Gibco™/Thermo Fisher Scientific, #R001100) in PBS at 37ºC for 7 min. Then, RPMI supplemented with 10% (v/v) fetal bovine serum (FBS) (Gibco™/Thermo Fisher Scientific, #10270-106) was added for enzymatic digestion inactivation and cells were homogenized before being centrifuged at 210 × *g* for 3 min. Cell pellet was washed with PBS and centrifuged again at 210 × *g* for 3 min. After PSB removal, cell pellet was fixed by resuspension in 2% (v/v) paraformaldehyde (PFA) (Sigma-Aldrich®/Merck, #158127) in PBS and kept at 4°C until flow cytometry was performed.

The antibodies used for flow cytometry analysis were Octamer Binding Transcription Factor 4 (OCT4), Stage-Specific Embryonic Antigen-4 (SSEA4) and T Cell Receptor Alpha Locus (TRA-1-60) markers, for pluripotency assessment, and cTnT, to quantify the percentage of CMs at the end of the differentiation process. In the case of the primary antibodies OCT4 and cTnT it was performed an intracellular staining protocol, and in the case of SSEA4 and TRA-1-60 a cell surface staining protocol was applied.

3.3.1. Intracellular Markers

Fixed cells were centrifuged at 200 × *g* for 5 min. Cell pellet was resuspended and incubated with 90% (v/v) cold methanol in Milli-Q® water at 4ºC for 15 min. Cells were then washed three times with flow cytometry buffer 1 (FB1) (0.5% (v/v) bovine serum albumin (BSA) solution (Sigma-Aldrich®/Merck, #A8327) in PBS), and centrifuged at 210 × *g* for 5 min, each time. Cell pellet was resuspended in flow cytometry buffer 2 (FB2) (0.1% (v/v) Triton X-100 (Sigma-Aldrich®/Merck, #T9284) in FB1), with the appropriate dilution of primary antibody, according to Table 3.1, and incubated at RT for 1 h. After incubation, cells were washed twice with FB2 and cell pellet was resuspended in FB2 containing a 1:1000 (v/v) dilution of secondary antibody, according to Table 3.2. The mixture was incubated for 30 min at RT in the dark. Cells were washed twice with FB2 and centrifuged at 210 × *g* for 5 min, each time. Cell pellet was resuspended in 300 µL of PBS and cell suspension was transferred to Falcon round-bottom tubes. Flow cytometry was performed using a

FACSCalibur™ flow cytometer (Becton Dickinson) and data analysis using FlowJo software. For each sample, a minimum of 1×10^4 events were analysed.

3.3.2. Surface Markers

Fixed cells were centrifuged at 210 × *g* for 5 min. Cell pellet was resuspended in 1 mL of PBS. Cells were then washed three times with PBS and centrifuged at 210 × *g* for 5 min, each time. Cell pellet was resuspended in 100 µL of 2% BSA solution in PBS with the appropriate dilution of the antibody, according to Table 3.1, and incubated at RT for 30 min in the dark. Cells were washed twice with PBS and centrifuged at 210 × *g* for 5 min, each time. Cell pellet was resuspended in 300 µL of PBS and cell suspension was transferred to Falcon round-bottom tubes. Flow cytometry was performed using a FACSCalibur™ flow cytometer (Becton Dickinson) and data analysis using FlowJo software. For each sample, a minimum of 1×10^4 events were analysed.

3.4. Immunostaining Analysis

Immunostaining analysis was performed in aggregate slices of D12-D15 CM aggregates and in D15-D19 replated CMs. Immunofluorescence staining images were acquired using Zeiss LSM 710 Confocal Laser Point-Scanning Microscope and images were processed in ZEN 2.3 blue edition software (Zeiss).

3.4.1. Sample Collection

3.4.1.1. Aggregate Slices

At the end of culture, aggregates were washed with PBS and then incubated for 30 min in 4% (v/v) PFA in PBS at RT. After PFA removal, the fixed aggregates were stored in PBS at 4ºC. Before slicing the fixed aggregates, they were incubated in 15% (m/v) sucrose (Sigma-Aldrich®/Merck, #S7903) in PBS, at 4ºC overnight. Then, aggregates were embedded in 7.5% (w/v) gelatin (Sigma-Aldrich®/Merck, #G6144) supplemented with 15% (wt/vol) sucrose and isopentane (Carlo Erba Reagents, #528492) was used for freezing at -80°C. Aggregate sections with approximately 10-12 µm thickness were cut on a cryostatmicrotome (Leica CM3050S, Leica Microsystems) and collected on Superfrost™ Microscope Slides (Thermo Scientific). At the time of analysis, aggregate slices were degelatinized in PBS at 37°C for 30 min.

3.4.1.2. Replated Aggregates

At the end of culture, aggregates were washed with PBS and then incubated with 0.25% (v/v) trypsin-EDTA in PBS at 37ºC for 7 min. RPMI supplemented with 10% (v/v) FBS was added for enzymatic digestion inactivation and cells were homogenized before being centrifuged at 210 × *g* for 3 min. Cell pellet was resuspended in RPMI supplemented with B-27™, ROCKi and 10% (v/v) FBS and seeded in a 24-well plate coated with Matrigel® and coverslips. Two days after replating, cells were washed with PBS and fixed with 4% (v/v) PFA in PBS for 20 min at RT. After PFA removal, coverslips were left in PBS and kept at 4°C until analysis.

3.4.2. Immunostaining

At the time of analysis, the CM aggregate slices and replated CMs were incubated in 0.1 M glycine (Sigma-Aldrich®/Merck, #G8898) for 10 min at RT to remove PFA residues, permeabilized with 0.1% (v/v) Triton X-100 in PBS, at RT for 10 min and blocked with 10% (v/v) FBS in TBST (20 mM Tris-HCl pH 8.0, 150 mM NaCl and 0.05% (v/v) Tween-20 (Sigma-Aldrich®/Merck, #P1379) in PBS, at RT for 30 min. Cells were incubated with primary antibodies (Table 3.1) diluted in blocking solution at 4°C overnight. After three washing steps with TBST, cells were incubated with secondary antibodies (Table 3.2) for 30 min at RT in the dark. Nuclear counterstaining was performed using 0.15% (v/v) 4',6-diamidino-2-phenylindole (DAPI) dye (Sigma-Aldrich®/Merck, #D9542) in PBS, at RT for 10 min. After brief drying, the CM aggregate slices and replated CMs were mounted in Mowiol® (Sigma-Aldrich®/ Merck, #81381).

Table 3.1: Primary antibodies used for flow cytometry and immunostaining analysis. (Cat. No.) catalogue number; (FC) flow cytometry; (I) intracellular; (IS) immunostaining; (S) surface.

Primary antibody		Staining		Supplier, #Cat. No.	Application	Dilution
α-actinin	Mouse IgG	CMs (sarcomeres)	I	Sigma-Aldrich®/Merck, #A7811	IS	1:200
CD31	Mouse IgG	ECs	S	Dako/Agilent Technologies, #M0823	IS	1:50
cTnT	Mouse IgG	CMs (fibers)	I	Invitrogen™/ Thermo Fisher Scientific, #MA5-12960	IS FC	1:200
ISL1	Rabbit IgG	Cardiac progenitors	I	Abcam, #ab178400	IS	1:200
Ki-67	Rabbit IgG	Cell proliferation	I	Abcam, #ab833	IS	1:50
NKX2.5	Rabbit IgG	CMs (nucleus)	I	Abcam, #ab97355	IS	1:200
OCT4	Mouse IgG	Pluripotency	I	Millipor, #MAB4419	FC	1:200
SSEA4	Human IgG	Pluripotency	S	Miltenyi Biotec, #130-098-369	FC	1:50
TRA-1-60	Human IgG	Pluripotency	S	Miltenyi Biotec, #130-100-347	FC	1:50

Table 3.2: Secondary antibodies used for flow cytometry and immunostaining analysis. (Cat. No.) catalogue number; (FC) flow cytometry; (IS) immunostaining.

Secondary antibody		Supplier, #Cat. No.	Application	Dilution
Alexa Fluor™ 546	Anti-mouse IgG	Invitrogen™/Thermo Fisher Scientific, #A11003	IS	1:500
Alexa Fluor™ 488	Anti-rabbit IgG	Invitrogen™/Thermo Fisher Scientific, #A11008	IS	1:500
Alexa Fluor™ 488	Anti-mouse IgG	Invitrogen™/Thermo Fisher Scientific, #A11001	FC	1:1000

3.5. Aggregate Cavity Analysis

The cavities of each hiPSC-derived CM aggregate were monitored using an optical microscope. Representative images of D11-13 and D15-19 aggregates were taken using Leica DMI 3000B microscope with a Nikon DXM 1200F digital camera. The number of cavities and the size of the aggregates and their cavities were measured using immunofluorescence staining images and ImageJ software (Figure 3.3 a, b, c, d). To do so, the aggregates (Figure 3.3 c) and their cavities (Figure 3.3 d) were delimited, taking into consideration cTnT and DAPI staining. All the internal regions of the aggregates characterized by the absence of DAPI staining were considered cavities. The area of each aggregate and the respective cavities was the parameter used to quantify their size. Through the obtained values, the percentage of aggregate area occupied by cavities (Equation 3.1) and the proportion of cavities by area range (Equation 3.2; Table 3.3) were determined.

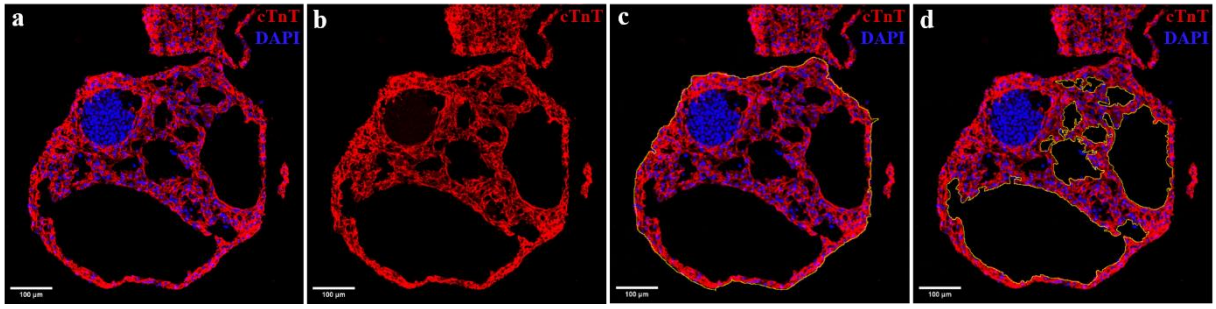

Figure 3.3: Measurement of CM aggregate cavities. Representative immunofluorescence staining images of CM aggregate cryosections at D13 of differentiation **(a-b)**. Cells were stained for cTnT in red (CM fibers) and nuclei in blue were stained with DAPI. **(c)** Aggregates and **(d)** their cavities were delimited as shown in yellow. Scale bars represent 100 µm.

$$\text{Percentage of aggregate area occupied by cavities} = \frac{\sum_{i=1}^{t} \text{aggregate cavity}_i \text{ area}}{\text{aggregate area}} \times 100$$

Equation 3.1

where t is the total number of cavities per aggregate.

$$\text{Proportion of cavities by area range} = \frac{\text{number of cavities in the area range}_r}{\text{total number of cavities}} \times 100$$

Equation 3.2

where r is the total of area ranges mentioned in Table 3.3.

Table 3.3: Area ranges considered for the cavity size study.

Area Range	Inferior Limit (µm^2)	Superior Limit (µm^2)
1	0	1 000
2	1 001	10 000
3	10 001	100 000
4	100 001	1 000 000

3.6. Cardiomyocyte Sarcomere Analysis

The microstructure of the CM sarcomeres was analysed using immunofluorescence staining images and Sarcomere Organization and Texture Analysis Tool (SotaTool) software for automated quantification, based on the protocol developed by Stein et al. [177]. The exposure and contrast of the immunofluorescence staining images used in the analysis were adjusted in ImageJ software, in order to optimize the regions of interest (the sarcomeres) (Figure 3.4 a, b). The image resolution and segmentation were the only parameters manipulated in the SotaTool interface. The program generates a folder with the segments resulting from the original image segmentation, as well as a second folder with output graphs and a .csv file with the values of the analysed parameters.

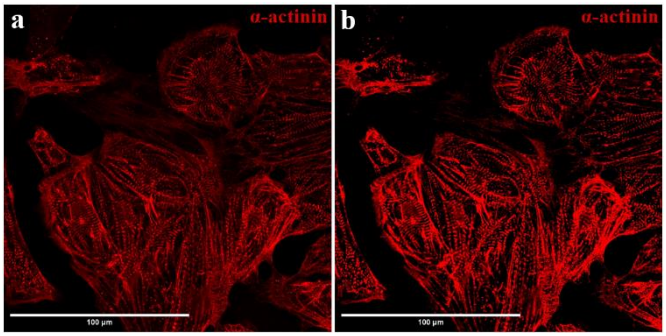

Figure 3.4: CM sarcomere analysis. **(a)** Representative immunofluorescence staining image of replated CM aggregates at D19 of differentiation. Cells were stained for α-actinin in red (CM sarcomeres). **(b)** Resulting image from manipulation of the representative immunofluorescence staining image. Scale bars represent 100 µm.

3.7. Cardiomyocyte Proliferation Analysis

CMs can be identified through immunofluorescence analysis of cTnT and proliferative CMs may be identified by co-staining with Ki-67. In this work, the percentage of proliferative CMs was determined by Equation 3.3.

$$\text{Percentage of proliferative CMs} = \frac{\text{number of proliferative CMs}}{\text{number of CMs}} \times 100$$

Equation 3.3

3.8. Statistical Analysis

Statistical analysis was performed with GraphPad Prism 8 (GraphPad Software). Statistical significance was evaluated with a two-tailed, unpaired Student's t test ($p < 0.05$). The data are presented as mean ± standard deviation (SD) or mean ± standard error of mean (SEM), depending on the independent experiments considered. Statistical significance was assigned as not significant (ns), $p \geq 0.05$; (*) $p < 0.05$; (**) $p < 0.01$; (***) $p < 0.001$; (****) $p < 0.0001$.

Chapter 4

Results and Discussion

4.1. Rett Syndrome-derived Alterations to the Process of Cardiac Differentiation from Human Induced Pluripotent Stem Cells

A protocol previously established by Branco et al. [142] was used to differentiate hiPSCs into CMs as 3D aggregates, which is based on the temporal modulation of Wnt signalling pathway by small molecules in a very specific and controlled manner. Briefly, it starts with Wnt signalling activation for mesendoderm induction, followed by a step of Wnt pathway inhibition to cardiac lineage specification. Two culture parameters have been proven to be relevant for cardiac differentiation success, namely 1) the aggregate size at D0 of differentiation and 2) the CHIR concentration.

Cardiac differentiation optimization was performed using both 1) MT cell lines, including R2C6 and R255X M, and 2) WT cell lines, namely DF6 and R255X WT, which were used as controls throughout all the experiments. The individual optimization for each cell line is essential since variability between cell lines and heterogeneity within clones, as a consequence of genetic and epigenetic variations, is well documented in the literature for this specific differentiation protocol [178].

4.1.1. Pre-differentiation Period

The first goal of this MSc project was to study the impact of using different cell seeding densities at D-3 of differentiation to reach an aggregate size at D0 in the range previously identified as the optimal one (± 300 µm) for the various cell lines. To do so, single hiPSCs were forced to aggregate in Aggrewell plates, allowing the aggregates to form and grow for 3 days in mTeSR™1 before starting the differentiation process. After cell settling in the microwells by gravitation, they self-organized into 3D aggregates and their size was monitored.

A cell seeding density of 3800 cells/aggregate (7.6×10^5 cells/mL) has been previously defined as the optimal condition for hiPSC differentiation into CMs for the DF6 cell line. Thus, in the case of the R2C6 cell line, 3000 and 4000 cells/aggregate (6×10^5 and 8×10^5 cells/mL, respectively) were tested, as the optimal cell seeding density for the DF6 cell line is included in this range. Since in the case of R255X M and respective WT cell line, it was observed that the cell size was apparently smaller than both DF6 and R2C6 hiPSCs, it was tested a greater number of cells per aggregate to ensure reaching the optimal size at D0. Thus, cell seeding densities of 4000 and 5000 cells/aggregate (10^6 cells/mL) were tested for both R255X M and WT hiPSCs.

Regardless of the cell line and cell seeding density used, all aggregates presented a similar aspect (Figure 4.1 a, b, c, d). Despite some cell death, the vast majority of cells aggregated at the bottom of the Aggrewell plate, clustering together in a spherical shape.

One important parameter that also determines the success of hiPSC differentiation is the pluripotency stage of the initial cell population. Taking that into consideration, the pluripotency state of one of the RTT-derived hiPSC lines used, namely the R2C6 cell line, was assessed through flow cytometry (Figure 4.1 e). The results revealed that 96.3% were OCT4^{+}, and 100% of the cells were SSEA4^{+}/TRA-1-60^{+}, which provides a good indication that the analysed cells were pluripotent.

At D0, the R2C6 aggregates presented an average size of 288.4 ± 3.5 µm and 293.2 ± 4.1 µm for a cell seeding density of 3000 and 4000 cells/aggregate, respectively (Figure 4.1 f; Supplementary Figure 1). In the case of R255X M aggregates, the average diameter was 284.8 ± 2.5 µm for the 4000 cells/aggregate condition and 287.3 ± 1.7 µm for the 5000 cells/aggregate condition (Figure 4.1 g). The DF6 aggregates presented an average size of 297.6 ± 1.7 µm (Figure 4.1 h), while the R255X WT aggregates had a diameter of 283.4 ± 2.4 µm and 278.0 ± 1.5 µm for cell seeding densities of 4000 and 5000 cells/aggregate, respectively (Figure 4.1 i). With the exception of the DF6 cell line, for which only one cell seeding density was tested, there were no significant differences between the average size of aggregates obtained from the two tested cell seeding densities.

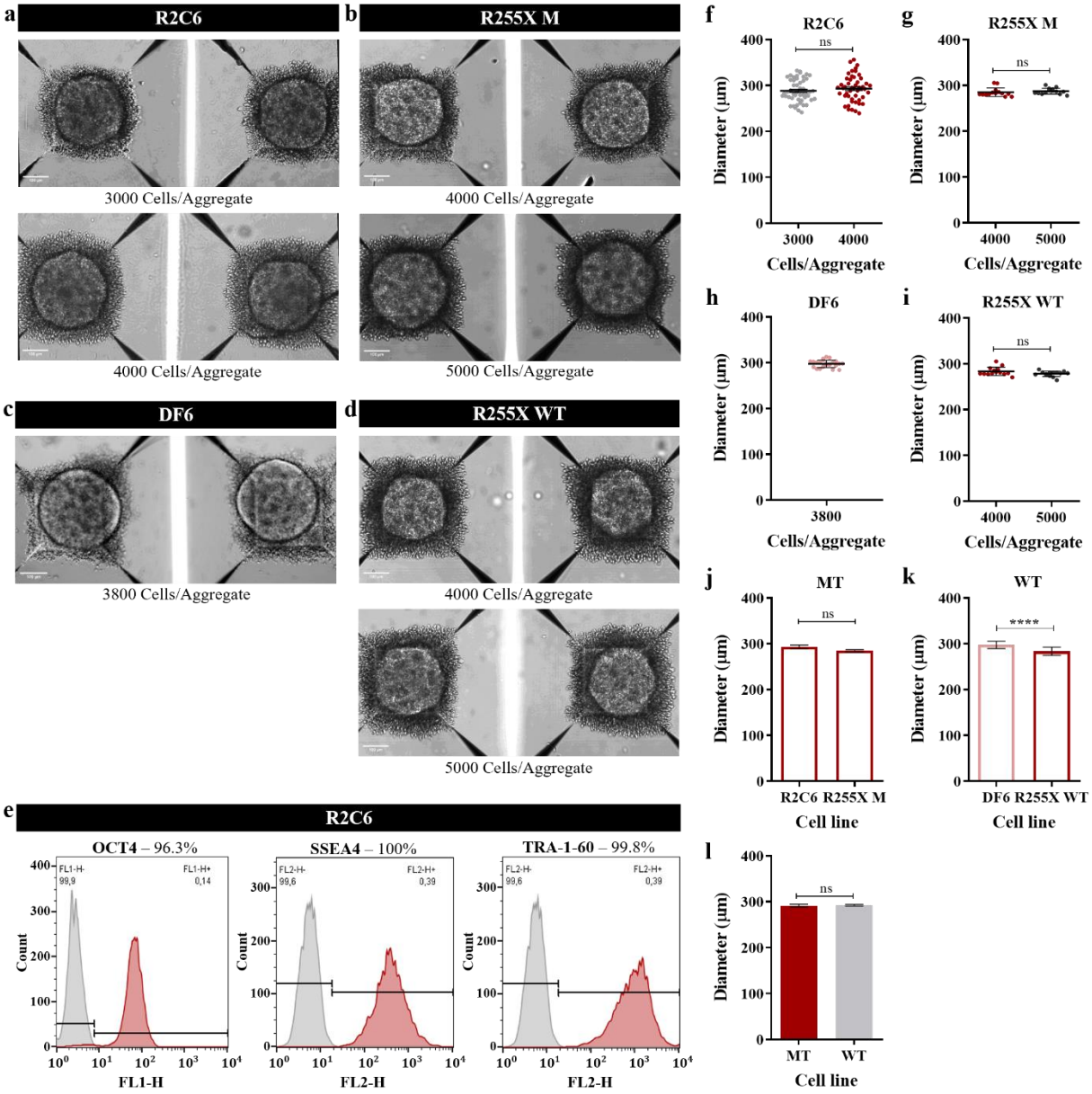

Figure 4.1: Characterization of the pre-differentiation period of hiPSC differentiation into CMs as 3D aggregates. Bright-field (BF) images at D0 of R2C6 aggregates for a cell seeding density of 3000 and 4000 cells/aggregate **(a)**; R255X M aggregates for a cell seeding density of 4000 and 5000 cells/aggregate **(b)**; DF6 aggregates for a cell seeding density of 3800 cells/aggregate **(c)**; and R255X WT aggregates for a cell seeding density of 4000 and 5000 cells/aggregate **(d)**. **(e)** Assessment of the pluripotency state of R2C6 cell line by flow cytometry analysis for OCT4, SSEA4 and TRA-1-60. n=1. **(f)** R2C6 aggregate size for a cell seeding density of 3000 and 4000 cells/aggregate at D0 by Feret diameter measurement. Mean ± SEM; n=3 experiments, measuring N=50 aggregates for the 3000 cells/aggregate condition and N=49 for the 4000 cells/aggregate condition. **(g)** R255X M aggregate size for a cell seeding density of 4000 and 5000 cells/aggregate at D0 by Feret diameter measurement. Mean ± SD; n=1 experiment, measuring N=14 aggregates for each cell seeding density. **(h)** DF6 aggregate size for a cell seeding density of 3800 cells/aggregate at D0 by Feret diameter measurement. Mean ± SD; n=1 experiment, measuring N=23 aggregates. **(i)** R255X WT aggregate size for a cell seeding density of 4000 and 5000 cells/aggregate at D0 by Feret diameter measurement. Mean ± SD; n=1 experiment, measuring N=14 aggregates for each cell seeding density. **(j)** MT aggregate size comparison between the R2C6 cell line with a 4000 cells/aggregate cell seeding density and the R255X M cell line with a 4000 cells/aggregate cell seeding density at D0. Mean ± SEM. **(k)** WT aggregate size comparison between the DF6 cell line with a 3800 cells/aggregate cell seeding density and the R255X WT cell line with a 4000 cells/aggregate cell seeding density at D0. Mean ± SD. **(l)** Comparison between MT and WT aggregate size at D0. Mean ± SEM; measuring N=63 MT aggregates and N=37 WT aggregates. MT aggregates correspond to the R2C6 cell line with a 4000 cells/aggregate cell seeding density and the R255X M cell line with a 4000 cells/aggregate cell seeding density; WT aggregates correspond to the DF6 cell line with a 3800 cells/aggregate cell seeding density and the R255X WT cell line with a 4000 cells/aggregate cell seeding density. (j), (k) and (l) data correspond to the cell seeding density of the optimal condition for each cell line, determined based on the analysis of the results obtained during the pre-differentiation and differentiation periods (discussed below). Statistical analysis was performed using T-tests, with (****) $p < 0.0001$, (ns) not significant. Scale bars represent 100 µm.

Overall, no significant difference was observed in aggregate size at D0 between MT and WT lines (291.3 ± 3.2 µm and 292.2 ± 1.8 µm, respectively), being the value in both cases in the range of the optimal one (± 300 µm) (Figure 4.1 j, k, l).

The two density conditions tested for each cell line were further evaluated concerning their differentiation process, as the range of tested densities was not large enough to contemplate differences between aggregates at this point.

4.1.2. Cardiac Differentiation Period

As described in the previous section (Materials and Methods), at D0 of differentiation, cells were cultured in the first basal medium supplemented with CHIR at a final concentration of 7 µM, 9 µM or 11 µM, depending on the tested condition (Figure 4.2 a, b, c, d). At D3, the small molecule IWP-4 for Wnt signalling blockage was used at a concentration of 5 µM for all cell lines. The impact on CM differentiation efficiency was analysed at D11-D15 of differentiation (Figure 4.2 e, f, g, h, i, j; Supplementary Table 1; Supplementary Figure 2).

Aggregate contraction, which is the first indicator of a successful differentiation into CMs, was analysed throughout the process of differentiation. Spontaneous contractions were first observed around D9. Then, in the course of time, the percentage of beating aggregates increased, and the spontaneous contractions became increasingly vigorous, not ceasing until the aggregates were collected for further analysis at D13-19.

Through bright-field (BF) images taken on the final days of cardiac differentiation, it was found that R2C6 aggregates (Figure 4.2 a) supplemented with 9 µM CHIR, and R255X M aggregates (Figure 4.2 b) supplemented with 9 and 11 µM CHIR were bigger and more uniform (more similar in terms of shape within each condition) compared to aggregates supplemented with 11 µM CHIR and 7 µM CHIR, respectively. Additionally, it was evident that R2C6 aggregates supplemented with 9 µM CHIR and R255X M aggregates supplemented with 9 and 11 µM CHIR were less compact, with most of their volume being composed by cavities. Although the impact of the different tested CHIR concentrations was visible, it was not possible to conclude, in a qualitative way, whether there were differences between aggregates derived from distinct cell seeding densities from both RTT cell lines.

Regarding the R255X WT aggregates (Figure 4.2 d), it was found that the aggregate size in the 9 and 11 µM CHIR conditions, both for the 4000 cells/aggregate and for 5000 cells/aggregate, appeared to be bigger than the ones observed for the 7 µM CHIR condition. Under all conditions, a high degree of compaction, meaning denser aggregates with a smaller proportion of their volume being composed by cavities, was observed compared with RTT cell lines. DF6 aggregates (Figure 4.2 c), only tested for the optimal condition, appeared to look similar to R255X WT aggregates supplemented with 9 µM CHIR and 11 µM CHIR.

During the differentiation period, the aggregates increased in size, reaching an average of 670.5 ± 30.7 µm for the MT aggregates and 513.5 ± 11.6 µm for the WT aggregates at D11-13 (Figure 4.2 k; Supplementary Figure 3). This increase in size could be detected mainly after transferring the aggregates from the Aggrewell plates to low adhesion cell culture plates, where they remained from D7 to D15 of differentiation under static conditions. Comparing the RTT aggregates with the healthy ones, it was found a lower compaction degree and, consequently, more cavities, in the RTT aggregates, regardless of the cell seeding density used. This distinct morphology seems to be correlated with the aggregate size, since the smaller size of the healthy aggregates may be a consequence of the higher compaction degree of these aggregates.

Another interesting parameter that should be further assessed is the CM yield, in order to evaluate if CM aggregate size variations between RTT and healthy conditions could result from differences in the number of CMs per aggregate. To assess the efficiency of the differentiation protocol for all the tested conditions, the percentage of cells positive for the cTnT marker was estimated by flow cytometry. The analysis of R2C6 aggregate samples revealed that the differentiation efficiency was affected by the CHIR concentration used (Figure 4.2 e, f; Supplementary Table 1). This is in line with the aggregate morphology described above. Although the screening for the various cell seeding conditions combined with different CHIR concentrations was only performed twice, and with a visible discrepancy for some of the tested conditions, a cell seeding density of 4000 cells/aggregate combined with 9 µM CHIR allowed to reach an efficient and reproducible percentage of cTnT in both biological replicates at D11-15 of differentiation (70.6% of $cTnT^+$ cells and 65.0% $cTnT^+$ cells), being this the selected optimal condition for this cell line.

Contrary to the expected, given the differences in the R255X M aggregate appearance, independently on the CHIR concentration used at D0, the cardiac differentiation efficiency was not affected (Figure 4.2 g; Supplementary Table 1). However, as it is possible to observe in the cell scattering plot (Figure 4.2 l), although the similarities in CM differentiation efficiencies, the cell population for the 7 µM CHIR condition is apparently distinct, mainly discriminated by the forward-scattered light (FSS) parameter. This suggests that these cells present a bigger size compared with 9 and 11 µM conditions, which could indicate differences in the type of the CM population generated or on the remaining $cTnT^-$ cells. Although more replicates are needed to definitely conclude which condition is optimal, based on the aggregate morphology and the differentiation process efficiency, the combination of a 4000 cells/aggregate density with a 11 µM CHIR concentration (76.1% $cTnT^+$ cells) was selected as the optimal condition.

In the case of the healthy cell lines, the DF6 aggregate samples presented an average of 78.8 ± 2.8 % of $cTnT^+$ cells, which proved the differentiation efficiency for this line, for 3800 cells/aggregate density and 11 µM CHIR concentration condition (Figure 4.2 h; Supplementary Table 1). Additionally, and once again contrarily to what was expected given the appearance of the R255X WT aggregates for the different CHIR concentration used at D0, the cardiac differentiation efficiency was not affected by this parameter (Figure 4.2 i; Supplementary Table 1). Although, similarly to the R255X M cell line, more replicates are needed to further characterize the optimal condition in terms of differentiation

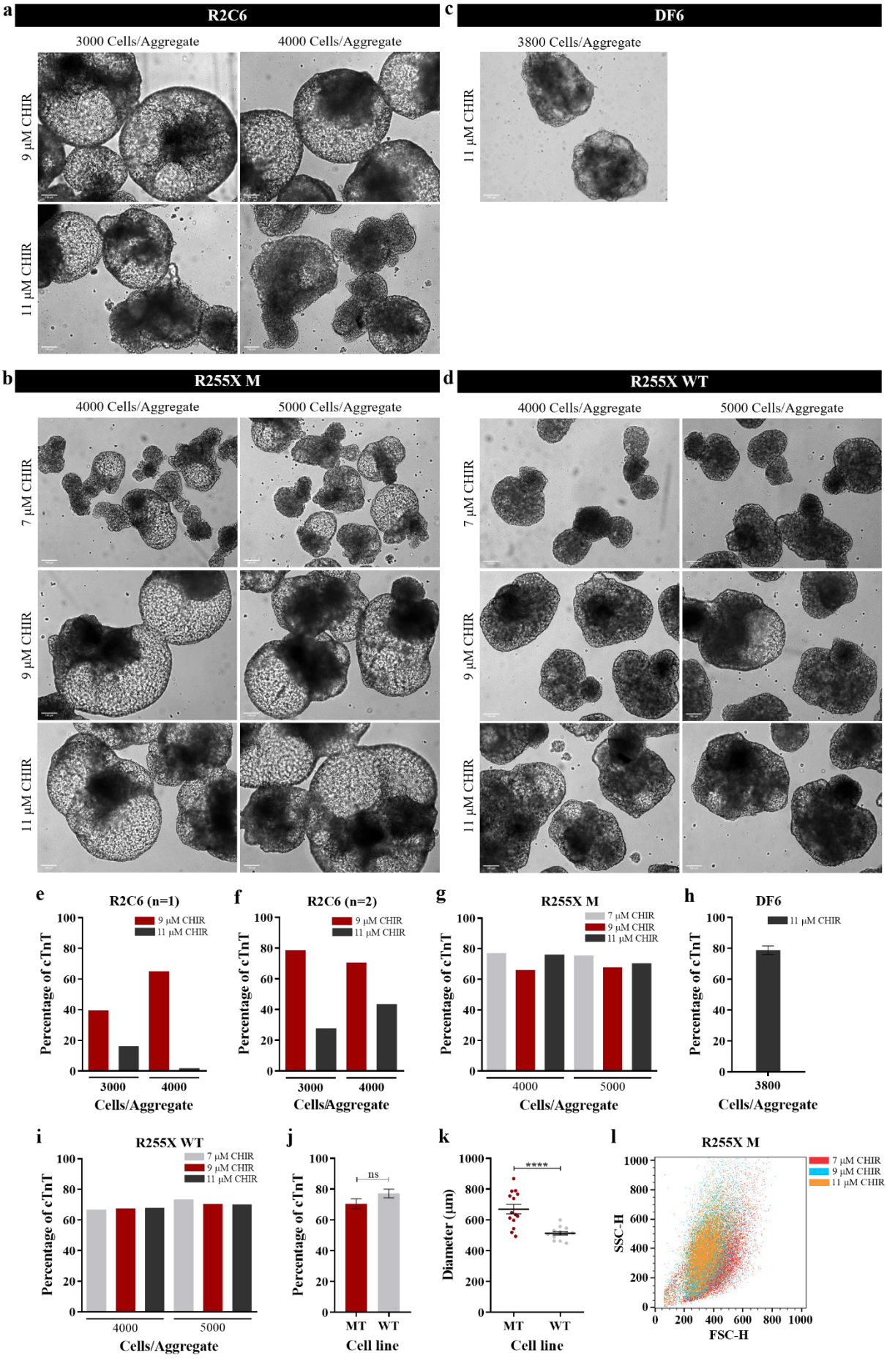
a
R2C6
3000 Cells/Aggregate
4000 Cells/Aggregate
9 µM CHIR
11 µM CHIR
c
DF6
3800 Cells/Aggregate
11 µM CHIR
b
R255X M
4000 Cells/Aggregate
5000 Cells/Aggregate
7 µM CHIR
9 µM CHIR
11 µM CHIR
d
R255X WT
4000 Cells/Aggregate
5000 Cells/Aggregate
7 µM CHIR
9 µM CHIR
11 µM CHIR
e
R2C6 (n=1)
9 µM CHIR
11 µM CHIR
Percentage of cTnT
Cells/Aggregate
3000
4000
f
R2C6 (n=2)
9 µM CHIR
11 µM CHIR
Percentage of cTnT
Cells/Aggregate
3000
4000
g
R255X M
7 µM CHIR
9 µM CHIR
11 µM CHIR
Percentage of cTnT
Cells/Aggregate
4000
5000
h
DF6
11 µM CHIR
Percentage of cTnT
Cells/Aggregate
3800
i
R255X WT
7 µM CHIR
9 µM CHIR
11 µM CHIR
Percentage of cTnT
Cells/Aggregate
4000
5000
j
ns
Percentage of cTnT
MT
WT
Cell line
k
****
Diameter (µm)
MT
WT
Cell line
l
R255X M
7 µM CHIR
9 µM CHIR
11 µM CHIR
SSC-H
FSC-H

Figure 4.2: Characterization of the period of hiPSC differentiation into CMs as 3D aggregates. BF images at D11-13 of **(a)** R2C6 aggregates for a cell seeding density of 3000 or 4000 cells/aggregate combined with 9 or 11 µM CHIR concentration; **(b)** R255X M aggregates for a cell seeding density of 4000 or 5000 cells/aggregate combined with 7, 9 or 11 µM CHIR concentration; **(c)** DF6 aggregates for a cell seeding density of 3800 cells/aggregate combined with 11 µM CHIR concentration; **(d)** R255X WT aggregates for a cell seeding density of 4000 or 5000 cells/aggregate combined with 7, 9 or 11 µM CHIR concentration. **(e-f)** Assessment of CM differentiation efficiency of R2C6 cell line for a cell seeding density of 3000 or 4000 cells/aggregate combined with 9 or 11 µM CHIR concentration by flow cytometry analysis for cTnT at D11-15. Mean ± SD; n=1 **(e)** and n=2 **(f)**. **(g)** Assessment of CM differentiation efficiency of R255X M cell line for a cell seeding density of 4000 or 5000 cells/aggregate combined with 7, 9 or 11 µM CHIR concentration by flow cytometry analysis for cTnT at D11-15. Mean ± SD; n=1 experiment. **(h)** Assessment of CM differentiation efficiency of DF6 cell line for a cell seeding density of 3800 cells/aggregate combined with 11 µM CHIR concentration by flow cytometry analysis for cTnT at D11-15. Mean ± SEM; n=6 experiments. **(i)** Assessment of CM differentiation efficiency for R255X WT cell line for a cell seeding density of 4000 or 5000 cells/aggregate combined with 7, 9 or 11 µM CHIR concentration by cTnT positive cells quantification through flow cytometry analysis at D11-15. Mean ± SD; n=1 experiment. **(j)** Comparison between MT and WT CM differentiation efficiency by flow cytometry analysis for cTnT at D11-15. Mean ± SEM. **(k)** Comparison between MT and WT aggregate size at D11-13. Mean ± SEM; measuring N=14 MT aggregates and N=13 WT aggregates. **(l)** Cell scattering plot resulting from flow cytometry analysis for cTnT at D11-15 of R255X M aggregate samples with a cell seeding density of 4000 cells/aggregate combined with 7, 9 or 11 µM CHIR concentration. n=1 experiment. The side-scattered light (SSC) parameter is proportional to cell granularity or internal complexity, while the FSC parameter is proportional to cell-surface area or size. MT aggregates correspond to the R2C6 cell line with the combination of a 4000 cells/aggregate density and a 9 µM CHIR concentration and the R255X M cell line with the combination of a 4000 cells/aggregate density and a 11 µM CHIR concentration; WT aggregates correspond to the DF6 cell line with the combination of a 3800 cells/aggregate density and a 11 µM CHIR concentration and the R255X WT cell line with the combination of a 4000 cells/aggregate density and a 11 µM CHIR concentration. Statistical analysis was performed using T-tests, with (****) $p < 0.0001$, (ns) not significant. Scale bars represent 100 µm.

efficiency, to be consistent with the R255X M cell line, a cell density of 4000 cells/aggregate and 11µM CHIR concentration was chosen as the optimal condition, corresponding to a CM differentiation efficiency of 67.8% of $cTnT^+$ cells.

Combining both MT and WT optimal conditions, it was observed an average of 70.6 ± 3.2 % of $cTnT^+$ cells for the MT lines and an average of 77.2 ± 2.8 % of $cTnT^+$ cells for the WT lines (Figure 4.2 j). Thus, in terms of differentiation efficiency, there were no significant differences between the RTT and healthy cell lines, being achieved for all tested cell lines a successful 3D CM differentiation.

Differentiation efficiencies were similar regardless of cell seeding density and CHIR concentration for the various cell lines, except for R2C6 aggregates. This discrepancy is potentially related with the distinct impact of CHIR concentration for R255X WT/M and R2C6 lines on CM differentiation efficiency, which can be related with the intrinsic variability in the basal activity signalling pathways between different hiPSC lines [178]. This can make one cell line more sensitive to the same level of Wnt signalling activation compared to other, which can justify the mentioned observations. Additionally, although the cell seeding density seems to have an impact on the efficiency of the differentiation in the case of R2C6 cell line, this result is still not irrefutably proved. Seeding with both 3000 and 4000 cells/aggregate resulted in aggregates with the same average size at D0 of differentiation, setting a priori the cell seeding density as not being a relevant parameter that would influence the efficiency of the differentiation. However, it is important to highlight that due to technical issues, as can be seen in (Figure 4.1 f, g, h, i; Supplementary Table 1), the size of R2C6 aggregates at D0 was more dispersed compared to the other lines. This introduced an extra parameter of variability that may be masking the impact of not only cell seeding density but ultimately also the impact of CHIR on CM differentiation efficiencies. The verification of this hypothesis highlights that heterogeneity in aggregate sizes at D0 affects the efficiency and reproducibility of differentiation.

Summing up, a successful differentiation of both RTT and healthy hiPSCs into CMs was established, as proved by spontaneous CM aggregate contraction and CM differentiation efficacies above 70% $cTnT^+$ for the four tested cell lines. It was observed a lower compaction degree and, consequently, more cavities, in the RTT aggregates, regardless of the tested conditions, as well as a higher aggregate size compared with healthy CM aggregates. The optimal cell seeding density ranged between 3800 and 4000 cells/aggregate, while the optimal CHIR concentration varied between 9 µM, in the case of R2C6

aggregates, and 11 µM for R255X M, DF6 and R255X WT, suggesting that these conditions were cell line-dependent and not a distinctive feature between RTT and healthy cell lines.

4.2. Structural Alterations on 3D Aggregates of Rett Syndrome Human Induced Pluripotent Stem Cell-derived Cardiomyocytes

Immunofluorescence staining of hiPSC-derived aggregate slices and replated CMs was performed at D12-19 of differentiation to characterize 1) the structural architecture and cellular composition of aggregates and 2) the CM sarcomere microstructure, respectively, and consequently assess RTT-derived alterations to these aspects.

Staining for the CM-specific marker cTnT proved the efficient differentiation of hiPSCs into CMs. Additionally, other cardiac cell types that are naturally present *in vivo* in the human heart were found in the differentiated aggregates. This was the case of ECs, which were stained with CD31 marker, and appear as cell population with a low prevalence (Figure 4.3 a, b). This is not surprising, as it has already been reported that similar manipulation of the Wnt signalling with CHIR also leads to endothelial progenitor differentiation [179]. Although at this stage of differentiation CMs were already $cTnT^{+}$/ISL1, it was commonly observed a core of $cTnT^{-}$ cells that express the CM progenitor marker ISL1, meaning that a pool of cardiac progenitor cells may still be present at this stage of differentiation (Figure 4.3 a, b, c).

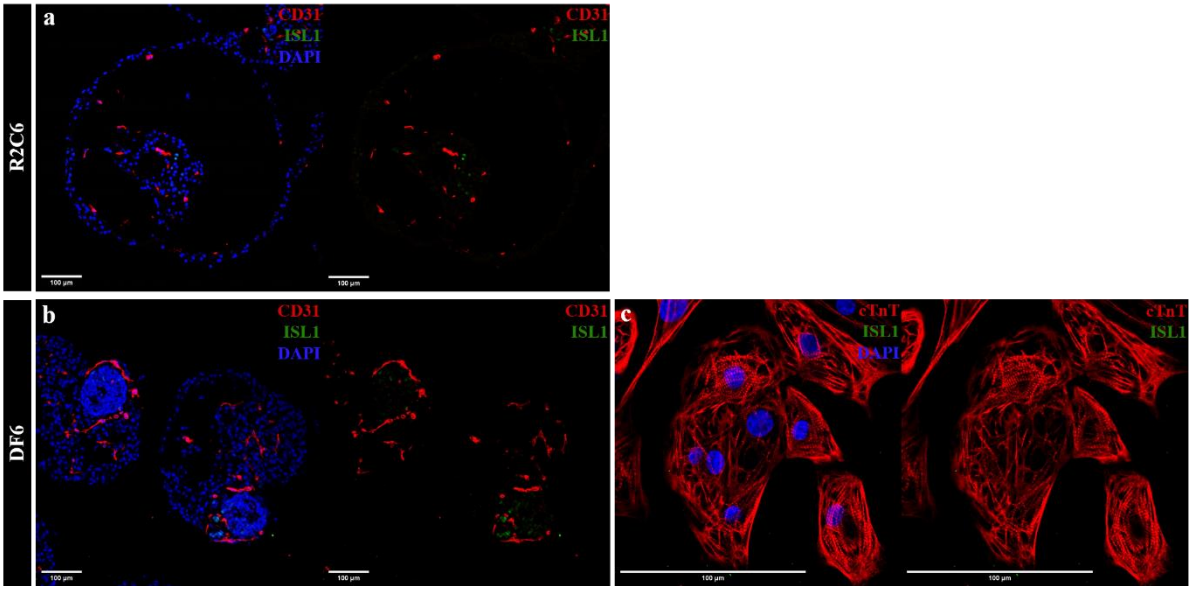

Figure 4.3: Characterization of the cardiac cell types present in the differentiated aggregates. **(a)** Immunofluorescence staining images of MT aggregate cryosections (R2C6 aggregates for a cell seeding density of 4000 cells/aggregate combined with 9 µM CHIR concentration) at D13 of differentiation. Cells were stained for CD31 in red (ECs) and ISL1 in green (cardiac progenitors). **(b)** Immunofluorescence staining images of WT aggregate cryosections (DF6 aggregates for a cell seeding density of 3800 cells/aggregate combined with 11 µM CHIR concentration) at D12 of differentiation. Cells were stained for CD31 in red (ECs) and ISL1 in green (cardiac progenitors). **(c)** Immunofluorescence staining images of replated WT aggregates (DF6 aggregates for a cell seeding density of 3800 cells/aggregate combined with 11 µM CHIR concentration) at D19 of differentiation. Cells were stained for cTnT in red (CM fibers) and ISL1 in green (cardiac progenitors). Nuclei in blue were stained with DAPI. Scale bars represent 100 µm.

4.2.1. Cardiomyocyte Aggregate Cavities

Through immunofluorescence staining images of aggregate slices (Figure 4.4 a, b, c), it was possible to characterize the CM aggregate cavities, which were identified as the internal aggregate compartments that do not stain for DAPI. This specific analysed parameter revealed interesting differences between the RTT and healthy aggregates, as previously suggested by the BF observations. To characterize the differences in cavities in both conditions, three parameters were considered, including 1) the number of cavities per aggregate slice, 2) the percentage of aggregate slice area occupied by cavities, and 3) the proportion of cavities according to their size.

The R2C6 and DF6 aggregate slices presented an average of 7.0 ± 0.5 and 7.7 ± 1.1 cavities per slice, respectively, while the R255X WT aggregates exhibited an average of 10.4 ± 1.6 cavities per aggregate slice (Figure 4.4 d). It was thus concluded that the number of cavities per aggregate slice was not a distinctive characteristic between MT and WT cell lines (7.0 ± 0.5 cavities for MT line and 8.5 ± 0.9 cavities for WT lines) (Figure 4.4 e).

On the other hand, it was observed a considerable difference regarding the percentage of R2C6 aggregate area occupied by cavities compared to the percentage observed in DF6 or R255X WT aggregates (Figure 4.4 f). In R2C6 aggregates, 54.1 ± 3.2 % of the area was occupied by cavities. On the opposite side, the DF6 and R255X WT aggregates were much more compact, exhibiting only 17.3 ± 2.0 % and 12.5 ± 2.5 %, respectively, of their area occupied by cavities. The percentage of aggregate area occupied by cavities is thus a distinctive parameter between MT and WT lines, with cavities occupying, on average, 54.1 ± 3.2 % of the MT aggregates and 15.8 ± 1.6 % of the WT aggregates (Figure 4.4 g).

Another interesting parameter studied was the size of the cavities. Four area ranges were considered, numbered from the lowest to the highest values, including 1) from 0 to 1 000 μm^2, designated the first range; 2) from 1 001 to 10 000 μm^2, referred to as the second range; 3) from 10 001 to 100 000 μm^2, called the third range; and 4) from 100 001 to 1 000 000 μm^2, named the fourth range (Table 3.3). The values obtained for the DF6 and R255X WT aggregate cavity sizes were very similar (Figure 4.4 h; Supplementary Figure 4). Therefore, the analysis will focus on directly comparing RTT and healthy lines (Figure 4.4 i). Most aggregate cavities were in the first two value ranges, corresponding to the smallest areas. However, comparing MT and WT aggregates, it was found that, while in the MT case, this value corresponds to 77.2%, for the WT, the value was noticeably higher, standing at 97.7%. The MT aggregate cavities showed a very variable size, being distributed over the four area ranges considered. 41.6% of the cavities presented an area belonging to the second range, followed by 35.5% of the cavities with an area belonging to the smaller area range, 16.8% in the third range and 6.1% in the last range, which includes the higher areas. This last value is noteworthy, since about 6% of the cavities had an area of the same magnitude range as the area of the aggregates themselves, values never reached by the WT aggregates. These WT aggregate cavities occupied a much smaller aggregate area overall than in the MT case. In this case, the number of cavities was inversely proportional to the increase in the considered area range, with 60.3% of the cavities having an area belonging to the first range, 37.4% to the second and 2.3% to the third.

In a study performed by Hofbauer et al. [180], it was described that the level of Wnt and BMP4 signalling pathways activation at early stages of differentiation impacts the generation of cavities in cardiac organoids and their sizes. Thus, it will be interesting to assess if one or both of the mentioned pathways could be altered and therefore condition the structural differences observed between RTT and healthy aggregates. The same study also revealed that HAND1 knockout cardiac organoids showed a defect in cardiac cavity self-organization and size (smaller size cardioids with smaller cavities, with no difference in the cell number per cardioid), highlighting the need of HAND1 for cardioid self-

organization. According to this and given our results, it may be interesting to study in the future the expression levels of HAND1 in both RTT- and WT-derived CM aggregates.

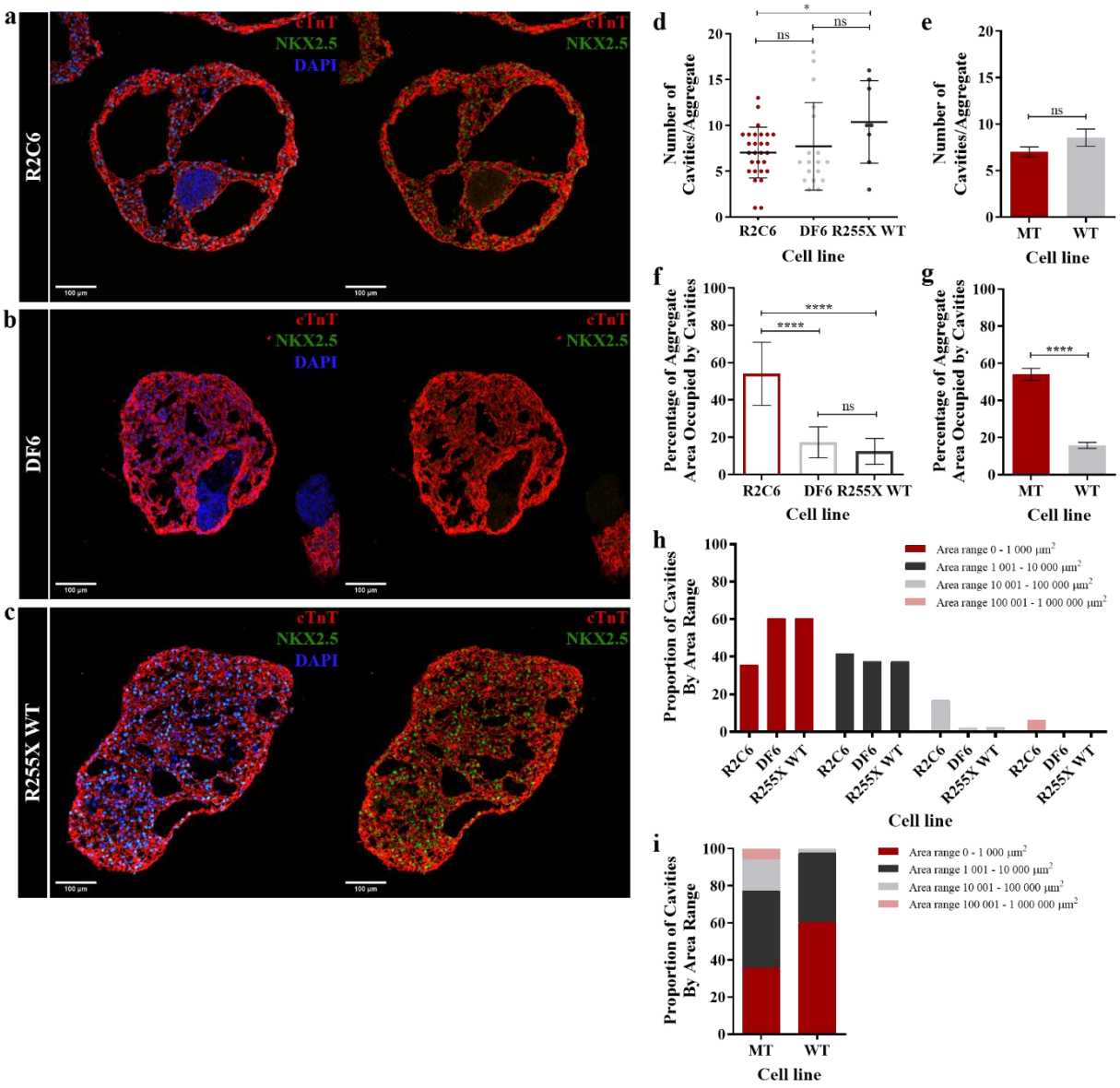

Figure 4.4: Characterization of the CM aggregate cavities. **(a)** Immunofluorescence staining images of MT aggregate cryosections (R2C6 aggregates for a cell seeding density of 4000 cells/aggregate combined with 9 µM CHIR concentration) at D13 of differentiation. Cells were stained for cTnT in red (CM fibers) and NKX2.5 in green (CM nuclei). **(b)** and **(c)** Immunofluorescence staining images of WT aggregate cryosections (DF6 aggregates for a cell seeding density of 3800 cells/aggregate combined with 11 µM CHIR concentration at D12 of differentiation; and R255X WT aggregates for a cell seeding density of 4000 cells/aggregate combined with 11 µM CHIR concentration at D15 of differentiation, respectively). Cells were stained for cTnT in red (CM fibers) and NKX2.5 in green (CM nuclei). Nuclei in blue were stained with DAPI. **(d)** Number of cavities per aggregate of R2C6, DF6 and R255X WT cell lines. Mean ± SD. **(e)** Comparison between the number of cavities per aggregate of MT and WT aggregates. Mean ± SEM. **(f)** Percentage of aggregate area occupied by cavities of R2C6, DF6 and R255X WT cell lines. Mean ± SD. **(g)** Comparison between the percentage of aggregate area occupied by cavities of MT and WT aggregates. Mean ± SEM. **(h)** Proportion of cavities per area range of R2C6, DF6 and R255X WT cell lines. Four area ranges were considered: from 0 to 1 000 µm^2; from 1 001 to 10 000 µm^2; from 10 001 to 100 000 µm^2; from 100 001 to 1 000 000 µm^2. **(i)** Comparison between the proportion of cavities according to their size of MT and WT aggregates. The same described four area ranges were used. N=28 R2C6 aggregates, N=18 DF6 aggregates and N=8 R255X WT aggregates were measured. MT aggregates correspond to R2C6 aggregates and WT aggregates to DF6 and R255X WT aggregates. Statistical analysis was performed using T-tests, with (*) $p < 0.05$, (****) $p < 0.0001$, (ns) not significant. Scale bars represent 100 µm.

4.2.1.1. Proliferation of Mutated and Wild-Type Cardiomyocytes

Given the differences between RTT and healthy aggregates regarding the percentage of aggregate area occupied by cavities as well as the size of the cavities, we hypothesised that differences concerning CM proliferation may contribute to the observed results. To evaluate this hypothesis, we performed immunofluorescence analysis of replated CM aggregates derived from R255X M and DF6 cell lines for Ki-67 at D15 and D19 of differentiation, respectively (Figure 4.5 a, b). No significant differences were found regarding the percentage of proliferative CMs between MT and WT aggregates (46.1 ± 3.6 % and 41.1 ± 4.3 %, respectively) (Figure 4.5 c). Although more replicates are needed to confirm this result, the obtained data suggests that differences between the RTT and healthy aggregate cavities were not driven by a different CM proliferation profile. An immunostaining assay for the apoptotic marker CASPASE should be evaluated in the future in order to study whether cavity formation is driven by cell death. If cavity expansion is not driven by regional proliferation differences nor by apoptosis, the most reasonable hypothesis is that smaller cavities eventually coalesced into bigger cavities in RTT aggregates, as suggested by [180]. In this case, and in accordance with what was mentioned above, a higher coalescence of the RTT aggregate cavities could be due to a change in the level of Wnt and BMP4 signalling pathways activation at early stages of cardiac differentiation or/and result from differences in HAND1 expression levels in MT and WT-derived CM aggregates.

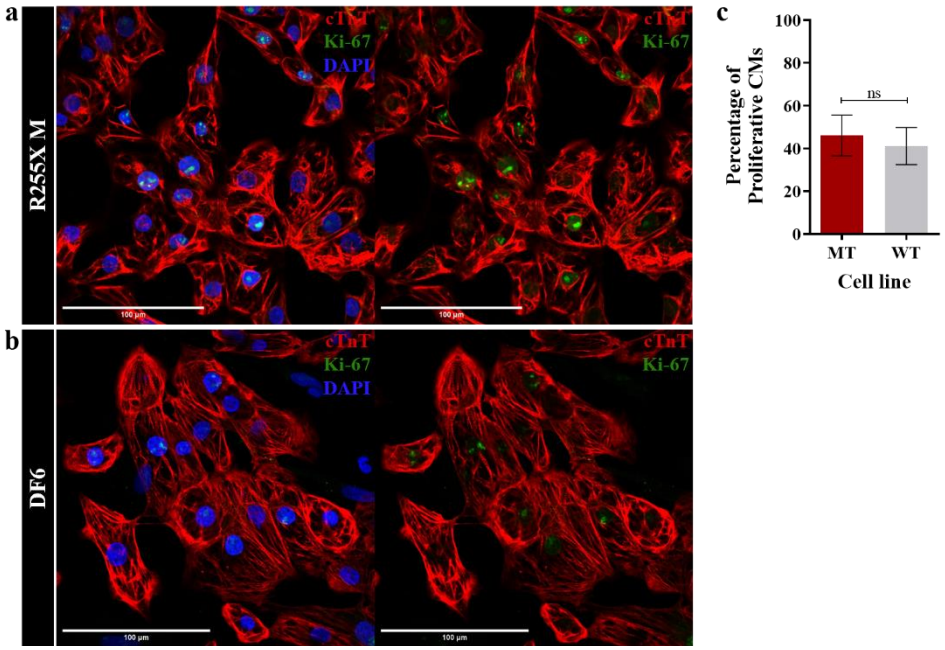

Figure 4.5: Characterization of proliferation in replated CMs from aggregates. **(a)** Immunofluorescence staining images of replated MT aggregates (R255X M aggregates for a cell seeding density of 4000 cells/aggregate combined with 11 µM CHIR concentration) at D15 of differentiation. Cells were stained for cTnT in red (CM fibers) and Ki-67 in green (cell proliferation). **(b)** Immunofluorescence staining images of replated WT aggregates (DF6 aggregates for a cell seeding density of 3800 cells/aggregate combined with 11 µM CHIR concentration) at D19 of differentiation. Cells were stained for cTnT in red (CM fibers) and Ki-67 in green (cell proliferation). Nuclei in blue were stained with DAPI. **(c)** Comparison between the percentage of proliferative CMs in MT and WT aggregates. Mean ± SD; measuring N = 208 MT CMs and N=129 WT CMs. Statistical analysis was performed using T-tests, with (ns) not significant. Scale bars represent 100 µm.

4.2.2. Characterization of Replated Cardiomyocyte Sarcomeres

CMs are composed of myofibril bundles, each of them consisting of distinct and repeating sarcomeres. These sarcomeres are the structural units of the contractile apparatus in cardiac muscle cells,

meaning they are the basic force-generating unit of cardiac muscle. Sarcomeres are composed of two types of myofilaments, namely 1) myosin, which forms the thick filaments, and 2) actin, which forms the thin filaments. The sarcomere borders are protein complexes called Z-bands, to which the actin myofilaments are attached, through the α-actinin protein [177], [181].

Sarcomere feature alterations are indicative of changes in sarcomeric proteins and their function during development and disease. In fact, the size, alignment, and distribution of sarcomeres within a CM is often used as an indicator of CM maturity and functionality. Thus, we performed the evaluation of sarcomere structural parameters for replated CMs. Based on immunofluorescence staining images for α-actinin, which stains Z-bands and is an excellent marker to evaluate sarcomeric integrity, we assessed the sarcomere length and whether this parameter was significantly different in CMs derived from RTT cell lines compared to healthy ones.

Through immunofluorescence staining images, a difference between sarcomere organization, shape and spatial distribution between RTT and healthy lines was evident. In the WT line (DF6 hiPSC-derived CMs), it was possible to distinguish cells with organized sarcomeres, characterized by the striated pattern of α-actinin staining. In contrast, MT line (R255X M hiPSC-derived CMs) sarcomeres were much less organized. The clearly identifiable Z-bands in the sarcomeres of the WT line contrast with the MT line, where some CMs present dots (and not bands) stained by α-actinin, which raises doubts regarding the contractile apparatus integrity. Interestingly, it was also observed that in MT CMs, striated sarcomeres were more concentrated around the cell nucleus, whereas WT CMs were uniformly distributed across the cytoplasm (Figure 4.6 a, b).

SotaTool software was used to quantify the sarcomere length [177]. This is an automated image analysis tool that allows quantifying sarcomere organization regardless of the cell shape and orientation and image magnification. Only two parameters were manipulated in the SotaTool interface, including image resolution and segmentation. The image resolution is a fixed value and was determined through ImageJ. On the other hand, the segmentation automatically segments the original images and can be successively increased, according to the image characteristics and the analysis purpose, which in turn also increases the computation time (Figure 4.6 c). Repeated striations, as is the sarcomere case, result in damped oscillating correlation graphs, where the sarcomere length can be determined as the distance to the first peak (Figure 4.6 d).

Firstly, three segmentations were tested with the WT line images, namely 4x4, 5x5 and 6x6, in order to determine the impact that this parameter could have on sarcomere length determination (Figure 4.6 c). Intuitively, the higher the segmentation value, the smaller the original image section is analysed at a time. The analysis revealed that the sarcomeres presented an average length of 1.67 ± 0.030 μm using a 4x4 segmentation, 1.69 ± 0.024 μm for the 5x5 segmentation and 1.70 ± 0.021 μm using a 6x6 segmentation, whose values did not differ significantly from each other (Figure 4.6 e). Since the MT CM sarcomeres were much less organized and the staining was more punctual, not being uniformly spread, a greater segmentation of the original image was necessary to quantify the sarcomere size. The software was not able to determine the parameter under study with a segmentation lower than 6x6. Therefore, the cell lines were compared based on a 6x6 segmentation of the original images. The average sarcomere length of the MT CMs (1.55 ± 0.038 μm) was significantly lower compared with the WT CMs (1.70 ± 0.021 μm), as seen in the comparison between the MT segmented images and WT ones (Figure 4.6 c, f).

Adult human CMs typically present sarcomeres with about 2.20 μm length. Immature hPSC-derived CMs typically have a shorter sarcomere length, in the range of 1.65–2.00 μm [177], [181], which results in contractile impairment. Although in both cases, WT and MT CMs presented a value that was lower than 2.20 μm, as expected taking into consideration the differentiation time point at which CMs were analysed, it should be noted that the sarcomere length value of the MT line CMs was lower than the lower limit of the range reported in the literature for immature CMs. Therefore, it is speculated that the

even more drastic reduction in the sarcomere length of the MT line CMs has a further limiting role in the contraction performance of these CMs.

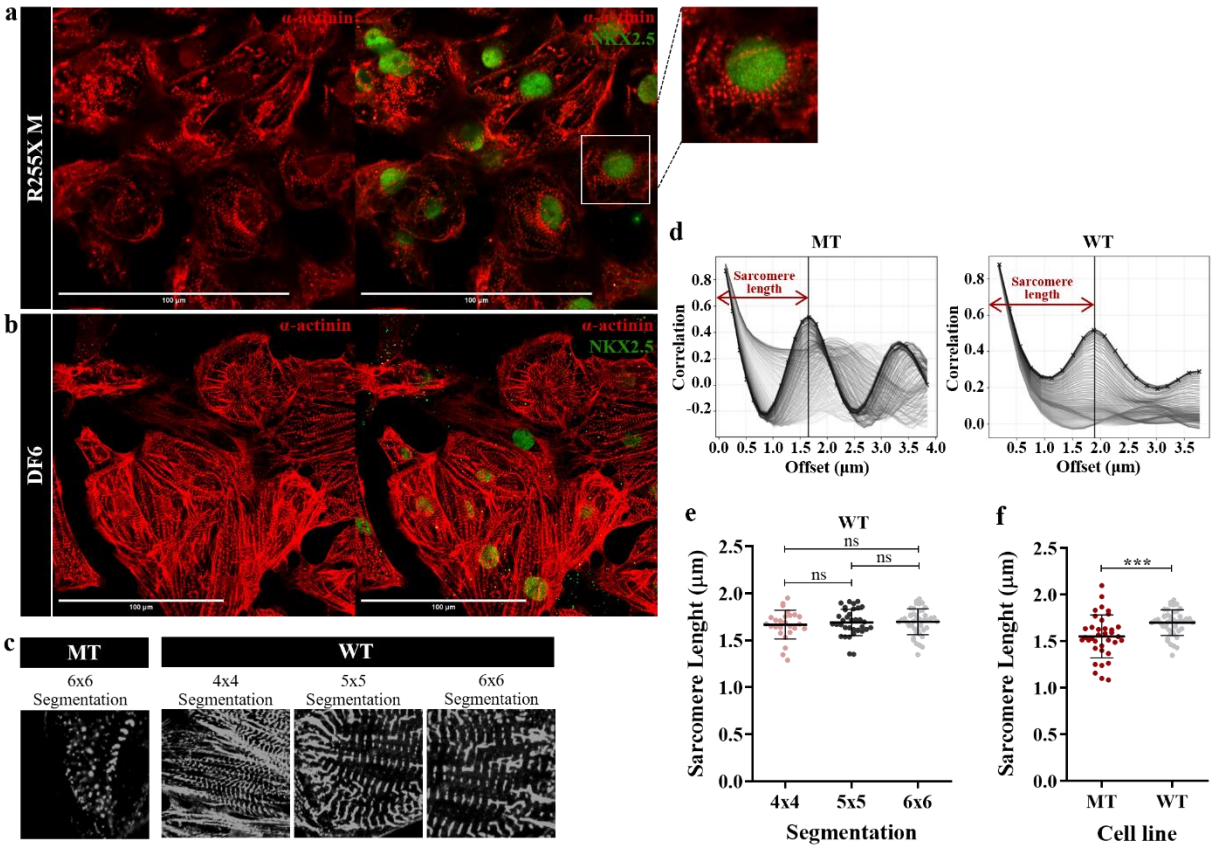

Figure 4.6: Characterization of sarcomeres in replated CMs from aggregates. **(a)** Immunofluorescence staining images of replated MT aggregates (R255X M aggregates for a cell seeding density of 4000 cells/aggregate combined with 11 μM CHIR concentration) at D15 of differentiation. Cells were stained for α-actinin in red (CM sarcomeres) and NKX2.5 in green (CM nuclei). Zoomed section show evidence that the MT sarcomeres were more concentrated around the cell nucleus. **(b)** Immunofluorescence staining images of replated WT aggregates (DF6 aggregates for a cell seeding density of 3800 cells/aggregate combined with 11 μM CHIR concentration) at D19 of differentiation. Cells were stained for α-actinin in red (CM sarcomeres) and NKX2.5 in green (CM nuclei). **(c)** Segments resulting from the segmentation of the original immunofluorescence staining images. One segmentation (6x6) with the MT line images and three segmentations (4x4, 5x5 and 6x6) with the WT line images were tested. **(d)** Damped oscillating correlation graphs derived from SotaTool software. Sarcomere length is given by the distance to the first peak. The left graph corresponds to the MT cell line data and the right graph to the WT cell line data. **(e)** Sarcomere length for 4x4, 5x5 and 6x6 segmentations of the WT cell line images. Mean ± SD; 4x4, 5x5 and 6x6 segmentation resulted in N=26, N=35 and N=44 measurements, respectively. **(f)** Sarcomere length comparison between 6x6 segmented images of MT and WT cell lines. Mean ± SD; segmentation resulted in N=36 measurements for the MT cell line and N=44 measurements for the WT cell line. MT aggregates correspond to R255X M aggregates and WT aggregates to DF6 aggregates. Statistical analysis was performed using T-tests, with (***) $p < 0.001$, (ns) not significant. Scale bars represent 100 μm.

Together, these findings suggest that RTT hiPSC-derived CMs present sarcomere structural impairment, with a lower density of myofibril, the presence of which was more pronounced near the CM nucleus, and a shorter sarcomere length, compared to healthy CMs. In diseased settings, the sarcomere structural impairment culminates in a diminished contraction force, jeopardizing the normal function of the heart. In the future, in addition to a more in-depth study of the discussed structural parameters and others, as evaluating the sarcomere shortening, it will be essential to perform a functional analysis of RTT and healthy CMs. Functional alterations on RTT hiPSC-derived CMs, such as contraction duration and beating rate, can be evaluated using intracellular calcium transient analysis, under standard conditions and upon exposure to drugs that are known to elicit an increased and/or

arrhythmic CM contraction (as is the case of isoproterenol and E-4031), or through electrical stimulation using MEA.

Overall, this project allowed the identification of RTT-derived alterations to the process of cardiac differentiation from hiPSCs into CMs as 3D aggregates, through the study of several parameters, namely both macro and microstructural aspects. Consequently, it was possible to establish a parallelism between RTT and healthy hiPSC-derived CM aggregates, as summarized in Table 4.1, which highlighted extremely interesting and exciting results.

Table 4.1: Summary of the parameters evaluated in this project and their comparison between RTT and healthy conditions.

	Parameters		RTT	Healthy
3D hiPSC-derived CM aggregates	Contraction		• Yes.	• Yes.
	Diameter		• 670.5 ± 30.7 μm.	• 513.5 ± 11.6 μm.
	Morphology		• Less compact; • More cavities.	• More compact; • Less cavities.
	Cellular composition		• CMs (majority); • ECs; • Pool of progenitor cells.	• CMs (majority); • ECs; • Pool of progenitor cells.
	Number of cavities per aggregate		• 7.0 ± 0.5.	• 8.5 ± 0.9.
	Percentage of aggregate area occupied by cavities		• 54.1 ± 3.2 %.	• 15.8 ± 1.6 %.
	Size of the cavities		• Variable, with values being distributed over the four area ranges; • 77.2% of the cavities within the first two area ranges, corresponding to the smallest areas; • 6% of the cavities presented an area of the same magnitude range as the area of the aggregates themselves.	• Variable, with values being distributed over the three smaller area ranges; • 97.7% of the cavities within the first two area ranges, corresponding to the smallest areas.
	Percentage of proliferative CMs		• 46.1 ± 3.6 %.	• 41.1 ± 4.3 %.
hiPSC-derived CMs	Sarcomere	length	• 1.55 ± 0.038 μm.	• 1.70 ± 0.021 μm.
		shape	• Dots.	• Bands.
		organization	• Less organized.	• More organized.
		spatial distribution	• Lower density; • More concentrated around the cell nucleus.	• Higher density; • Uniformly distributed across the cytoplasm.

Chapter 5

Conclusions and Future Work

Given the RTT multifaceted nature, it has been proven challenging to accurately mimic the myriad of phenotypes associated with this disorder and to investigate and develop therapies for these patients. Besides presenting neurological complications, RTT patients suffer from a wide array of non-neurological problems, including cardiac abnormalities. The analysis of brain development and function has been the focus of the vast majority of models that have been used to study RTT, with very few mimicking the disease in the heart. Furthermore, although animal models have been making significant contributions to disease recapitulation, their clinical relevance is affected by the differences between species and the diversity among patients can hardly be modelled using these strategies. To overcome this limitation, more recently, hPSCs have emerged as a promising alternative for the study of RTT. However, to date, there are no reported hPSC-derived cardiac models of RTT. In this context, this innovative work is extremely relevant, as it intended to modulate RTT with 3D cardiac models derived from patient-specific hiPSCs.

Firstly, our results demonstrated that it is possible to successfully differentiate both RTT and healthy hiPSCs into CMs as 3D aggregates. We were able to optimize the process of cardiac differentiation for each cell line, by varying two parameters, namely the aggregate size at D0 of differentiation and the CHIR concentration. Although the optimal values for these parameters varied according to the cell line, the results obtained suggested that these conditions were cell line-dependent and not a distinctive parameter between MT and WT cell lines. Regarding the study of RTT-derived alterations to the process of cardiac differentiation, it is important to highlight the differences observed in the size and compaction degree of the aggregates, being higher and lower, respectively, in the MT aggregates compared to the WT ones. Secondly, structural alterations between RTT hiPSC-derived CM aggregates and controls were evaluated. In addition to CMs, other cardiac cell types that are naturally present *in vivo* in the human heart were also found, as a minority, in the differentiated aggregates, such as ECs and a pool of cardiac progenitor cells. The aggregate cavity characterization revealed interesting differences between RTT CM aggregates and controls, including a much higher percentage of MT aggregate area occupied by cavities comparing to WT aggregates, which was not related to the number of cavities per aggregate, parameter that was similar between conditions. It was also reported a variation in the proportion of cavities according to their size between MT and WT aggregates. Additionally, we investigate whether the disparity between the MT and WT aggregate cavities was not driven by CM proliferation differences. Lastly, our results suggest that RTT hiPSC-derived CMs present sarcomere structural impairment, with a lower density of myofibril, the presence of which was more pronounced near the CM nucleus, and a shorter sarcomere length, compared to healthy CMs.

In the future, more replicates will be needed to confirm our findings. Moreover, it will be essential to use other cell lines in the experiments, including hiPSC lines derived from patients with different RTT-associated mutations, to validate our results. Additionally, a more detailed analysis of RTT-derived

changes in the CM differentiation process and of the structural alterations of RTT hiPSC-derived CMs should be performed. The process of cardiac differentiation of RTT and healthy hiPSC lines should be characterized in terms of kinetics and levels of gene expression of the main genes involved in hPSC cardiac differentiation (e.g. T, ISL1, MESP1, NKX2.5, TNNT2) and CM maturation (e.g. MYL7, MYH7, MYL2, MYH6), performing molecular profiling using real-time polymerase chain reaction (RT-PCR). Moreover, RNA sequencing (RNA-seq) could be used as a complementary strategy to assess in depth the origin of the possible differences observed between MT and WT conditions. Regarding the structural analysis, and particularly related with the aggregate cavities, it would be interesting to evaluate the level of Wnt and BMP4 signalling pathways activation at early stages of cardiac differentiation, since its alteration can impact the structural differences observed between MT and WT aggregates [180]. Furthermore, the assessment of the HAND1 expression levels in both MT- and WT-derived CM aggregates would also be interesting, as HAND1 has been reported to interfere with cavity-like self-organization [180]. To complement the study of the aggregate cavity expansion, an immunostaining assay for the apoptotic marker CASPASE should be performed, in order to study whether cell death drives cavity formation. On the other hand, it would be extremely relevant to evaluate the functional alterations on RTT CMs. Particularly, the contraction duration and beating rate are some of the parameters that could be assessed using intracellular calcium transient analysis, under standard conditions and upon exposure to drugs that are known to elicit an increased and/or arrhythmic CM contraction, as is the case of isoproterenol and E-4031, or through electrical stimulation using MEA.

However, the CM culture per se may not allow to observe the cardiac functional abnormalities that have already been described in humans. As previously discussed, CMs and neurons undergo co-maturation during the heart innervation in embryogenesis. Therefore, the study of the interactions between these cell types is essential, especially to model multi-systemic diseases such as RTT. For these reasons, in a subsequent phase, it would be interesting to increase the complexity of our system, by co-culturing hiPSC-derived CMs with hiPSC-derived ANS neurons. For that purpose, we could either use a compartmentalized chip, restricting cell-to-cell interactions to axons extending through microtunnels between the isolated compartments of neuronal somas and CMs [129], [172]–[174]; or seed CMs on top of neurons, not restricting cell-to-cell contacts and allowing the formation of functional interactions between both cell types [168], [171], [175], [176]. These approaches would allow the capture of potential functional alterations of RTT CMs promoted by RTT ANS neurons, assessing whether the CM dysfunctional phenotype would be exacerbated in co-culture. To do so, it could be evaluated the effect of electrical and/or chemical stimulation applied to neurons on CM contraction duration and beating rate; as well as the effect of co-culture on neuron and CM maturation. The development of a model with these characteristics would be an important step in the modelling of this disorder, eventually allowing the unveiling of information about a potential defective cross-talk between these two cell populations which, to date, remains unknown.

Moreover, in the future it would also be interesting to recreate the heterogeneity of cardiac cells present in the human heart. For instance, this could be achieved by generating a cardiac multicellular spheroid microtissue, comprising both CM, CFs and ECs, or a self-organized cardiac organoid, composed of the same cell types. Both models, with different complexity degrees and cardiac cell interactions, would be extremely relevant. On the one hand, they would allow studying cell maturation and the general function of CMs in comparison with the simpler healthy model. On the other hand, they could enable us to understand whether the main steps that occur during the cardiac development process in embryogenesis, the way different cell populations are specified, and the CM function are or not affected by RTT. Posteriorly, these models could also be co-cultured with neurons, establishing a complex 3D neuro-cardiac model for the study of this disease.

References

[1] ‘Rett Syndrome’. https://emedicine.medscape.com/article/916377-overview (accessed Sep. 05, 2022).

[2] ‘International Rett Syndrome Foundation (IRSF)’. https://www.rettsyndrome.org/ (accessed Sep. 05, 2022).

[3] A. R. Gomes, T. G. Fernandes, J. M. S. Cabral, and M. M. Diogo, ‘Modeling Rett Syndrome with Human Pluripotent Stem Cells: Mechanistic Outcomes and Future Clinical Perspectives’, *Int. J. Mol. Sci.*, vol. 22, no. 7, p. 3751, Apr. 2021, doi: 10.3390/ijms22073751.

[4] ‘Rett Syndrome’. https://www.statpearls.com/point-of-care/28490 (accessed Sep. 05, 2022).

[5] B. Hendrich and S. Tweedie, ‘The methyl-CpG binding domain and the evolving role of DNA methylation in animals’, *Trends Genet.*, vol. 19, no. 5, pp. 269–277, May 2003, doi: 10.1016/S0168-9525(03)00080-5.

[6] N. Vashi and M. J. Justice, ‘Treating Rett syndrome: from mouse models to human therapies’, *Mamm. Genome*, vol. 30, no. 5–6, pp. 90–110, Jun. 2019, doi: 10.1007/s00335-019-09793-5.

[7] J. Guy, B. Hendrich, M. Holmes, J. E. Martin, and A. Bird, ‘A mouse Mecp2-null mutation causes neurological symptoms that mimic Rett syndrome’, *Nat. Genet.*, vol. 27, no. 3, pp. 322–326, Mar. 2001, doi: 10.1038/85899.

[8] R. Z. Chen, S. Akbarian, M. Tudor, and R. Jaenisch, ‘Deficiency of methyl-CpG binding protein-2 in CNS neurons results in a Rett-like phenotype in mice’, *Nat. Genet.*, vol. 27, no. 3, pp. 327–331, Mar. 2001, doi: 10.1038/85906.

[9] K. Brown, J. Selfridge, S. Lagger, J. Connelly, D. De Sousa, A. Kerr, S. Webb, J. Guy, C. Merusi, M. V. Koerner, and A. Bird, ‘The molecular basis of variable phenotypic severity among common missense mutations causing Rett syndrome’, *Hum. Mol. Genet.*, vol. 25, no. 3, pp. 558–570, Feb. 2016, doi: 10.1093/hmg/ddv496.

[10] M. J. Lyst, R. Ekiert, D. H. Ebert, C. Merusi, J. Nowak, J. Selfridge, J. Guy, N. R. Kastan, N. D. Robinson, F. de Lima Alves, J. Rappsilber, M. E. Greenberg, and A. Bird, ‘Rett syndrome mutations abolish the interaction of MeCP2 with the NCoR/SMRT co-repressor’, *Nat. Neurosci.*, vol. 16, no. 7, pp. 898–902, Jul. 2013, doi: 10.1038/nn.3434.

[11] A. Lawson-Yuen, D. Liu, L. Han, Z. I. Jiang, G. E. Tsai, A. C. Basu, J. Picker, J. Feng, and J. T. Coyle, ‘Ube3a mRNA and protein expression are not decreased in Mecp2 mutant mice’, *Brain Res.*, vol. 1180, pp. 1–6, Nov. 2007, doi: 10.1016/j.brainres.2007.08.039.

[12] L. R. Schaevitz, N. B. Gómez, D. P. Zhen, and J. E. Berger-Sweeney, ‘MeCP2 R168X male and female mutant mice exhibit Rett-like behavioral deficits’, *Genes, Brain Behav.*, p. n/a-n/a, Aug. 2013, doi: 10.1111/gbb.12070.

[13] E. Wegener, C. Brendel, A. Fischer, S. Hülsmann, J. Gärtner, and P. Huppke, ‘Characterization of the MeCP2R168X Knockin Mouse Model for Rett Syndrome’, *PLoS One*, vol. 9, no. 12, p. e115444, Dec. 2014, doi: 10.1371/journal.pone.0115444.

[14] M. R. Pitcher, J. A. Herrera, S. A. Buffington, M. Y. Kochukov, J. K. Merritt, A. R. Fisher, N. C. Schanen, M. Costa-Mattioli, and J. L. Neul, ‘Rett syndrome like phenotypes in the R255X Mecp2 mutant mouse are rescued by MECP2 transgene’, *Hum. Mol. Genet.*, vol. 24, no. 9, pp. 2662–2672, May 2015, doi: 10.1093/hmg/ddv030.

[15] M. Itoh, C. G. T. Tahimic, S. Ide, A. Otsuki, T. Sasaoka, S. Noguchi, M. Oshimura, Y. Goto, and A. Kurimasa, ‘Methyl CpG-binding Protein Isoform MeCP2_e2 Is Dispensable for Rett Syndrome Phenotypes but Essential for Embryo Viability and Placenta Development’, *J. Biol. Chem.*, vol. 287, no. 17, pp. 13859–13867, Apr. 2012, doi: 10.1074/jbc.M111.309864.

[16] D. H. Yasui, M. L. Gonzales, J. O. Aflatooni, F. K. Crary, D. J. Hu, B. J. Gavino, M. S. Golub, J. B. Vincent, N. C. Schanen, C. O. Olson, M. Rastegar, and J. M. Lasalle, ‘Mice with an isoform-ablating Mecp2 exon 1 mutation recapitulate the neurologic deficits of Rett syndrome’, *Hum. Mol. Genet.*, vol. 23, no. 9, pp. 2447–2458, May 2014, doi: 10.1093/hmg/ddt640.

[17] R. C. Samaco, J. D. Fryer, J. Ren, S. Fyffe, H.-T. Chao, Y. Sun, J. J. Greer, H. Y. Zoghbi, and J. L. Neul, ‘A partial loss of function allele of Methyl-CpG-binding protein 2 predicts a human neurodevelopmental syndrome’, *Hum. Mol. Genet.*, vol. 17, no. 12, pp. 1718–1727, Mar. 2008, doi: 10.1093/hmg/ddn062.

[18] J. Guy, J. Gan, J. Selfridge, S. Cobb, and A. Bird, ‘Reversal of Neurological Defects in a Mouse Model of Rett Syndrome’, *Science (80-.).*, vol. 315, no. 5815, pp. 1143–1147, Feb. 2007, doi: 10.1126/science.1138389.

[19] B. Hagberg, I. Witt-Engerström, J. M. Opitz, and J. F. Reynolds, ‘Rett Syndrome: A suggested staging system for describing impairment profile with increasing age towards adolescence’, *Am. J. Med. Genet.*, vol. 25, no. S1, pp. 47–59, 1986, doi: 10.1002/ajmg.1320250506.

[20] M. Chahrour and H. Y. Zoghbi, ‘The Story of Rett Syndrome: From Clinic to Neurobiology’, *Neuron*, vol. 56, no. 3, pp. 422–437, Nov. 2007, doi: 10.1016/j.neuron.2007.10.001.

[21] C. Elefant and T. Wigram, ‘Learning ability in children with Rett syndrome’, *Brain Dev.*, vol. 27, pp. S97–S101, Nov. 2005, doi: 10.1016/j.braindev.2005.03.020.

[22] P. Moretti, ‘Learning and Memory and Synaptic Plasticity Are Impaired in a Mouse Model of Rett Syndrome’, *J. Neurosci.*, vol. 26, no. 1, pp. 319–327, Jan. 2006, doi: 10.1523/JNEUROSCI.2623-05.2006.

[23] R. H. Mount, T. Charman, R. P. Hastings, S. Reilly, and H. Cass, ‘The Rett Syndrome Behaviour Questionnaire (RSBQ): refining the behavioural phenotype of Rett syndrome’, *J. Child Psychol. Psychiatry*, vol. 43, no. 8, pp. 1099–1110, Nov. 2002, doi: 10.1111/1469-7610.00236.

[24] R. C. Samaco, C. Mandel-Brehm, C. M. McGraw, C. A. Shaw, B. E. McGill, and H. Y. Zoghbi, ‘Crh and Oprm1 mediate anxiety-related behavior and social approach in a mouse model of MECP2 duplication syndrome’, *Nat. Genet.*, vol. 44, no. 2, pp. 206–211, Feb. 2012, doi: 10.1038/ng.1066.

[25] L. L. Orefice, A. L. Zimmerman, A. M. Chirila, S. J. Sleboda, J. P. Head, and D. D. Ginty, ‘Peripheral Mechanosensory Neuron Dysfunction Underlies Tactile and Behavioral Deficits in Mouse Models of ASDs’, *Cell*, vol. 166, no. 2, pp. 299–313, Jul. 2016, doi: 10.1016/j.cell.2016.05.033.

[26] Y. Wu, W. Zhong, N. Cui, C. M. Johnson, H. Xing, S. Zhang, and C. Jiang, ‘Characterization of Rett Syndrome-like phenotypes in Mecp2-knockout rats’, *J. Neurodev. Disord.*, vol. 8, no. 1, p. 23, Dec. 2016, doi: 10.1186/s11689-016-9156-7.

[27] D. Goffin and Z. Zhou, ‘The neural circuit basis of Rett syndrome’, *Front. Biol. (Beijing).*, vol. 7, no. 5, pp. 428–435, Oct. 2012, doi: 10.1007/s11515-012-1248-5.

[28] C. M. Buchovecky, S. D. Turley, H. M. Brown, S. M. Kyle, J. G. McDonald, B. Liu, A. A. Pieper, W. Huang, D. M. Katz, D. W. Russell, J. Shendure, and M. J. Justice, ‘A suppressor screen in Mecp2 mutant mice implicates cholesterol metabolism in Rett syndrome’, *Nat. Genet.*, vol. 45, no. 9, pp. 1013–1020, Sep. 2013, doi: 10.1038/ng.2714.

[29] M. J. Justice, C. M. Buchovecky, S. M. Kyle, and A. Djukic, ‘A role for metabolism in Rett syndrome pathogenesis’, *Rare Dis.*, vol. 1, no. 1, p. e27265, Jan. 2013, doi: 10.4161/rdis.27265.

[30] M. Segatto, L. Trapani, I. Di Tunno, C. Sticozzi, G. Valacchi, J. Hayek, and V. Pallottini, ‘Cholesterol Metabolism Is Altered in Rett Syndrome: A Study on Plasma and Primary Cultured Fibroblasts Derived from Patients’, *PLoS One*, vol. 9, no. 8, p. e104834, Aug. 2014, doi: 10.1371/journal.pone.0104834.

[31] S. M. Kyle, N. Vashi, and M. J. Justice, ‘Rett syndrome: a neurological disorder with metabolic components’, *Open Biol.*, vol. 8, no. 2, p. 170216, Feb. 2018, doi: 10.1098/rsob.170216.

[32] N. Shulyakova, A. C. Andreazza, L. R. Mills, and J. H. Eubanks, ‘Mitochondrial Dysfunction in the Pathogenesis of Rett Syndrome: Implications for Mitochondria-Targeted Therapies’, *Front. Cell. Neurosci.*, vol. 11, Mar. 2017, doi: 10.3389/fncel.2017.00058.

[33] C. De Felice, L. Ciccoli, S. Leoncini, C. Signorini, M. Rossi, L. Vannuccini, G. Guazzi, G. Latini, M. Comporti, G. Valacchi, and J. Hayek, ‘Systemic oxidative stress in classic Rett syndrome’, *Free Radic. Biol. Med.*, vol. 47, no. 4, pp. 440–448, Aug. 2009, doi: 10.1016/j.freeradbiomed.2009.05.016.

[34] O. A. Janc, M. A. Hüser, K. Dietrich, B. Kempkes, C. Menzfeld, S. Hülsmann, and M. Müller, ‘Systemic Radical Scavenger Treatment of a Mouse Model of Rett Syndrome: Merits and Limitations of the Vitamin E Derivative Trolox’, *Front. Cell. Neurosci.*, vol. 10, Nov. 2016, doi: 10.3389/fncel.2016.00266.

[35] J.-M. Ramirez, C. S. Ward, and J. L. Neul, ‘Breathing challenges in Rett Syndrome: Lessons learned from humans and animal models’, *Respir. Physiol. Neurobiol.*, vol. 189, no. 2, pp. 280–287, Nov. 2013, doi:

10.1016/j.resp.2013.06.022.

[36] M. D. McCauley, T. Wang, E. Mike, J. Herrera, D. L. Beavers, T.-W. Huang, C. S. Ward, S. Skinner, A. K. Percy, D. G. Glaze, X. H. T. Wehrens, and J. L. Neul, 'Pathogenesis of Lethal Cardiac Arrhythmias in Mecp2 Mutant Mice: Implication for Therapy in Rett Syndrome', *Sci. Transl. Med.*, vol. 3, no. 113, Dec. 2011, doi: 10.1126/scitranslmed.3002982.

[37] M. Hara, T. Takahashi, C. Mitsumasu, S. Igata, M. Takano, T. Minami, H. Yasukawa, S. Okayama, K. Nakamura, Y. Okabe, E. Tanaka, G. Takemura, K. I. Kosai, Y. Yamashita, and T. Matsuishi, 'Disturbance of cardiac gene expression and cardiomyocyte structure predisposes Mecp2-null mice to arrhythmias', *Sci. Rep.*, vol. 5, no. November 2014, pp. 1–17, 2015, doi: 10.1038/srep11204.

[38] A. Anderson, K. Wong, P. Jacoby, J. Downs, and H. Leonard, 'Twenty years of surveillance in Rett syndrome: what does this tell us?', *Orphanet J. Rare Dis.*, vol. 9, no. 1, p. 87, Dec. 2014, doi: 10.1186/1750-1172-9-87.

[39] G. Wenk, 'Alterations in Dopaminergic Function in Rett Syndrome', *Neuropediatrics*, vol. 26, no. 02, pp. 123–125, Apr. 1995, doi: 10.1055/s-2007-979741.

[40] D. S. Paterson, E. G. Thompson, R. A. Belliveau, B. A. Antalffy, F. L. Trachtenberg, D. D. Armstrong, and H. C. Kinney, 'Serotonin Transporter Abnormality in the Dorsal Motor Nucleus of the Vagus in Rett Syndrome: Potential Implications for Clinical Autonomic Dysfunction', *J. Neuropathol. Exp. Neurol.*, vol. 64, no. 11, pp. 1018–1027, Nov. 2005, doi: 10.1097/01.jnen.0000187054.59018.f2.

[41] J.-C. Viemari, 'Mecp2 Deficiency Disrupts Norepinephrine and Respiratory Systems in Mice', *J. Neurosci.*, vol. 25, no. 50, pp. 11521–11530, Dec. 2005, doi: 10.1523/JNEUROSCI.4373-05.2005.

[42] H.-T. Chao, H. Chen, R. C. Samaco, M. Xue, M. Chahrour, J. Yoo, J. L. Neul, S. Gong, H.-C. Lu, N. Heintz, M. Ekker, J. L. R. Rubenstein, J. L. Noebels, C. Rosenmund, and H. Y. Zoghbi, 'Dysfunction in GABA signalling mediates autism-like stereotypies and Rett syndrome phenotypes', *Nature*, vol. 468, no. 7321, pp. 263–269, Nov. 2010, doi: 10.1038/nature09582.

[43] A. Patrizi, N. Picard, A. J. Simon, G. Gunner, E. Centofante, N. A. Andrews, and M. Fagiolini, 'Chronic Administration of the N-Methyl-D-Aspartate Receptor Antagonist Ketamine Improves Rett Syndrome Phenotype', *Biol. Psychiatry*, vol. 79, no. 9, pp. 755–764, May 2016, doi: 10.1016/j.biopsych.2015.08.018.

[44] Q. Chang, G. Khare, V. Dani, S. Nelson, and R. Jaenisch, 'The Disease Progression of Mecp2 Mutant Mice Is Affected by the Level of BDNF Expression', *Neuron*, vol. 49, no. 3, pp. 341–348, Feb. 2006, doi: 10.1016/j.neuron.2005.12.027.

[45] V. Deng, V. Matagne, F. Banine, M. Frerking, P. Ohliger, S. Budden, J. Pevsner, G. A. Dissen, L. S. Sherman, and S. R. Ojeda, 'FXYD1 is an MeCP2 target gene overexpressed in the brains of Rett syndrome patients and Mecp2 -null mice', *Hum. Mol. Genet.*, vol. 16, no. 6, pp. 640–650, Mar. 2007, doi: 10.1093/hmg/ddm007.

[46] R. Deogracias, M. Yazdani, M. P. J. Dekkers, J. Guy, M. C. S. Ionescu, K. E. Vogt, and Y.-A. Barde, 'Fingolimod, a sphingosine-1 phosphate receptor modulator, increases BDNF levels and improves symptoms of a mouse model of Rett syndrome', *Proc. Natl. Acad. Sci.*, vol. 109, no. 35, pp. 14230–14235, Aug. 2012, doi: 10.1073/pnas.1206093109.

[47] M. Itoh, S. Ide, S. Takashima, S. Kudo, Y. Nomura, M. Segawa, T. Kubota, H. Mori, S. Tanaka, H. Horie, Y. Tanabe, and Y. Goto, 'Methyl CpG-Binding Protein 2 (a Mutation of Which Causes Rett Syndrome) Directly Regulates Insulin-Like Growth Factor Binding Protein 3 in Mouse and Human Brains', *J. Neuropathol. Exp. Neurol.*, vol. 66, no. 2, pp. 117–123, Feb. 2007, doi: 10.1097/nen.0b013e3180302078.

[48] R. Artuso, F. T. Papa, E. Grillo, M. Mucciolo, D. H. Yasui, K. W. Dunaway, V. Disciglio, M. A. Mencarelli, M. Pollazzon, M. Zappella, G. Hayek, F. Mari, A. Renieri, J. M. LaSalle, and F. Ariani, 'Investigation of modifier genes within copy number variations in Rett syndrome', *J. Hum. Genet.*, vol. 56, no. 7, pp. 508–515, Jul. 2011, doi: 10.1038/jhg.2011.50.

[49] L. Pizzo *et al.*, 'Rare variants in the genetic background modulate cognitive and developmental phenotypes in individuals carrying disease-associated variants', *Genet. Med.*, vol. 21, no. 4, pp. 816–825, Apr. 2019, doi: 10.1038/s41436-018-0266-3.

[50] C. De Felice *et al.*, 'Oxidative brain damage in Mecp2-mutant murine models of Rett syndrome', *Neurobiol. Dis.*, vol. 68, pp. 66–77, Aug. 2014, doi: 10.1016/j.nbd.2014.04.006.

[51] H. Van Esch, M. Bauters, J. Ignatius, M. Jansen, M. Raynaud, K. Hollanders, D. Lugtenberg, T. Bienvenu,

L. R. Jensen, J. Gécz, C. Moraine, P. Marynen, J.-P. Fryns, and G. Froyen, ‘Duplication of the MECP2 Region Is a Frequent Cause of Severe Mental Retardation and Progressive Neurological Symptoms in Males’, *Am. J. Hum. Genet.*, vol. 77, no. 3, pp. 442–453, Sep. 2005, doi: 10.1086/444549.

[52] C. Philippeos, R. D. Hughes, A. Dhawan, and R. R. Mitry, ‘Introduction to Cell Culture’, in *Human Cell Culture Protocols*, 3rd ed.Humana Press, 2012, pp. 1–13. doi: 10.1007/978-1-61779-367-7_1.

[53] A. Khan, A. Menon, and J. Tongers, ‘Cell-Based Therapy in Ischemic Heart Disease’, in *Biochemical Basis and Therapeutic Implications of Angiogenesis*, Cham: Springer International Publishing, 2017, pp. 343–359. doi: 10.1007/978-3-319-61115-0_15.

[54] G. Rodrigues and B. A. J. Roelen, *Concepts and Applications of Stem Cell Biology*, 1st ed. in Learning Materials in Biosciences. Springer International Publishing, 2020, pp. 2–27. doi: 10.1007/978-3-030-43939-2.

[55] K. Takahashi, K. Tanabe, M. Ohnuki, M. Narita, T. Ichisaka, K. Tomoda, and S. Yamanaka, ‘Induction of Pluripotent Stem Cells from Adult Human Fibroblasts by Defined Factors’, *Cell*, vol. 131, no. 5, pp. 861–872, Nov. 2007, doi: 10.1016/j.cell.2007.11.019.

[56] A. Trounson and N. D. DeWitt, ‘Pluripotent stem cells progressing to the clinic’, *Nat. Rev. Mol. Cell Biol.*, vol. 17, no. 3, pp. 194–200, Mar. 2016, doi: 10.1038/nrm.2016.10.

[57] S. Yamanaka, ‘Pluripotent Stem Cell-Based Cell Therapy—Promise and Challenges’, *Cell Stem Cell*, vol. 27, no. 4, pp. 523–531, Oct. 2020, doi: 10.1016/j.stem.2020.09.014.

[58] M. C. N. Marchetto, C. Carromeu, A. Acab, D. Yu, G. W. Yeo, Y. Mu, G. Chen, F. H. Gage, and A. R. Muotri, ‘A Model for Neural Development and Treatment of Rett Syndrome Using Human Induced Pluripotent Stem Cells’, *Cell*, vol. 143, no. 4, pp. 527–539, Nov. 2010, doi: 10.1016/j.cell.2010.10.016.

[59] G. Ananiev, E. C. Williams, H. Li, and Q. Chang, ‘Isogenic Pairs of Wild Type and Mutant Induced Pluripotent Stem Cell (iPSC) Lines from Rett Syndrome Patients as In Vitro Disease Model’, *PLoS One*, vol. 6, no. 9, p. e25255, Sep. 2011, doi: 10.1371/journal.pone.0025255.

[60] K.-Y. Kim, E. Hysolli, and I.-H. Park, ‘Neuronal maturation defect in induced pluripotent stem cells from patients with Rett syndrome’, *Proc. Natl. Acad. Sci.*, vol. 108, no. 34, pp. 14169–14174, Aug. 2011, doi: 10.1073/pnas.1018979108.

[61] U. Djuric, A. Y. L. Cheung, W. Zhang, R. S. Mok, W. Lai, A. Piekna, J. A. Hendry, P. J. Ross, P. Pasceri, D.-S. Kim, M. W. Salter, and J. Ellis, ‘MECP2e1 isoform mutation affects the form and function of neurons derived from Rett syndrome patient iPS cells’, *Neurobiol. Dis.*, vol. 76, pp. 37–45, Apr. 2015, doi: 10.1016/j.nbd.2015.01.001.

[62] S. M. Chambers, C. A. Fasano, E. P. Papapetrou, M. Tomishima, M. Sadelain, and L. Studer, ‘Highly efficient neural conversion of human ES and iPS cells by dual inhibition of SMAD signaling’, *Nat. Biotechnol.*, vol. 27, no. 3, pp. 275–280, Mar. 2009, doi: 10.1038/nbt.1529.

[63] T. G. Fernandes, S. T. Duarte, M. Ghazvini, C. Gaspar, D. C. Santos, A. R. Porteira, G. M. C. Rodrigues, S. Haupt, D. M. Rombo, J. Armstrong, A. M. Sebastião, J. Gribnau, À. Garcia-Cazorla, O. Brüstle, D. Henrique, J. M. S. Cabral, and M. M. Diogo, ‘Neural commitment of human pluripotent stem cells under defined conditions recapitulates neural development and generates patient-specific neural cells’, *Biotechnol. J.*, vol. 10, no. 10, pp. 1578–1588, Oct. 2015, doi: 10.1002/biot.201400751.

[64] E. W. M. Chin, G. Marcy, S.-I. Yoon, D. Ma, F. J. Rosales, G. J. Augustine, and E. L. K. Goh, ‘Choline Ameliorates Disease Phenotypes in Human iPSC Models of Rett Syndrome’, *NeuroMolecular Med.*, vol. 18, no. 3, pp. 364–377, Sep. 2016, doi: 10.1007/s12017-016-8421-y.

[65] Q. Bu, A. Wang, H. Hamzah, A. Waldman, K. Jiang, Q. Dong, R. Li, J. Kim, D. Turner, and Q. Chang, ‘CREB Signaling Is Involved in Rett Syndrome Pathogenesis’, *J. Neurosci.*, vol. 37, no. 13, pp. 3671–3685, Mar. 2017, doi: 10.1523/JNEUROSCI.3735-16.2017.

[66] M. Yoo, C. Carromeu, O. Kwon, A. Muotri, and M. Schachner, ‘The L1 adhesion molecule normalizes neuritogenesis in Rett syndrome-derived neural precursor cells’, *Biochem. Biophys. Res. Commun.*, vol. 494, no. 3–4, pp. 504–510, Dec. 2017, doi: 10.1016/j.bbrc.2017.10.073.

[67] X. Tang, J. Kim, L. Zhou, E. Wengert, L. Zhang, Z. Wu, C. Carromeu, A. R. Muotri, M. C. N. Marchetto, F. H. Gage, and G. Chen, ‘KCC2 rescues functional deficits in human neurons derived from patients with Rett syndrome’, *Proc. Natl. Acad. Sci.*, vol. 113, no. 3, pp. 751–756, Jan. 2016, doi: 10.1073/pnas.1524013113.

[68] X. Tang, J. Drotar, K. Li, C. D. Clairmont, A. S. Brumm, A. J. Sullins, H. Wu, X. S. Liu, J. Wang, N. S. Gray, M. Sur, and R. Jaenisch, 'Pharmacological enhancement of KCC2 gene expression exerts therapeutic effects on human Rett syndrome neurons and Mecp2 mutant mice', *Sci. Transl. Med.*, vol. 11, no. 503, Jul. 2019, doi: 10.1126/scitranslmed.aau0164.

[69] M. Ohashi, E. Korsakova, D. Allen, P. Lee, K. Fu, B. S. Vargas, J. Cinkornpumin, C. Salas, J. C. Park, I. Germanguz, J. Langerman, C. Chronis, E. Kuoy, S. Tran, X. Xiao, M. Pellegrini, K. Plath, and W. E. Lowry, 'Loss of MECP2 Leads to Activation of P53 and Neuronal Senescence', *Stem Cell Reports*, vol. 10, no. 5, pp. 1453–1463, May 2018, doi: 10.1016/j.stemcr.2018.04.001.

[70] E. Landucci *et al.*, 'iPSC-derived neurons profiling reveals GABAergic circuit disruption and acetylated α-tubulin defect which improves after iHDAC6 treatment in Rett syndrome', *Exp. Cell Res.*, vol. 368, no. 2, pp. 225–235, Jul. 2018, doi: 10.1016/j.yexcr.2018.05.001.

[71] S. Varderidou-Minasian, L. Hinz, D. Hagemans, D. Posthuma, M. Altelaar, and V. M. Heine, 'Quantitative proteomic analysis of Rett iPSC-derived neuronal progenitors', *Mol. Autism*, vol. 11, no. 1, p. 38, Dec. 2020, doi: 10.1186/s13229-020-00344-3.

[72] P. Sharma, P. Mesci, C. Carromeu, D. R. McClatchy, L. Schiapparelli, J. R. Yates, A. R. Muotri, and H. T. Cline, 'Exosomes regulate neurogenesis and circuit assembly', *Proc. Natl. Acad. Sci.*, vol. 116, no. 32, pp. 16086–16094, Aug. 2019, doi: 10.1073/pnas.1902513116.

[73] Y. Xiang, Y. Tanaka, B. Patterson, S.-M. Hwang, E. Hysolli, B. Cakir, K.-Y. Kim, W. Wang, Y.-J. Kang, E. M. Clement, M. Zhong, S.-H. Lee, Y. S. Cho, P. Patra, G. J. Sullivan, S. M. Weissman, and I.-H. Park, 'Dysregulation of BRD4 Function Underlies the Functional Abnormalities of MeCP2 Mutant Neurons', *Mol. Cell*, vol. 79, no. 1, pp. 84-98.e9, Jul. 2020, doi: 10.1016/j.molcel.2020.05.016.

[74] Z.-N. Zhang, B. C. Freitas, H. Qian, J. Lux, A. Acab, C. A. Trujillo, R. H. Herai, V. A. Nguyen Huu, J. H. Wen, S. Joshi-Barr, J. V. Karpiak, A. J. Engler, X.-D. Fu, A. R. Muotri, and A. Almutairi, 'Layered hydrogels accelerate iPSC-derived neuronal maturation and reveal migration defects caused by MeCP2 dysfunction', *Proc. Natl. Acad. Sci.*, vol. 113, no. 12, pp. 3185–3190, Mar. 2016, doi: 10.1073/pnas.1521255113.

[75] A. T. Nguyen, S. Mattiassi, M. Loeblein, E. Chin, D. Ma, P. Coquet, V. Viasnoff, E. H. T. Teo, E. L. Goh, and E. K. F. Yim, 'Human Rett-derived neuronal progenitor cells in 3D graphene scaffold as an in vitro platform to study the effect of electrical stimulation on neuronal differentiation', *Biomed. Mater.*, vol. 13, no. 3, p. 034111, Mar. 2018, doi: 10.1088/1748-605X/aaaf2b.

[76] N. Mellios, D. A. Feldman, S. D. Sheridan, J. P. K. Ip, S. Kwok, S. K. Amoah, B. Rosen, B. A. Rodriguez, B. Crawford, R. Swaminathan, S. Chou, Y. Li, M. Ziats, C. Ernst, R. Jaenisch, S. J. Haggarty, and M. Sur, 'MeCP2-regulated miRNAs control early human neurogenesis through differential effects on ERK and AKT signaling', *Mol. Psychiatry*, vol. 23, no. 4, pp. 1051–1065, Apr. 2018, doi: 10.1038/mp.2017.86.

[77] H. Nakashima, K. Tsujimura, K. Irie, T. Imamura, C. A. Trujillo, M. Ishizu, M. Uesaka, M. Pan, H. Noguchi, K. Okada, K. Aoyagi, T. Andoh-Noda, H. Okano, A. R. Muotri, and K. Nakashima, 'MeCP2 controls neural stem cell fate specification through miR-199a-mediated inhibition of BMP-Smad signaling', *Cell Rep.*, vol. 35, no. 7, p. 109124, May 2021, doi: 10.1016/j.celrep.2021.109124.

[78] A. R. Gomes, T. G. Fernandes, S. H. Vaz, T. P. Silva, E. P. Bekman, S. Xapelli, S. Duarte, M. Ghazvini, J. Gribnau, A. R. Muotri, C. A. Trujillo, A. M. Sebastião, J. M. S. Cabral, and M. M. Diogo, 'Modeling Rett Syndrome With Human Patient-Specific Forebrain Organoids', *Front. Cell Dev. Biol.*, vol. 8, Dec. 2020, doi: 10.3389/fcell.2020.610427.

[79] N. Madan, M. Levine, K. Pourmoghadam, and M. Sokoloski, 'Severe Sinus Bradycardia in a Patient with Rett Syndrome: A New Cause for a Pause?', *Pediatr. Cardiol.*, vol. 25, no. 1, pp. 53–55, Feb. 2004, doi: 10.1007/s00246-003-0341-6.

[80] E. A. Sekul, J. P. Moak, R. J. Schultz, D. G. Glaze, J. K. Dunn, and A. K. Percy, 'Electrocardiographic findings in Rett syndrome: An explanation for sudden death?', *J. Pediatr.*, vol. 125, no. 1, pp. 80–82, Jul. 1994, doi: 10.1016/S0022-3476(94)70128-8.

[81] M. Fuster-Siebert and M. Castro-Gago, 'Electrocardiographic findings in Rett syndrome', *J. Pediatr.*, vol. 126, no. 3, p. 506, Mar. 1995, doi: 10.1016/S0022-3476(95)70490-6.

[82] F. Guideri, M. Acampa, C. Hayek, M. Zappella, and T. Di Perri, 'Reduced Heart Rate Variability in Patients Affected with Rett Syndrome. A Possible Explanation for Sudden Death', *Neuropediatrics*, vol. 30, no. 03, pp. 146–148, Jun. 1999, doi: 10.1055/s-2007-973480.

[83] F. Guideri, M. Acampa, T. DiPerri, M. Zappella, and Y. Hayek, ‘Progressive Cardiac Dysautonomia Observed in Patients Affected by Classic Rett Syndrome and Not in the Preserved Speech Variant’, *J. Child Neurol.*, vol. 16, no. 5, pp. 370–373, May 2001, doi: 10.1177/088307380101600512.

[84] F. Guideri and M. Acampa, ‘Sudden Death and Cardiac Arrhythmias in Rett Syndrome’, *Pediatr. Cardiol.*, vol. 26, no. 1, pp. 111–111, Feb. 2005, doi: 10.1007/s00246-004-0701-x.

[85] C. J. Ellaway, G. Sholler, H. Leonard, and J. Christodoulou, ‘Prolonged QT interval in Rett syndrome’, *Arch. Dis. Child.*, vol. 80, no. 5, pp. 470–472, May 1999, doi: 10.1136/adc.80.5.470.

[86] A. Kumar, A. Jaryal, S. Gulati, B. Chakrabarty, A. Singh, K. K. Deepak, R. M. Pandey, N. Gupta, S. Sapra, M. Kabra, and R. Khajuria, ‘Cardiovascular Autonomic Dysfunction in Children and Adolescents With Rett Syndrome’, *Pediatr. Neurol.*, vol. 70, pp. 61–66, May 2017, doi: 10.1016/j.pediatrneurol.2017.01.010.

[87] C. De Felice, S. Maffei, C. Signorini, S. Leoncini, S. Lunghetti, G. Valacchi, M. D’Esposito, S. Filosa, F. Della Ragione, G. Butera, R. Favilli, L. Ciccoli, and J. Hayek, ‘Subclinical myocardial dysfunction in Rett syndrome’, *Eur. Hear. J. - Cardiovasc. Imaging*, vol. 13, no. 4, pp. 339–345, Apr. 2012, doi: 10.1093/ejechocard/jer256.

[88] A. M. Kerr, D. D. Armstrong, R. J. Prescott, D. Doyle, and D. L. Kearney, ‘Rett syndrome: analysis of deaths in the British survey.’, *Eur. Child Adolesc. Psychiatry*, vol. 6 Suppl 1, pp. 71–4, 1997, [Online]. Available: http://www.ncbi.nlm.nih.gov/pubmed/9452925

[89] J. Crosson, S. Srivastava, G. M. Bibat, S. Gupta, A. Kantipuly, C. Smith-Hicks, S. M. Myers, A. Sanyal, G. Yenokyan, J. Brenner, and S. R. Naidu, ‘Evaluation of QTc in Rett syndrome: Correlation with age, severity, and genotype’, *Am. J. Med. Genet. Part A*, vol. 173, no. 6, pp. 1495–1501, Jun. 2017, doi: 10.1002/ajmg.a.38191.

[90] B. C. Clark, A. Kopp, W. Morey, and A. Djukic, ‘Serial follow-up of corrected QT interval in Rett syndrome’, *Dev. Med. Child Neurol.*, vol. 62, no. 7, pp. 833–836, Jul. 2020, doi: 10.1111/dmcn.14419.

[91] ‘Dysautonomia - National Institute of Neurological Disorders and Stroke’. https://www.ninds.nih.gov/Disorders/All-Disorders/Dysautonomia-Information-Page (accessed Sep. 16, 2022).

[92] A. M. Goldman, E. Glasscock, J. Yoo, T. T. Chen, T. L. Klassen, and J. L. Noebels, ‘Arrhythmia in Heart and Brain: KCNQ1 Mutations Link Epilepsy and Sudden Unexplained Death’, *Sci. Transl. Med.*, vol. 1, no. 2, Oct. 2009, doi: 10.1126/scitranslmed.3000289.

[93] S. Mucerino, A. Di Salle, N. Alessio, S. Margarucci, R. Nicolai, M. A. B. Melone, U. Galderisi, and G. Peluso, ‘Alterations in the carnitine cycle in a mouse model of Rett syndrome’, *Sci. Rep.*, vol. 7, no. 1, p. 41824, Mar. 2017, doi: 10.1038/srep41824.

[94] J. A. Herrera, C. S. Ward, M. R. Pitcher, A. K. Percy, S. Skinner, W. E. Kaufmann, D. G. Glaze, X. H. T. Wehrens, and J. L. Neul, ‘Treatment of cardiac arrhythmias in Rett Syndrome with sodium channel blocking antiepileptic drugs’, *Dis. Model. Mech.*, Jan. 2015, doi: 10.1242/dmm.020131.

[95] C. S. Ward, E. M. Arvide, T.-W. Huang, J. Yoo, J. L. Noebels, and J. L. Neul, ‘MeCP2 Is Critical within HoxB1-Derived Tissues of Mice for Normal Lifespan’, *J. Neurosci.*, vol. 31, no. 28, pp. 10359–10370, Jul. 2011, doi: 10.1523/JNEUROSCI.0057-11.2011.

[96] D. M. Katz, M. Dutschmann, J.-M. Ramirez, and G. Hilaire, ‘Breathing disorders in Rett syndrome: Progressive neurochemical dysfunction in the respiratory network after birth’, *Respir. Physiol. Neurobiol.*, vol. 168, no. 1–2, pp. 101–108, Aug. 2009, doi: 10.1016/j.resp.2009.04.017.

[97] M. F. Oginsky, N. Cui, W. Zhong, C. M. Johnson, and C. Jiang, ‘Alterations in the cholinergic system of brain stem neurons in a mouse model of Rett syndrome’, *Am. J. Physiol. Physiol.*, vol. 307, no. 6, pp. C508–C520, Sep. 2014, doi: 10.1152/ajpcell.00035.2014.

[98] E. Großer, U. Hirt, O. A. Janc, C. Menzfeld, M. Fischer, B. Kempkes, S. Vogelgesang, T. U. Manzke, L. Opitz, G. Salinas-Riester, and M. Müller, ‘Oxidative burden and mitochondrial dysfunction in a mouse model of Rett syndrome’, *Neurobiol. Dis.*, vol. 48, no. 1, pp. 102–114, Oct. 2012, doi: 10.1016/j.nbd.2012.06.007.

[99] H. Cheng, I. Charles, A. F. James, A. P. Abdala, and J. C. Hancox, ‘QTc interval and ventricular action potential prolongation in the Mecp2Null/+ murine model of Rett syndrome’, *Physiol. Rep.*, vol. 10, no. 19, Oct. 2022, doi: 10.14814/phy2.15437.

[100] H. Cheng, I. Charles, A. F. James, A. P. Abdala, and J. C. Hancox, 'Delayed Ventricular Repolarization and Sodium Channel Current Modification in a Mouse Model of Rett Syndrome', *Int. J. Mol. Sci.*, vol. 23, no. 10, p. 5735, May 2022, doi: 10.3390/ijms23105735.

[101] H. Morita, J. Wu, and D. P. Zipes, 'The QT syndromes: long and short', *Lancet*, vol. 372, no. 9640, pp. 750–763, Aug. 2008, doi: 10.1016/S0140-6736(08)61307-0.

[102] L. M. Hondeghem, L. Carlsson, and G. Duker, 'Instability and Triangulation of the Action Potential Predict Serious Proarrhythmia, but Action Potential Duration Prolongation Is Antiarrhythmic', *Circulation*, vol. 103, no. 15, pp. 2004–2013, Apr. 2001, doi: 10.1161/01.CIR.103.15.2004.

[103] L. M. HONDEGHEM, 'Relative Contributions of TRIaD and QT to Proarrhythmia', *J. Cardiovasc. Electrophysiol.*, vol. 18, no. 6, pp. 655–657, Jun. 2007, doi: 10.1111/j.1540-8167.2007.00827.x.

[104] J. A. Herrera, C. S. Ward, X. H. T. Wehrens, and J. L. Neul, 'Methyl-CpG binding-protein 2 function in cholinergic neurons mediates cardiac arrhythmogenesis', *Hum. Mol. Genet.*, p. ddw326, Oct. 2016, doi: 10.1093/hmg/ddw326.

[105] I. Splawski, K. W. Timothy, L. M. Sharpe, N. Decher, P. Kumar, R. Bloise, C. Napolitano, P. J. Schwartz, R. M. Joseph, K. Condouris, H. Tager-Flusberg, S. G. Priori, M. C. Sanguinetti, and M. T. Keating, 'CaV1.2 Calcium Channel Dysfunction Causes a Multisystem Disorder Including Arrhythmia and Autism', *Cell*, vol. 119, no. 1, pp. 19–31, Oct. 2004, doi: 10.1016/j.cell.2004.09.011.

[106] M. Yazawa, B. Hsueh, X. Jia, A. M. Pasca, J. A. Bernstein, J. Hallmayer, and R. E. Dolmetsch, 'Using induced pluripotent stem cells to investigate cardiac phenotypes in Timothy syndrome', *Nature*, vol. 471, no. 7337, pp. 230–234, Mar. 2011, doi: 10.1038/nature09855.

[107] V. Yarotskyy, G. Gao, L. Du, S. B. Ganapathi, B. Z. Peterson, and K. S. Elmslie, 'Roscovitine Binds to Novel L-channel (CaV1.2) Sites That Separately Affect Activation and Inactivation', *J. Biol. Chem.*, vol. 285, no. 1, pp. 43–53, Jan. 2010, doi: 10.1074/jbc.M109.076448.

[108] L. Song, S. E. Park, Y. Isseroff, K. Morikawa, and M. Yazawa, 'Inhibition of CDK5 Alleviates the Cardiac Phenotypes in Timothy Syndrome', *Stem Cell Reports*, vol. 9, no. 1, pp. 50–57, Jul. 2017, doi: 10.1016/j.stemcr.2017.05.028.

[109] K. L. Moore, T. V. N. Persaud, and M. G. Torchia, *The Developing Human*, 10th ed. Elsevier, 2016, pp. 51–52; 283–335; 414.

[110] M. F. J. Buijtendijk, P. Barnett, and M. J. B. Hoff, 'Development of the human heart', *Am. J. Med. Genet. Part C Semin. Med. Genet.*, vol. 184, no. 1, pp. 7–22, Mar. 2020, doi: 10.1002/ajmg.c.31778.

[111] M. Sylva, M. J. B. van den Hoff, and A. F. M. Moorman, 'Development of the human heart', *Am. J. Med. Genet. Part A*, vol. 164, no. 6, pp. 1347–1371, Jun. 2014, doi: 10.1002/ajmg.a.35896.

[112] C. M. J. Tan and A. J. Lewandowski, 'The Transitional Heart: From Early Embryonic and Fetal Development to Neonatal Life', *Fetal Diagn. Ther.*, vol. 47, no. 5, pp. 373–386, 2020, doi: 10.1159/000501906.

[113] T. W. Sadler, *Langman's Medical Embryology*, 12th ed. Lippincott Williams & Wilkins, 2012, pp. 70–77; 162–200.

[114] E. Tzahor, 'Wnt/β-Catenin Signaling and Cardiogenesis: Timing Does Matter', *Dev. Cell*, vol. 13, no. 1, pp. 10–13, Jul. 2007, doi: 10.1016/j.devcel.2007.06.006.

[115] L. Tirosh-Finkel, A. Zeisel, M. Brodt-Ivenshitz, A. Shamai, Z. Yao, R. Seger, E. Domany, and E. Tzahor, 'BMP-mediated inhibition of FGF signaling promotes cardiomyocyte differentiation of anterior heart field progenitors', *Development*, vol. 137, no. 18, pp. 2989–3000, Sep. 2010, doi: 10.1242/dev.051649.

[116] M. R. Hutson, X. L. Zeng, A. J. Kim, E. Antoon, S. Harward, and M. L. Kirby, 'Arterial pole progenitors interpret opposing FGF/BMP signals to proliferate or differentiate', *Development*, vol. 137, no. 18, pp. 3001–3011, Sep. 2010, doi: 10.1242/dev.051565.

[117] L. A. Dyer and M. L. Kirby, 'Sonic hedgehog maintains proliferation in secondary heart field progenitors and is required for normal arterial pole formation', *Dev. Biol.*, vol. 330, no. 2, pp. 305–317, Jun. 2009, doi: 10.1016/j.ydbio.2009.03.028.

[118] C.-L. Cai, X. Liang, Y. Shi, P.-H. Chu, S. L. Pfaff, J. Chen, and S. Evans, 'Isl1 Identifies a Cardiac Progenitor Population that Proliferates Prior to Differentiation and Contributes a Majority of Cells to the Heart', *Dev. Cell*, vol. 5, no. 6, pp. 877–889, Dec. 2003, doi: 10.1016/S1534-5807(03)00363-0.

[119] S. M. Meilhac and M. E. Buckingham, ‘The deployment of cell lineages that form the mammalian heart’, *Nat. Rev. Cardiol.*, vol. 15, no. 11, pp. 705–724, Nov. 2018, doi: 10.1038/s41569-018-0086-9.

[120] D. Später, E. M. Hansson, L. Zangi, and K. R. Chien, ‘How to make a cardiomyocyte’, *Development*, vol. 141, no. 23, pp. 4418–4431, Dec. 2014, doi: 10.1242/dev.091538.

[121] D. Shier, J. Butler, and R. Lewis, ‘Cardiovascular System’, in *Hole’s Essentials Of Human Anatomy & Physiology*, 11th ed.McGraw-Hill, 2012, pp. 340–376.

[122] M. A. Branco, J. M. S. Cabral, and M. M. Diogo, ‘From Human Pluripotent Stem Cells to 3D Cardiac Microtissues: Progress, Applications and Challenges’, *Bioengineering*, vol. 7, no. 3, p. 92, Aug. 2020, doi: 10.3390/bioengineering7030092.

[123] E. P. Widmaier, H. Raff, and K. T. Strang, ‘The heart’, in *Vander’s Human Physiology*, 11th ed.McGraw-Hill, 2008, pp. 365–384.

[124] M. Litviňuková *et al.*, ‘Cells of the adult human heart’, *Nature*, vol. 588, no. 7838, pp. 466–472, Dec. 2020, doi: 10.1038/s41586-020-2797-4.

[125] Y. Cui, Y. Zheng, X. Liu, L. Yan, X. Fan, J. Yong, Y. Hu, J. Dong, Q. Li, X. Wu, S. Gao, J. Li, L. Wen, J. Qiao, and F. Tang, ‘Single-Cell Transcriptome Analysis Maps the Developmental Track of the Human Heart’, *Cell Rep.*, vol. 26, no. 7, pp. 1934-1950.e5, Feb. 2019, doi: 10.1016/j.celrep.2019.01.079.

[126] A. R. Pinto, A. Ilinykh, M. J. Ivey, J. T. Kuwabara, M. L. D’Antoni, R. Debuque, A. Chandran, L. Wang, K. Arora, N. A. Rosenthal, and M. D. Tallquist, ‘Revisiting Cardiac Cellular Composition’, *Circ. Res.*, vol. 118, no. 3, pp. 400–409, Feb. 2016, doi: 10.1161/CIRCRESAHA.115.307778.

[127] J.-Q. He, Y. Ma, Y. Lee, J. A. Thomson, and T. J. Kamp, ‘Human Embryonic Stem Cells Develop Into Multiple Types of Cardiac Myocytes’, *Circ. Res.*, vol. 93, no. 1, pp. 32–39, Jul. 2003, doi: 10.1161/01.RES.0000080317.92718.99.

[128] J. Zhang, G. F. Wilson, A. G. Soerens, C. H. Koonce, J. Yu, S. P. Palecek, J. A. Thomson, and T. J. Kamp, ‘Functional Cardiomyocytes Derived From Human Induced Pluripotent Stem Cells’, *Circ. Res.*, vol. 104, no. 4, Feb. 2009, doi: 10.1161/CIRCRESAHA.108.192237.

[129] K. Oiwa, K. Shimba, T. Numata, A. Takeuchi, K. Kotani, and Y. Jimbo, ‘A device for co-culturing autonomic neurons and cardiomyocytes using micro-fabrication techniques’, *Integr. Biol.*, vol. 8, no. 3, pp. 341–348, 2016, doi: 10.1039/C5IB00273G.

[130] M. L. Kirby, ‘Innervation of the Developing Heart’, in *Cardiac Development*, 1st ed.Oxford University Press, 2007, pp. 179–197.

[131] W. Hasan, ‘Autonomic cardiac innervation’, *Organogenesis*, vol. 9, no. 3, pp. 176–193, Jul. 2013, doi: 10.4161/org.24892.

[132] H. M. Young, R. B. Anderson, and C. R. Anderson, ‘Guidance cues involved in the development of the peripheral autonomic nervous system’, *Auton. Neurosci.*, vol. 112, no. 1–2, pp. 1–14, May 2004, doi: 10.1016/j.autneu.2004.02.008.

[133] Y. Morikawa, A. Zehir, E. Maska, C. Deng, M. D. Schneider, Y. Mishina, and P. Cserjesi, ‘BMP signaling regulates sympathetic nervous system development through Smad4-dependent and -independent pathways’, *Development*, vol. 136, no. 21, pp. 3575–3584, Nov. 2009, doi: 10.1242/dev.038133.

[134] R. Kuruvilla, L. S. Zweifel, N. O. Glebova, B. E. Lonze, G. Valdez, H. Ye, and D. D. Ginty, ‘A Neurotrophin Signaling Cascade Coordinates Sympathetic Neuron Development through Differential Control of TrkA Trafficking and Retrograde Signaling’, *Cell*, vol. 118, no. 2, pp. 243–255, Jul. 2004, doi: 10.1016/j.cell.2004.06.021.

[135] T. Makita, H. M. Sucov, C. E. Gariepy, M. Yanagisawa, and D. D. Ginty, ‘Endothelins are vascular-derived axonal guidance cues for developing sympathetic neurons’, *Nature*, vol. 452, no. 7188, pp. 759–763, Apr. 2008, doi: 10.1038/nature06859.

[136] S. T. Lockhart, G. G. Turrigiano, and S. J. Birren, ‘Nerve Growth Factor Modulates Synaptic Transmission between Sympathetic Neurons and Cardiac Myocytes’, *J. Neurosci.*, vol. 17, no. 24, pp. 9573–9582, Dec. 1997, doi: 10.1523/JNEUROSCI.17-24-09573.1997.

[137] R. Heumann, S. Korsching, J. Scott, and H. Thoenen, ‘Relationship between levels of nerve growth factor (NGF) and its messenger RNA in sympathetic ganglia and peripheral target tissues.’, *EMBO J.*, vol. 3, no. 13, pp. 3183–3189, Dec. 1984, doi: 10.1002/j.1460-2075.1984.tb02277.x.

[138] M. Ieda, K. Fukuda, Y. Hisaka, K. Kimura, H. Kawaguchi, J. Fujita, K. Shimoda, E. Takeshita, H. Okano, Y. Kurihara, H. Kurihara, J. Ishida, A. Fukamizu, H. J. Federoff, and S. Ogawa, 'Endothelin-1 regulates cardiac sympathetic innervation in the rodent heart by controlling nerve growth factor expression', *J. Clin. Invest.*, vol. 113, no. 6, pp. 876–884, Mar. 2004, doi: 10.1172/JCI19480.

[139] V. Hildreth, R. H. Anderson, and D. J. Henderson, 'Autonomic innervation of the developing heart: Origins and function', *Clin. Anat.*, vol. 22, no. 1, pp. 36–46, Jan. 2009, doi: 10.1002/ca.20695.

[140] M. L. Kirby and M. R. Hutson, 'Factors controlling cardiac neural crest cell migration', *Cell Adh. Migr.*, vol. 4, no. 4, pp. 609–621, Oct. 2010, doi: 10.4161/cam.4.4.13489.

[141] F. Müller and H. Rohrer, 'Molecular control of ciliary neuron development: BMPs and downstream transcriptional control in the parasympathetic lineage', *Development*, vol. 129, no. 24, pp. 5707–5717, Dec. 2002, doi: 10.1242/dev.00165.

[142] M. A. Branco, T. P. Dias, J. P. Cotovio, C. A. V. Rodrigues, T. G. Fernandes, J. M. S. Cabral, and M. M. Diogo, '3D Microwell Platform for Cardiomyocyte Differentiation of Human Pluripotent Stem Cells', in *Induced Pluripotent Stem (iPS) Cells: Methods and Protocols*, Humana, New York, NY, 2020, pp. 127–143. doi: 10.1007/7651_2020_336.

[143] X. Lian, C. Hsiao, G. Wilson, K. Zhu, L. B. Hazeltine, S. M. Azarin, K. K. Raval, J. Zhang, T. J. Kamp, and S. P. Palecek, 'Robust cardiomyocyte differentiation from human pluripotent stem cells via temporal modulation of canonical Wnt signaling', *Proc. Natl. Acad. Sci.*, vol. 109, no. 27, Jul. 2012, doi: 10.1073/pnas.1200250109.

[144] P. W. Burridge, G. Keller, J. D. Gold, and J. C. Wu, 'Production of De Novo Cardiomyocytes: Human Pluripotent Stem Cell Differentiation and Direct Reprogramming', *Cell Stem Cell*, vol. 10, no. 1, pp. 16–28, Jan. 2012, doi: 10.1016/j.stem.2011.12.013.

[145] P. W. Burridge, A. Sharma, and J. C. Wu, 'Genetic and Epigenetic Regulation of Human Cardiac Reprogramming and Differentiation in Regenerative Medicine', *Annu. Rev. Genet.*, vol. 49, no. 1, pp. 461–484, Nov. 2015, doi: 10.1146/annurev-genet-112414-054911.

[146] C. L. Mummery, J. Zhang, E. S. Ng, D. A. Elliott, A. G. Elefanty, and T. J. Kamp, 'Differentiation of Human Embryonic Stem Cells and Induced Pluripotent Stem Cells to Cardiomyocytes', *Circ. Res.*, vol. 111, no. 3, pp. 344–358, Jul. 2012, doi: 10.1161/CIRCRESAHA.110.227512.

[147] C. L. Bauwens, H. Song, N. Thavandiran, M. Ungrin, S. Massé, K. Nanthakumar, C. Seguin, and P. W. Zandstra, 'Geometric Control of Cardiomyogenic Induction in Human Pluripotent Stem Cells', *Tissue Eng. Part A*, vol. 17, no. 15–16, pp. 1901–1909, Aug. 2011, doi: 10.1089/ten.tea.2010.0563.

[148] J. Dahlmann, G. Kensah, H. Kempf, D. Skvorc, A. Gawol, D. A. Elliott, G. Dräger, R. Zweigerdt, U. Martin, and I. Gruh, 'The use of agarose microwells for scalable embryoid body formation and cardiac differentiation of human and murine pluripotent stem cells', *Biomaterials*, vol. 34, no. 10, pp. 2463–2471, Mar. 2013, doi: 10.1016/j.biomaterials.2012.12.024.

[149] M. A. Branco, J. P. Cotovio, C. A. V. Rodrigues, S. H. Vaz, T. G. Fernandes, L. M. Moreira, J. M. S. Cabral, and M. M. Diogo, 'Transcriptomic analysis of 3D Cardiac Differentiation of Human Induced Pluripotent Stem Cells Reveals Faster Cardiomyocyte Maturation Compared to 2D Culture', *Sci. Rep.*, vol. 9, no. 1, p. 9229, Dec. 2019, doi: 10.1038/s41598-019-45047-9.

[150] V. C. Chen, J. Ye, P. Shukla, G. Hua, D. Chen, Z. Lin, J. Liu, J. Chai, J. Gold, J. Wu, D. Hsu, and L. A. Couture, 'Development of a scalable suspension culture for cardiac differentiation from human pluripotent stem cells', *Stem Cell Res.*, vol. 15, no. 2, pp. 365–375, Sep. 2015, doi: 10.1016/j.scr.2015.08.002.

[151] C. Halloin *et al.*, 'Continuous WNT Control Enables Advanced hPSC Cardiac Processing and Prognostic Surface Marker Identification in Chemically Defined Suspension Culture', *Stem Cell Reports*, vol. 13, no. 2, pp. 366–379, Aug. 2019, doi: 10.1016/j.stemcr.2019.06.004.

[152] H. Fonoudi *et al.*, 'A Universal and Robust Integrated Platform for the Scalable Production of Human Cardiomyocytes From Pluripotent Stem Cells', *Stem Cells Transl. Med.*, vol. 4, no. 12, pp. 1482–1494, Dec. 2015, doi: 10.5966/sctm.2014-0275.

[153] M. Zhang, J. S. Schulte, A. Heinick, I. Piccini, J. Rao, R. Quaranta, D. Zeuschner, D. Malan, K.-P. Kim, A. Röpke, P. Sasse, M. Araúzo-Bravo, G. Seebohm, H. Schöler, L. Fabritz, P. Kirchhof, F. U. Müller, and B. Greber, 'Universal Cardiac Induction of Human Pluripotent Stem Cells in Two and Three-Dimensional Formats: Implications for In Vitro Maturation', *Stem Cells*, vol. 33, no. 5, pp. 1456–1469, May 2015, doi: 10.1002/stem.1964.

[154] K. Andrysiak, J. Stępniewski, and J. Dulak, 'Human-induced pluripotent stem cell-derived cardiomyocytes, 3D cardiac structures, and heart-on-a-chip as tools for drug research', *Pflügers Arch. - Eur. J. Physiol.*, vol. 473, no. 7, pp. 1061–1085, Jul. 2021, doi: 10.1007/s00424-021-02536-z.

[155] A. Khanna, M. Zamani, and N. F. Huang, 'Extracellular Matrix-Based Biomaterials for Cardiovascular Tissue Engineering', *J. Cardiovasc. Dev. Dis.*, vol. 8, no. 11, p. 137, Oct. 2021, doi: 10.3390/jcdd8110137.

[156] Y. Guo and W. T. Pu, 'Cardiomyocyte Maturation', *Circ. Res.*, vol. 126, no. 8, pp. 1086–1106, Apr. 2020, doi: 10.1161/CIRCRESAHA.119.315862.

[157] X. Yang, M. Rodriguez, L. Pabon, K. A. Fischer, H. Reinecke, M. Regnier, N. J. Sniadecki, H. Ruohola-Baker, and C. E. Murry, 'Tri-iodo-l-thyronine promotes the maturation of human cardiomyocytes-derived from induced pluripotent stem cells', *J. Mol. Cell. Cardiol.*, vol. 72, pp. 296–304, Jul. 2014, doi: 10.1016/j.yjmcc.2014.04.005.

[158] D. S. Lee, J.-H. Chen, D. J. Lundy, C.-H. Liu, S.-M. Hwang, L. Pabon, R.-C. Shieh, C.-C. Chen, S.-N. Wu, Y.-T. Yan, S.-T. Lee, P.-M. Chiang, S. Chien, C. E. Murry, and P. C. H. Hsieh, 'Defined MicroRNAs Induce Aspects of Maturation in Mouse and Human Embryonic-Stem-Cell-Derived Cardiomyocytes', *Cell Rep.*, vol. 12, no. 12, pp. 1960–1967, Sep. 2015, doi: 10.1016/j.celrep.2015.08.042.

[159] C. Y. Huang, R. Peres Moreno Maia-Joca, C. S. Ong, I. Wilson, D. DiSilvestre, G. F. Tomaselli, and D. H. Reich, 'Enhancement of human iPSC-derived cardiomyocyte maturation by chemical conditioning in a 3D environment', *J. Mol. Cell. Cardiol.*, vol. 138, pp. 1–11, Jan. 2020, doi: 10.1016/j.yjmcc.2019.10.001.

[160] A. Skorska, L. Johann, O. Chabanovska, P. Vasudevan, S. Kussauer, M. Hillemanns, M. Wolfien, A. Jonitz-Heincke, O. Wolkenhauer, R. Bader, H. Lang, R. David, and H. Lemcke, 'Monitoring the maturation of the sarcomere network: a super-resolution microscopy-based approach', *Cell. Mol. Life Sci.*, vol. 79, no. 3, p. 149, Mar. 2022, doi: 10.1007/s00018-022-04196-3.

[161] D. A. M. Feyen *et al.*, 'Metabolic Maturation Media Improve Physiological Function of Human iPSC-Derived Cardiomyocytes', *Cell Rep.*, vol. 32, no. 3, p. 107925, Jul. 2020, doi: 10.1016/j.celrep.2020.107925.

[162] O. J. Abilez *et al.*, 'Passive Stretch Induces Structural and Functional Maturation of Engineered Heart Muscle as Predicted by Computational Modeling', *Stem Cells*, vol. 36, no. 2, pp. 265–277, Feb. 2018, doi: 10.1002/stem.2732.

[163] S. M. Ravenscroft, A. Pointon, A. W. Williams, M. J. Cross, and J. E. Sidaway, 'Cardiac Non-myocyte Cells Show Enhanced Pharmacological Function Suggestive of Contractile Maturity in Stem Cell Derived Cardiomyocyte Microtissues', *Toxicol. Sci.*, vol. 152, no. 1, pp. 99–112, Jul. 2016, doi: 10.1093/toxsci/kfw069.

[164] A. C. Silva, O. B. Matthys, D. A. Joy, M. A. Kauss, V. Natarajan, M. H. Lai, D. Turaga, A. P. Blair, M. Alexanian, B. G. Bruneau, and T. C. McDevitt, 'Co-emergence of cardiac and gut tissues promotes cardiomyocyte maturation within human iPSC-derived organoids', *Cell Stem Cell*, vol. 28, no. 12, pp. 2137-2152.e6, Dec. 2021, doi: 10.1016/j.stem.2021.11.007.

[165] K. Ronaldson-Bouchard, S. P. Ma, K. Yeager, T. Chen, L. Song, D. Sirabella, K. Morikawa, D. Teles, M. Yazawa, and G. Vunjak-Novakovic, 'Advanced maturation of human cardiac tissue grown from pluripotent stem cells', *Nature*, vol. 556, no. 7700, pp. 239–243, Apr. 2018, doi: 10.1038/s41586-018-0016-3.

[166] M. A. Branco, T. P. Dias, J. M. S. Cabral, P. Pinto-do-Ó, and M. M. Diogo, 'Human multilineage pro-epicardium/foregut organoids support the development of an epicardium/myocardium organoid', *Nat. Commun.*, vol. 13, no. 1, p. 6981, Nov. 2022, doi: 10.1038/s41467-022-34730-7.

[167] K. Saito-Diaz, H. F. Wu, and N. Zeltner, 'Autonomic Neurons with Sympathetic Character Derived From Human Pluripotent Stem Cells', *Curr. Protoc. Stem Cell Biol.*, vol. 49, no. 1, p. e78, Jun. 2019, doi: 10.1002/cpsc.78.

[168] Y. Oh, G.-S. Cho, Z. Li, I. Hong, R. Zhu, M.-J. Kim, Y. J. Kim, E. Tampakakis, L. Tung, R. Huganir, X. Dong, C. Kwon, and G. Lee, 'Functional Coupling with Cardiac Muscle Promotes Maturation of hPSC-Derived Sympathetic Neurons', *Cell Stem Cell*, vol. 19, no. 1, pp. 95–106, Jul. 2016, doi: 10.1016/j.stem.2016.05.002.

[169] T. J. R. Frith and A. Tsakiridis, 'Efficient Generation of Trunk Neural Crest and Sympathetic Neurons from Human Pluripotent Stem Cells Via a Neuromesodermal Axial Progenitor Intermediate', *Curr.*

Protoc. Stem Cell Biol., vol. 49, no. 1, p. e81, Jun. 2019, doi: 10.1002/cpsc.81.

[170] K. Kirino, T. Nakahata, T. Taguchi, and M. K. Saito, 'Efficient derivation of sympathetic neurons from human pluripotent stem cells with a defined condition', *Sci. Rep.*, vol. 8, no. 1, p. 12865, Dec. 2018, doi: 10.1038/s41598-018-31256-1.

[171] Y. Takayama, H. Kushige, Y. Akagi, Y. Suzuki, Y. Kumagai, and Y. S. Kida, 'Selective Induction of Human Autonomic Neurons Enables Precise Control of Cardiomyocyte Beating', *Sci. Rep.*, vol. 10, no. 1, p. 9464, Dec. 2020, doi: 10.1038/s41598-020-66303-3.

[172] A. Takeuchi, M. Mori, K. Kitagawa, K. Shimba, Y. Takayama, H. Moriguchi, K. Miwa, K. Kotani, Jong-Kook Lee, M. Noshiro, and Y. Jimbo, 'Autonomic nervous system driven cardiomyocytes in vitro', in *2011 Annual International Conference of the IEEE Engineering in Medicine and Biology Society*, IEEE, Aug. 2011, pp. 1945–1948. doi: 10.1109/IEMBS.2011.6090549.

[173] K. Sakai, K. Shimba, K. Ishizuka, Z. Yang, K. Oiwa, A. Takeuchi, K. Kotani, and Y. Jimbo, 'Functional innervation of human induced pluripotent stem cell-derived cardiomyocytes by co-culture with sympathetic neurons developed using a microtunnel technique', *Biochem. Biophys. Res. Commun.*, vol. 494, no. 1–2, pp. 138–143, Dec. 2017, doi: 10.1016/j.bbrc.2017.10.065.

[174] M. Häkli, S. Jäntti, T. Joki, L. Sukki, K. Tornberg, K. Aalto-Setälä, P. Kallio, M. Pekkanen-Mattila, and S. Narkilahti, 'Human Neurons Form Axon-Mediated Functional Connections with Human Cardiomyocytes in Compartmentalized Microfluidic Chip', *Int. J. Mol. Sci.*, vol. 23, no. 6, p. 3148, Mar. 2022, doi: 10.3390/ijms23063148.

[175] A. Winbo, S. Ramanan, E. Eugster, S. Jovinge, J. R. Skinner, and J. M. Montgomery, 'Functional coculture of sympathetic neurons and cardiomyocytes derived from human-induced pluripotent stem cells', *Am. J. Physiol. Circ. Physiol.*, vol. 319, no. 5, pp. H927–H937, Nov. 2020, doi: 10.1152/ajpheart.00546.2020.

[176] W. J. Kowalski, I. H. Garcia-Pak, W. Li, H. Uosaki, E. Tampakakis, J. Zou, Y. Lin, K. Patterson, C. Kwon, and Y.-S. Mukouyama, 'Sympathetic Neurons Regulate Cardiomyocyte Maturation in Culture', *Front. Cell Dev. Biol.*, vol. 10, Mar. 2022, doi: 10.3389/fcell.2022.850645.

[177] J. M. Stein, U. Arslan, M. Franken, J. C. de Greef, S. E. Harding, N. Mohammadi, V. V. Orlova, M. Bellin, C. L. Mummery, and B. J. van Meer, 'Software Tool for Automatic Quantification of Sarcomere Length and Organization in Fixed and Live 2D and 3D Muscle Cell Cultures In Vitro', *Curr. Protoc.*, vol. 2, no. 7, Jul. 2022, doi: 10.1002/cpz1.462.

[178] P. Cahan and G. Q. Daley, 'Origins and implications of pluripotent stem cell variability and heterogeneity', *Nat. Rev. Mol. Cell Biol.*, vol. 14, no. 6, pp. 357–368, Jun. 2013, doi: 10.1038/nrm3584.

[179] X. Lian, X. Bao, A. Al-Ahmad, J. Liu, Y. Wu, W. Dong, K. K. Dunn, E. V. Shusta, and S. P. Palecek, 'Efficient Differentiation of Human Pluripotent Stem Cells to Endothelial Progenitors via Small-Molecule Activation of WNT Signaling', *Stem Cell Reports*, vol. 3, no. 5, pp. 804–816, Nov. 2014, doi: 10.1016/j.stemcr.2014.09.005.

[180] P. Hofbauer, S. M. Jahnel, N. Papai, M. Giesshammer, A. Deyett, C. Schmidt, M. Penc, K. Tavernini, N. Grdseloff, C. Meledeth, L. C. Ginistrelli, C. Ctortecka, Š. Šalic, M. Novatchkova, and S. Mendjan, 'Cardioids reveal self-organizing principles of human cardiogenesis', *Cell*, vol. 184, no. 12, pp. 3299-3317.e22, Jun. 2021, doi: 10.1016/j.cell.2021.04.034.

[181] M. D. Sutcliffe, P. M. Tan, A. Fernandez-Perez, Y.-J. Nam, N. V. Munshi, and J. J. Saucerman, 'High content analysis identifies unique morphological features of reprogrammed cardiomyocytes', *Sci. Rep.*, vol. 8, no. 1, p. 1258, Dec. 2018, doi: 10.1038/s41598-018-19539-z.

Supplementary Data

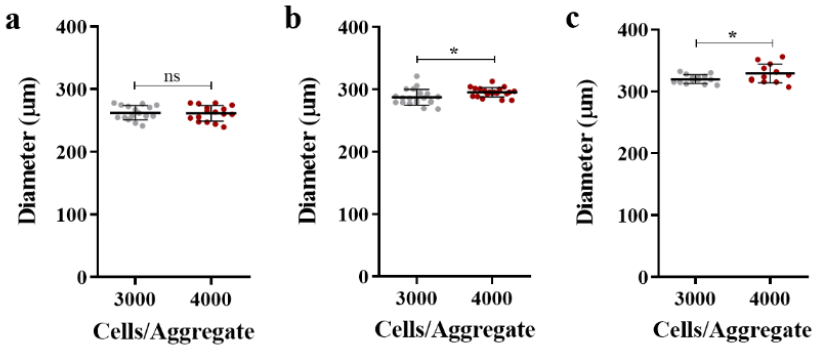

Supplementary Figure 1: Characterization of the pre-differentiation period of CM differentiation as 3D aggregates from R2C6 hiPSCs. R2C6 aggregate size for a cell seeding density of 3000 and 4000 cells/aggregate at D0 by Feret diameter measurement. Mean ± SD; **(a)** n=1, 262.2 ± 2.9 µm and 261.4 ± 3.1 µm for the cell seeding density of 3000 and 4000 cells/aggregate, respectively, measuring N=16 aggregates for each condition; **(b)** n=2, 287.3 ± 2.8 µm and 295.3 ± 1.7 µm for the cell seeding density of 3000 and 4000 cells/aggregate, respectively, measuring N=20 aggregates for each condition; **(c)** n=3, 320.0 ± 1.9 µm and 329.2 ± 4.1 µm for the cell seeding density of 3000 and 4000 cells/aggregate, respectively, measuring N=14 aggregates for the 3000 cells/aggregate condition and N=13 for the 4000 cells/aggregate condition. Statistical analysis was performed using T-tests, with (*) $p < 0.05$, (ns) not significant.

Supplementary Table 1: CM differentiation efficiency (%) of RTT and healthy hiPSC-derived CM aggregates. The assessment of CM differentiation efficiency of 1) R2C6 cell line was evaluated for a cell seeding density of 3000 or 4000 cells/aggregate combined with 9 or 11 µM CHIR concentration; 2) R255X M cell line was evaluated for a cell seeding density of 4000 or 5000 cells/aggregate combined with 7, 9 or 11 µM CHIR concentration; 3) DF6 cell line was evaluated for a cell seeding density of 3800 cells/aggregate combined with 11 µM CHIR concentration; 4) and R255X WT cell line was evaluated for a cell seeding density of 4000 or 5000 cells/aggregate combined with 7, 9 or 11 µM CHIR concentration. The results were obtained by flow cytometry analysis for cTnT at D11-15.

CM differentiation efficiency (%)					
		R2C6		**R255X M**	
		3000 cells/aggregate	4000 cells/aggregate	4000 cells/aggregate	5000 cells/aggregate
RTT hiPSC-derived CM aggregates	7 µM CHIR	-----	-----	77.1	75.6
	9 µM CHIR	39.5 (n=1) 78.5 (n=2)	65.0 (n=1) 70.6 (n=2)	66.1	67.9
	11 µM CHIR	16.0 (n=1) 27.7 (n=2)	1.9 (n=1) 43.4 (n=2)	76.1	70.4
		DF6		**R255X WT**	
		3800 cells/aggregate		4000 cells/aggregate	5000 cells/aggregate
Healthy hiPSC-derived CM aggregates	7 µM CHIR	-----		66.7	73.3
	9 µM CHIR	-----		67.6	70.4
	11 µM CHIR	75.0 (n=1) 84.8 (n=2) 82.1 (n=3)	85.3 (n=4) 78.0 (n=5) 67.4 (n=6)	67.8	70.1

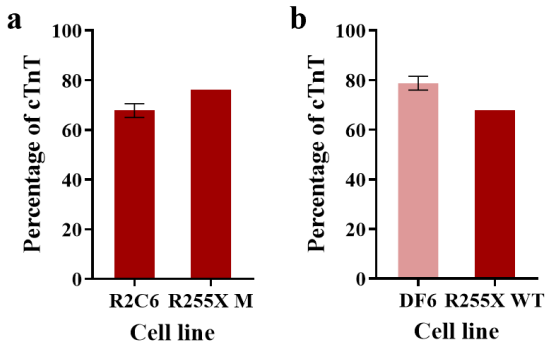

Supplementary Figure 2: Assessment of the CM differentiation efficiency of MT and WT aggregates. **(a)** Comparison between CM differentiation efficiency of R2C6 and R255X M aggregates by flow cytometry analysis for cTnT at D11-15. Mean ± SEM; n=2 experiments for the R2C6 cell line and n=1 experiment for the R255X M cell line. **(b)** Comparison between CM differentiation efficiency of DF6 and R255X WT aggregates by flow cytometry analysis for cTnT at D11-15. Mean ± SEM; n=6 experiments for the DF6 cell line and n=1 experiment for the R255X WT cell line. MT aggregates correspond to the R2C6 cell line with the combination of a 4000 cells/aggregate density and a 9 µM CHIR concentration and the R255X M cell line with the combination of a 4000 cells/aggregate density and a 11 µM CHIR concentration; WT aggregates correspond to the DF6 cell line with the combination of a 3800 cells/aggregate density and a 11 µM CHIR concentration and the R255X WT cell line with the combination of a 4000 cells/aggregate density and a 11 µM CHIR concentration.

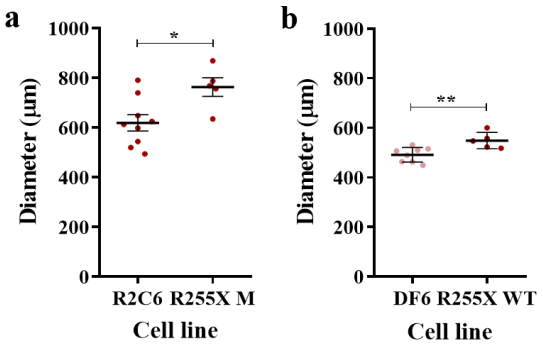

Supplementary Figure 3: Characterization of the MT and WT aggregate size at the end of differentiation. (a) Comparison between R2C6 and R255X M aggregate size at D11-13. Mean ± SEM; measuring N=9 R2C6 aggregates and N=5 R255X M aggregates. **(b)** Comparison between DF6 and R255X WT aggregate size at D11-13. Mean ± SD; measuring N=8 DF6 aggregates and N=5 R255X WT aggregates. MT aggregates correspond to the R2C6 cell line with the combination of a 4000 cells/aggregate density and a 9 µM CHIR concentration and the R255X M cell line with the combination of a 4000 cells/aggregate density and a 11 µM CHIR concentration; WT aggregates correspond to the DF6 cell line with the combination of a 3800 cells/aggregate density and a 11 µM CHIR concentration and the R255X WT cell line with the combination of a 4000 cells/aggregate density and a 11 µM CHIR concentration. Statistical analysis was performed using T-tests, with (*) $p < 0.05$, (**) $p < 0.01$.

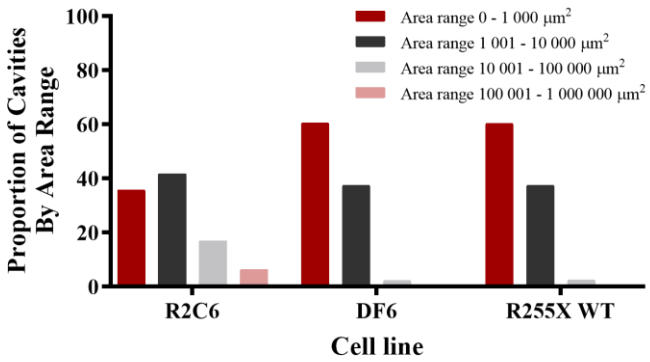

Supplementary Figure 4: Cavity size distribution of R2C6, DF6 and R255X WT aggregates. Four area ranges were considered: from 0 to 1 000 µm²; from 1 001 to 10 000 µm²; from 10 001 to 100 000 µm²; from 100 001 to 1 000 000 µm².